EPRI

Evaluation of Zinc Addition to Primary Coolant PWRs: Fuel Cladding Corrosion

WARNING:
Please read the Export Control Agreement on the back cover.

Technical Report

Evaluation of Zinc Addition to the Primary Coolant of PWRs

TR-106358-V2
4023-01

Final Report, August 1996

Prepared by
WESTINGHOUSE ELECTRIC CORPORATION
Nuclear Services Division
Madison, Pennsylvania

Authors

R. E. Gold	-	Nuclear Services Division
J. W. Kormuth	-	Nuclear Services Division
C. A. Bergmann	-	Systems & Major Projects Division
J. D. Perock	-	Systems & Major Projects Division
G. J. Corpora	-	Systems & Major Projects Division
R. S. Miller	-	Nuclear Manufacturing Divisions
G. Springer	-	Electro-Mechanical Division
S. L. Jenkins	-	Electro-Mechanical Division
J. Roesmer	-	Consultant

Prepared for
Electric Power Research Institute
3412 Hillview Avenue
Palo Alto, California 94304

EPRI Project Manager
R. Pathania
Nuclear Power Group

DISCLAIMER OF WARRANTIES AND LIMITATION OF LIABILITIES

ORGANIZATION(S) THAT PREPARED THIS REPORT

WESTINGHOUSE ELECTRIC CORPORATION

ORDERING INFORMATION

Requests for copies of this report should be directed to the EPRI Distribution Center, 207 Coggins Drive, P.O. Box 23205, Pleasant Hill, CA 94523, (510) 934-4212.

REPORT SUMMARY

Volume 1 of this report summarized the results of a zinc demonstration project at Farley Unit 2 that showed that addition of 35-45 ppb zinc to the primary coolant resulted in lower radiation dose rates, an apparent decrease in primary water stress corrosion cracking (PWSCC) of Alloy 600 steam generator tubing, and no significant effect on fuel cladding corrosion. Volume 2 presents an analysis of the fuel cladding corrosion data that confirms the conclusion that zinc addition did not have a significant effect on cladding corrosion.

Background

Previous laboratory studies had indicated that addition of zinc to PWR primary coolant could reduce the general corrosion rates of the primary system materials, decrease radiation fields, and partially inhibit PWSCC of Alloy 600 components. EPRI and a group of utilities from the Westinghouse Owners Group (WOG) sponsored a demonstration of zinc addition at Farley Unit 2 operated by Southern Nuclear Operating Company.

Objectives

- To establish whether the benefits of zinc addition in mitigating radiation fields and PWSCC of Alloy 600 that had been observed in the laboratory could be realized in an operating plant.
- To confirm that zinc addition does not have an adverse effect on fuel cladding corrosion, reactor coolant pump performance, or valve maintenance.

Volume 1 addresses both objectives, and Volume 2 provides a detailed assessment of the effect of zinc on fuel cladding corrosion.

Approach

The investigators used EPRI's PWR Fuel Cladding Corrosion (PFCC) model to analyze the cladding oxide thickness data from Farley-2 Cycle 9 (without zinc) and Cycle 10 (with zinc). In addition, they analyzed data provided by Southern Nuclear from Farley-1 cycle 13 (without zinc). The PFCC model is a parametric model that correlates cladding corrosion to factors such as heat flux, power history, material variability, lithium concentration, coolant temperature, and cladding temperature. The researchers used the PFCC model to assess the roles of thermal hydraulic duty, material variability, and zinc addition on fuel cladding corrosion.

Results

The cladding oxide measurements showed that both Farley-2 Cycle 10 (with zinc) and Farley-1 Cycle 13 (without zinc) had higher corrosion than Farley-2 Cycle 9(without zinc). The investigators concluded that the higher than expected thickness values of some rods from Farley-2 Cycle 10 and Farley-1 Cycle 13 resulted from higher thermal duty. Subcooled boiling was predicted to occur on some of the high power rods. The rods with the highest oxide measurements were often found at locations where two adjacent assemblies were placed next to each other resulting in simultaneous subcooled boiling at adjacent rods. Based on the EPRI PFCC model there was no statistically significant difference between Farley-2 Cycle 10 and Farley-1 Cycle 13. The researchers therefore concluded that zinc addition had no significant effect on cladding corrosion in Farley-2.

EPRI Perspective

EPRI report TR-106358, Volumes 1 and 2 support the conclusion that zinc addition does not have an adverse effect on cladding corrosion. A related EPRI report on Evaluation of Zinc Addition on Fuel Cladding at the Halden Test Reactor (TR-106357) also concluded that zinc addition did not increase cladding corrosion. Radiation measurements at Farley reported in TR-106358, Volume 1 showed a beneficial effect of zinc. PWSCC data are less conclusive but indicated a possible beneficial effect of zinc. In view of these results, EPRI recommends a continuation of the zinc demonstration program at Farley. Southern Nuclear is considering resumption of zinc addition at Farley-2 during Cycle 12.

TR-106358-V2

Interest Categories

Fuel assembly reliability and performance
Chemistry

Key Words

Fuel cladding corrosion
Zircaloy corrosion
Primary coolant chemistry
Fuel reliability

ABSTRACT

The Farley Unit 2 post-Zn fuel rod corrosion data obtained at the end of cycle (EOC) 10, after a half cycle of zinc injection, were analyzed and compared with data taken at EOC9 prior to the zinc injection. Additional data taken at Farley-1 EOC13 on fuel assemblies of the same design and comparable thermal/hydraulic duty were also compared. The corrosion data were analyzed for axial oxide thickness profile, rod-to-rod, and assembly-to-assembly corrosion variability to determine the roles of measurement accuracy and material variability. The effect of thermal/hydraulic duty, using the radial peaking factor as an indicator, was also compared. The rod peak oxide thickness of the three sets of data were analyzed using the EPRI PFCC cladding corrosion model and compared to each other and with other industry data base. Because the scope of the examination campaigns varied greatly, a statistical analysis was employed to determine the mean oxide values and the standard deviations. Finally, the differences between the Farley Unit 2 post-Zn Cycle 10 data and that of the pre-Zn Cycle 9 and the Farley Unit 1 non-Zn Cycle 13 data are discussed. The roles of material variability, thermal/hydraulic duty, and zinc injection on the differences in the corrosion data are discussed.

EXECUTIVE SUMMARY

One difficulty encountered in assessing the effect of zinc injection in Cycle 10 on fuel rod corrosion at Farley-2 resulted mainly from a simultaneous increase in the local thermal duty of some fuel from Cycle 9 to Cycle 10. Analyses of the available data base suggest that the major contributor to the increased corrosion of the Farley-2 Cycle 10 (F2C10) rods was the increased T/H duty, rather than the zinc injection. However, the boiling duty of the F2C10 rods is relatively mild when compared to some high temperature plants, thus, cautions should be taken in applying the Farley-2 experience to high duty plants.

Overall, the F2C10 post-Zn and the Farley-1 Cycle 13 (F1C13) without Zn injection rods had higher corrosion than the F2C9 pre-Zn rods. The F2C10 post-Zn cladding corrosion was only marginally higher than the F1C13 non-Zn rods, mainly because five F2C10 rods had peak oxide thickness values (62-73 μm) exceeding the maximum value of 62 μm found on the F1C13 rods. However, based on EPRI PFCC model no statistical differences between the two data sets can be discerned. Nevertheless, the upper ranges of the oxide thickness of the F2C10 and F1C13 rods, being 20-30, 60-73, and 80-100 μm for the once, twice, and thrice burnt rods, respectively, have also been reported sporadically by plants without zinc injection. Thus, any effect of the zinc injection on cladding corrosion is very subtle, as based on the available data base.

Likely explanations for those few higher corrosion rods in the post-Zn data are: (1) random cladding material variability, and (2) random crud deposition due to local rod power variations. From evaluation of cladding manufacturing records and assessment of rod-to-rod corrosion variability, it was concluded that material variability was not a significant issue for the majority of the cladding in the F2C9, F2C10 and F1C13 rods. Thus, the random occurrence of those few high corrosion rods in the twice burnt F2C10 assemblies might be related to the black deposits, although an effect of material variability cannot be completely ruled out.

It was concluded that higher T/H duty on some of the F2C10 and F1C13 rods contributed to the higher than expected oxide thickness values. Subcooled boiling was estimated to occur during the first cycle of operation on some of the high power rods. The rods with the highest peak oxide measurements were often found at locations where two high power assemblies were placed next to each other, resulting in simultaneous subcooled boiling of adjacent rods. It is not clear how this would result in an increased corrosion rate since the wall temperature is not largely impacted. One postulated explanation is that significant subcooled boiling could lead to local radiolytic

production of oxidizing species, which can increase the corrosion rate of Zircaloy. Another possibility is formation of crud deposits during operation to cause a thermal impedance effect or hideout of lithium inside the crud. Neither of the explanations can be substantiated at the moment.

In summary, while the Farley-2 experience indicated no significant effect of zinc injection on cladding corrosion, the same cannot be said with certainty if the fuel duty is increased. A fuel T/H duty analysis and coolant chemistry review should be performed, and if the conditions exceed the Farley-2 experience, a fuel surveillance program should be implemented.

ACKNOWLEDGMENTS

The PFCC corrosion model calculations were performed by staff members at S. Levy, Incorporated, including Paul Rank, Jeff Voskuil, and Patricia Gilmore. Their contributions are greatly appreciated. Thanks are also due to Dr. H. Klepfer for supervising the PFCC analysis and Neils Kjaer Patterson for suggestions on rod thermal/hydraulic issues. Acquisition of the oxide data and preparation of input data required to run the PFCC analysis were provided by Westinghouse Electric and Southern Nuclear, where many individuals made important contributions. From Westinghouse, Bob Gold and Dick Miller have been most helpful. Ken Turnage, Bruce Hunt, Mason Dove, Ron Cocherell are among numerous active contributors from the Southern Nuclear Company. Raj Pathania, and Rosa Yang of EPRI provided project management support. Finally, thanks are due to Southern Nuclear management for their support.

Ken Turnage, Mason Dove, Raj Pathania, and Bob Gold provided valuable comments and suggestions during preparation of this report. Martin Pytel of PI Development assisted diligently in the replotting of figures, reformatting data tables, and preparing this report for publication.

CONTENTS

ILLUSTRATIONS

TABLES

1

INTRODUCTION

To support the in-plant demonstration of zinc injection at Farley-2, EPRI funded fuel inspection and cladding oxide thickness measurement campaigns at the end of cycles (EOC) 9 and 10. The zinc injection was performed for the last 260 days (6/12/94 to 2/27/95) during cycle 10 which had a cycle length of 462 days (12/2/93 to 3/11/95). The EOC 9 inspection and measurement were performed to establish the baseline conditions in fuel rod surface deposits and cladding oxide thickness.

The pre-zinc EOC9 results were as expected: (a) fuel rods were essentially free of crud deposits except some spotty deposits at the hottest span, #6; (b) rod oxide thickness values were within the experience base. The post-zinc EOC10 (April 1995) results were not as-expected in three aspects. First, all fuel assemblies, regardless of burnup, had an apparently thin black coating covering essentially the entire rod length, including the bottom and top nozzles and grids. Second, the axial shapes of the rod oxide thickness from eddy current measurements were atypical for some once and twice burnt rods. Third, the rod maximum oxide thickness values for once, twice, and thrice burnt fuel were on average higher than expected based on the Westinghouse database for low tin Zircaloy-4 cladding. Thirty-three twice burnt fuel assemblies originally scheduled for reload were discharged to the fuel storage pool due to concern with the higher than expected oxide thickness.

The unexpected results from the EOC10 post-zinc inspection led to a re-inspection of the twice and thrice burnt fuel in November 1995 to ascertain that the atypical axial oxide thickness profiles and higher than expected oxide thickness values were not a result of oxide measurement error stemming from interference of the black deposit with the eddy current probe. In addition, Southern Nuclear performed a fuel inspection and oxide measurement campaign at Farley-1 EOC13 to obtain data on comparable fuel for analysis.

The black deposits found at Farley-2 EOC10 were scraped for analysis. The loading averaged <10 mg/dm^2 or <1.0 μm over the highest temperature spans #4-6 from the bottom. The main constituents in the deposits were Fe and Ni; Zn only constituted ~2-4% of the total metallic deposits. During the November 1995 re-inspection, the black surface deposits were all substantially dissolved after residing in the acidic (pH~4.5) storage pool for approximately 6 months, leaving a typical whitish oxide surface.

Surprisingly, the Farley-1 EOC13 inspection also found a black deposit on all fuel assemblies, although the F1C13 deposit appeared to be not as dark and smooth as those found at F2C10. At the highest temperature spans #4-6 of highest temperature F1C13 once burnt rods, the deposits appeared thicker and textured. Analysis of scraped samples confirmed that the F1C13 deposits at spans #4-6 were indeed up to 5 to 10 times thicker than those found on once burnt rods at F2C10. The common occurrence of the black deposit at both units indicate that zinc was unlikely to be the cause of the black deposits at Farley-2. Also, the very light deposits on the F2C10 fuel surface would suggest that the black deposit could not have a noticeable thermal impedance effect on cladding corrosion. A significant chemical effect of zinc on Zircaloy corrosion was also not likely based on results from in-core loop tests performed at the Halden reactor[(1)]. Furthermore, it was not certain whether the deposit formed during plant operation or during shutdown when the RCS chemistry changed from a reducing to an oxidizing condition. Detailed information on the surface concentration, chemical composition, and radiochemical composition of the black deposit is documented in Volume 1, Section 6, of this report.[(2)]

The oxide data taken at F2C9, F2C10, F1C13, and the remeasurements taken on F2C10 rods in November 1995 were evaluated and analyzed to assess the role of zinc injection on the cladding oxide thickness. Since several fuel and operational factors can contribute to Zircaloy cladding corrosion, a qualified corrosion model with a built-in thermal-hydraulic (T/H) code for fuel rod wall temperature calculation is needed to normalize the T/H and other operational duty differences between different plants and cycles. For the present analysis, the EPRI PWR Fuel Cladding Corrosion (PFCC) model[(3,4)] was used. Before the corrosion data were analyzed using the PFCC model, the data were sorted and grouped in order to extract the portion of the data that will provide a meaningful comparison. Another important objective in sorting the data was to evaluate data variability among rods with essentially the same operational history. A larger than expected variability would lead to questions on the accuracy of the oxide measurement or a variability in the cladding material chemistry or processing.

This report documents the analyses performed on the oxide data from Farley-1 and -2. Various factors contributing to the anomalous corrosion observations of the post-zinc (F2C10) fuel rods were evaluated and the role of zinc assessed. This task was performed with close collaboration among EPRI, Southern Nuclear, and Westinghouse Electric Corporation.

2

OXIDE DATA REVIEW

2.1 DESCRIPTION OF OXIDE DATA AND FUEL TYPE

The data base for this review is shown in Table 2-1. Each of the F2C9, F2C10, and F1C13 oxide measurement campaigns included once, twice, and thrice burnt fuel rods. Only peripheral rods in each fuel assembly were measured. Normally, measurements were performed on 4 to 8 adjacent rods on one face of a fuel assembly. In a few cases where large differences in rod power existed within the assembly due to its proximity to the core periphery, rods on two peripheral faces were measured. Selection of fuel assemblies for inspection were based on assembly design, rod power history, burnup, core location, and cladding material. As can be seen in Table 2-1, the F2C10 campaign was largely expanded to include a total of 47 assemblies including 29 of the 57 twice burnt 2L assemblies in the core. In the November 1995 re-measurement of F2C10 fuel, 13 rods in three 2L assemblies were re-measured. Table 2-1 also shows that, with exception of some twice and thrice burnt F2C9 rods and some thrice burnt F2C10 rods, the fuel cladding material was the Westinghouse improved low Sn (1.3-1.4 wt%) Zircaloy-4 type.

Table 2-1 Farley-1 and -2 Cladding Oxide Thickness Data Reviewed

	Farley-2 Cycle 9		Farley-2 Cycle 10		Farley-1 Cycle 13	
# of Cycle	#FAs	#rods	#FAs	#rods	#FAs	#rods
1	4/0	24/0	11/0	65/0	5/0	30/0
2	3/2	18/12	29/0	134/0	5/0	30/0
3	0/3	0/18	6/1	30/6	2/0	12/0

Note: Listed values A/B are defined as: **(** #FAs or rods using improved (low Sn) Zircaloy-4 cladding**)/(**#FAs or rods using standard cladding (1.5-1.6 wt% Sn)**)**

Two types of fuel designs were included in the data base: Vantage-5 and Standard Westinghouse fuel assembly. The Vantage-5 fuel had higher cycle average radial peaking factor than the Standard design and slightly smaller rod diameter, resulting in

higher heat flux during the first cycle of operation for the highest duty measured rods shown in Table 2-2. Some of the Vantage-5 rods in Table 2-2 had a local heat flux of >100 W/cm^2 at a radial peaking factor >1.39 (axial peaking ~1.17). Most of those high peaking rods also had calculated clad wall temperature exceeding the system saturation temperature of 343.5°C, suggesting the existence of subcooled boiling at the hot spans of those rods.

Table 2-2 Fuel Design Characteristics

Plant/Cycle	Fuel Design	Peaking Factor		#Rods Compared
		1st Cycle	2nd Cycle	# Low Sn Rods
Farley-2/C9(Pre Zn)				
1 cycle	Vantage-5	1.22-1.37	-	24
2 cycle	Standard	0.70-1.34	1.14-1.21	18
3 cycle	Standard	-	-	-
Farley-2/C10(Post Zn)				
1 cycle	Vantage-5	0.65-1.45	-	65
2 cycle	Vantage-5	0.60-1.39	0.34-1.14	134*
3 cycle	Standard	0.77-1.31	0.49-0.95	30
Farley-1/C13(Non Zn)				
1 cycle	Vantage-5	1.31-1.47	-	30
2 cycle	Vantage-5	1.30-1.47	1.09-1.20	30
3 cycle	Standard	0.82-1.30	0.87-1.16	12

* 13 rods in 3 FAs were remeasured in November 1996

The eddy current measurement equipment has an accuracy of ±5 μm[(5)]. Continuous eddy current traces were obtained over a span between grids. In the majority of measurements, oxide thickness traces were obtained from the high temperature spans #4 to 6 (the lowest span is span #1). With the Vantage 5 fuel having intermediate flow mixing (IFM) grids at spans 4-6, the spans are divided and referred to as A for the lower and B for the upper part of the span. Several rods were scanned for the entire length from spans 1 to 7. The eddy current traces were reviewed and the maximum oxide thickness values, after eliminating anomalous signals, are assigned to each span. The

F2C10 and F1C13 measurements were taken over the black surface deposit. Typically, oxide measurements made on surfaces exhibiting crud deposition are not recorded in the Westinghouse oxide data base.

2.2 AXIAL OXIDE THICKNESS PROFILE ANOMALIES

An examination of the axial oxide profiles was made to ascertain that the data conform to industry experience base. Out of the large oxide data base shown in Table 2-1, selected rods in 3 once, 5 twice and 3 thrice burnt F2C10 assemblies were measured for the entire rod length. Unusual axial oxide thickness profiles were found on some of the once and twice burnt rods. Such unusual axial profiles were not found on the thrice burnt F2C10 rods, nor the once, twice and thrice burnt rods in F1C13.

It can be seen in Figure 2-1 that the rod peak oxide location for many once burnt post-Zn F2C10 rods was at spans away from the as-expected peak clad temperature locations of spans 6A and 6B. The once burnt non-Zn F1C13 show as-expected axial profiles, Figure 2-2. In addition to the unusual axial profiles, it is also noted that the post-Zn rods had on average 5 μm thicker oxide at the bottom 3 spans when compared to the non-Zn F1C13 data. At the hot spans 4-6, the post-Zn F2C10 once burnt data are not greater than the non-Zn F1C13 data, if the unusual peak values are smoothed out. The twice burnt F2C10 data, Figures 2-3 and 2-4, also show unusual axial profiles, when compared to the F1C13 data, Figure 2-5. The worst case was seen on F2C10 assembly 2L51, Figure 2-3. The thrice burnt data show no unusual oxide profiles for both F2C10 and F1C13 rods, Figures 2-6 and 2-7, respectively. However, the bottom spans of the post-Zn F2C10 3 cycle rods still showed an oxide ~10 μm thicker than that of the F1C13 rods, even the oxide at the hot spans had about the same oxide thickness values.

The mystery of the unusual oxide peaks and thicker oxide values at bottom spans of the post-Zn F2C10 rods was partially resolved in the re-measurement campaign of three F2C10 twice burnt 2L assemblies in November 1995. Figures 2-8, 2-9, and 2-10 show the axial profiles of the original (EOC in 4/95) and re-measured data for assemblies 2L02, 2L28, and 2L51. It can be seen that the unusual peaks disappeared in the re-measurements. Also, the thickness values at the bottom spans all decreased by 5-10 μm or more for 2L02 and 2L51. In other words, the re-measured data conform to the expected axial oxide profiles. As discussed earlier, the black deposits found at EOC10 in April 1995 were substantially dissolved at re-measurement in November 1995. Thus, it can be concluded that the 5-10 μm "disappeared" oxide at bottom spans was due to the presence of the black deposit since the same eddy current equipment and probe was used in both campaigns. The deposit could interfere with the eddy current signal or affect probe alignment. Figures 2-8 through 2-10 also show that the peak oxide thickness values at spans 6A and 6B are within ~10% between the two separate measurements, except the 6A values for 2L51 where large reductions, again probably due to dissolution of the black deposit, were measured in the November campaign.

A still unanswered question is how a <1.0 μm nickel ferrite (with 2-4% Zn) deposit, estimated from crud scraping, can cause an increase of 5-10 μm and, in some cases, more in the eddy current oxide readings. Recent experiences with Zn injection in BWRs have shown that, in the presence of a magnetic zinc ferrite crud deposit, a bias in the eddy current oxide reading by a factor of ~10 can occur.[6,7] However, the BWR crud deposits that caused a ten-fold bias had a thickness in the range of 10-100 times higher than the F2C10 crud and a Zn content of 10-20%. It is not clear whether a very thin deposit with low Zn content like the one found on F2C10 rods will produce a strong enough magnetic field to cause a large bias in the eddy current reading. An attempt was made during the November 1995 re-measurement to quantify the effect of the black deposit on the oxide measurement by using a multi-frequency eddy current probe. Since the black deposit was largely dissolved except in a few isolated locations, the issue could not be fully resolved. However, for those spots that remained, no measurement bias was observed. Thus, the root cause of the axial oxide profile anomalies of the post-Zn F2C10 rods remains unclear beyond its apparent correlation with the black deposit. A magnetic field interference or some unknown mechanical effects, such as, probe alignment, could have contributed to the anomalies. Although less likely, under-estimate of the crud deposit thickness by crud scraping, cannot be completely ruled out.

Due to the axial oxide anomalies, some of the once and twice burnt values in the F2C10 data were biased on the high side. At the peak oxide locations of spans 6A and 6B, measurement bias was less significant, but still present in some data, as evidenced by the data in Figures 2-1 and 2-10 for assemblies 2M19 and 2L51, respectively. This existence of data bias in the F2C10 data should be taken into account when comparison with other data sets are made.

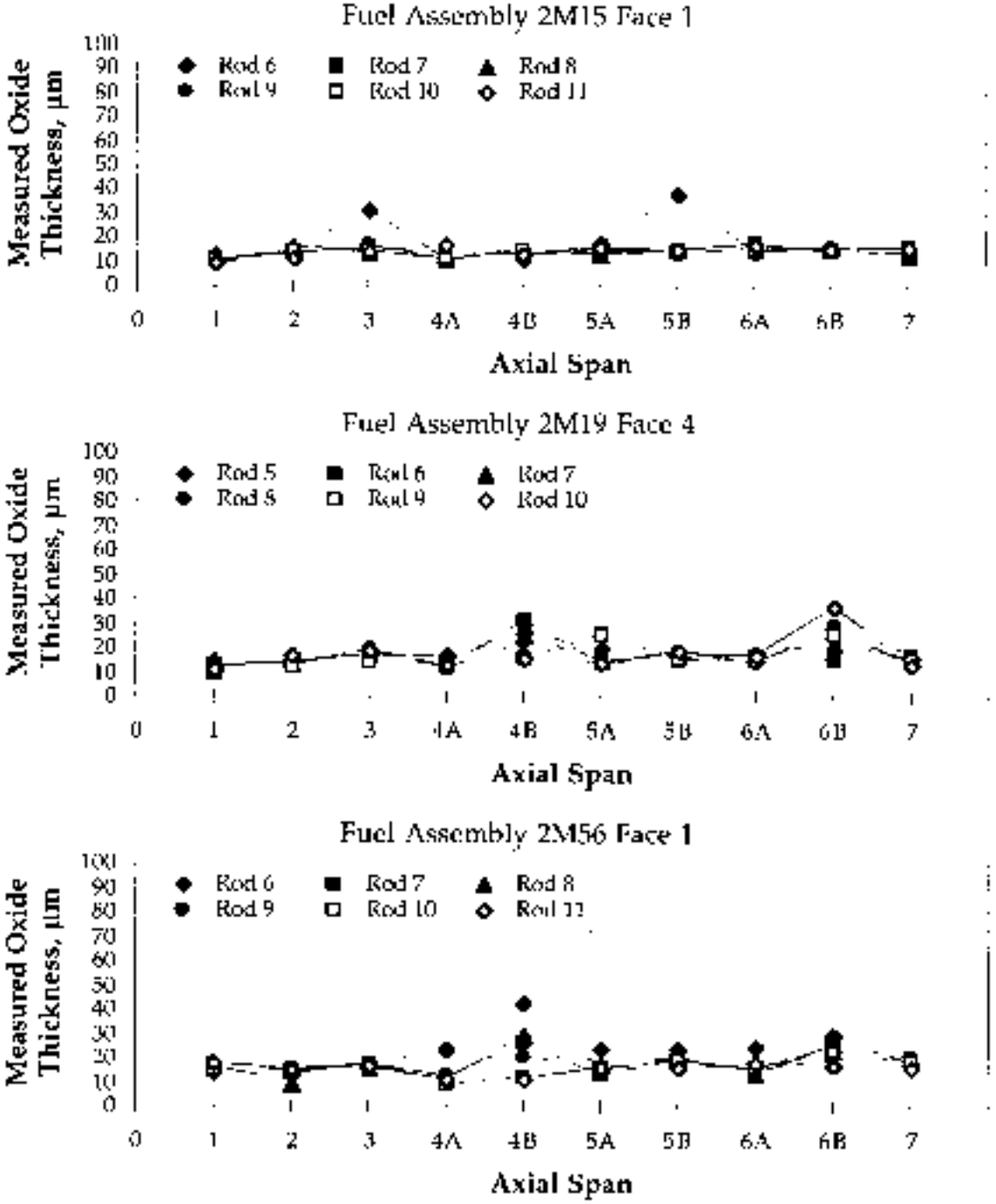

Figure 2-1 Fuel rod oxide thickness profiles measured on Farley-2 1 cycle fuel at EOC10

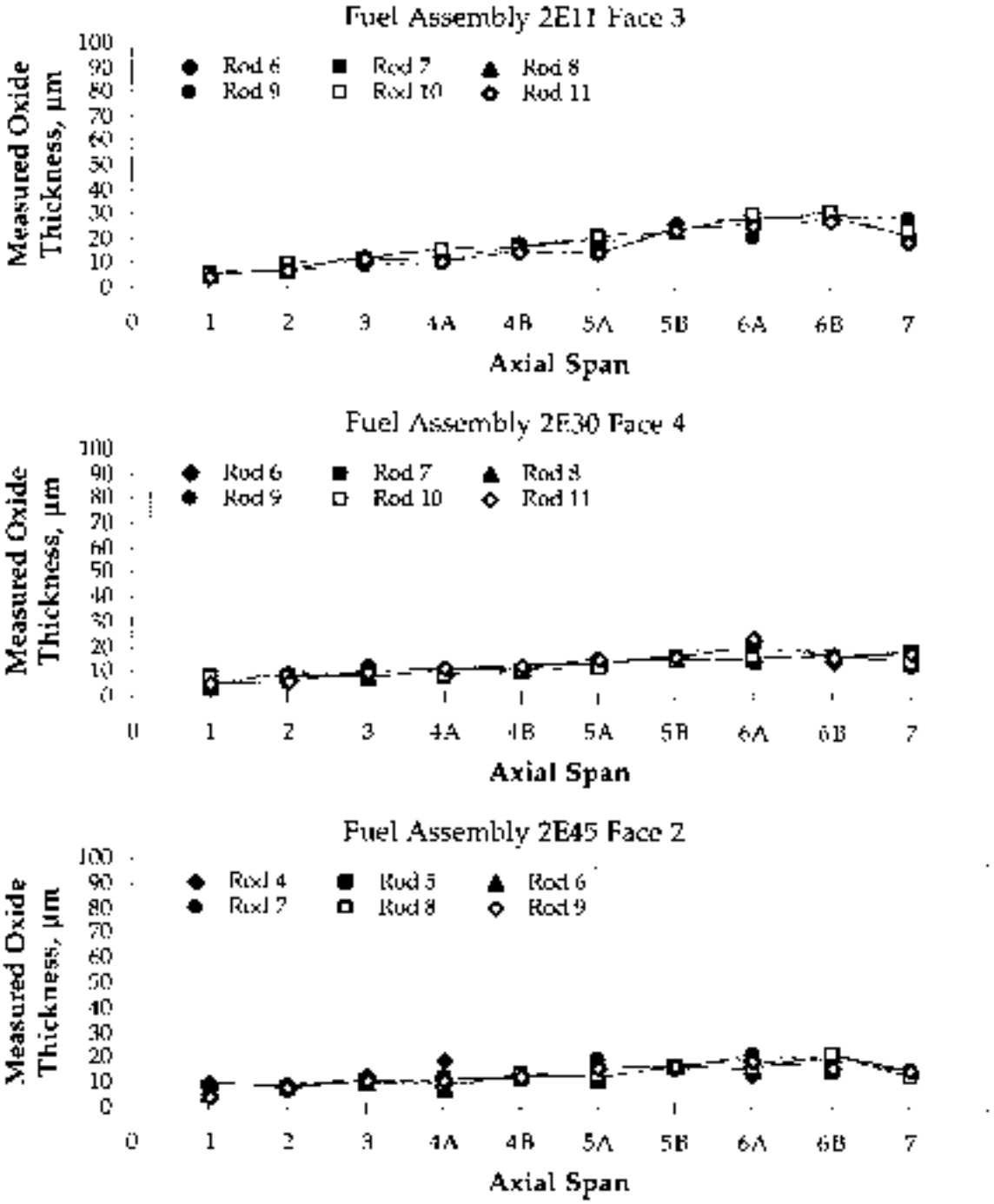

Figure 2-2 Fuel rod oxide thickness profiles measured on Farley-1 1 cycle fuel at EOC13

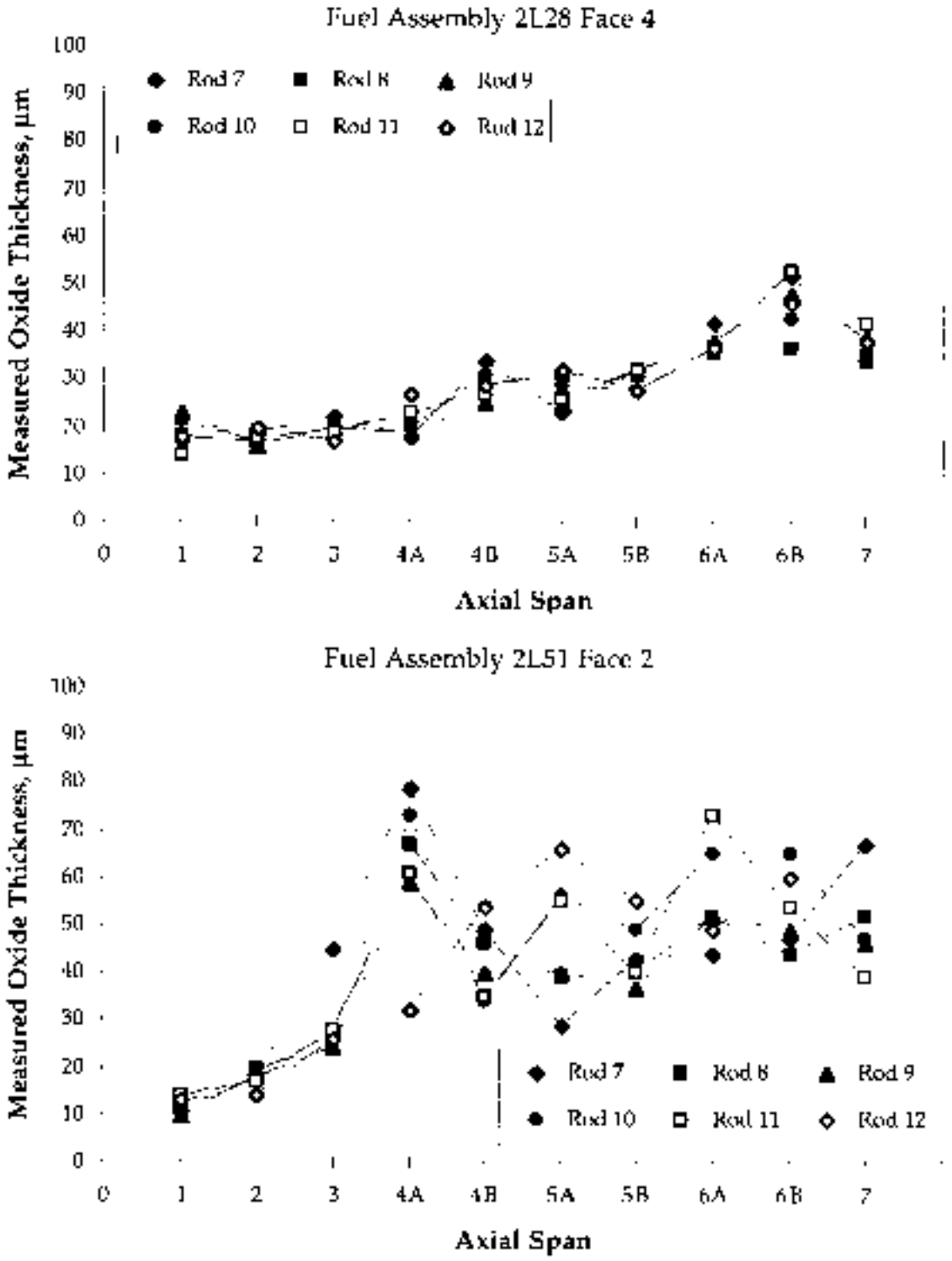

Figure 2-3 Fuel rod oxide thickness profiles measured on Farley-2 2 cycle fuel at EOC10

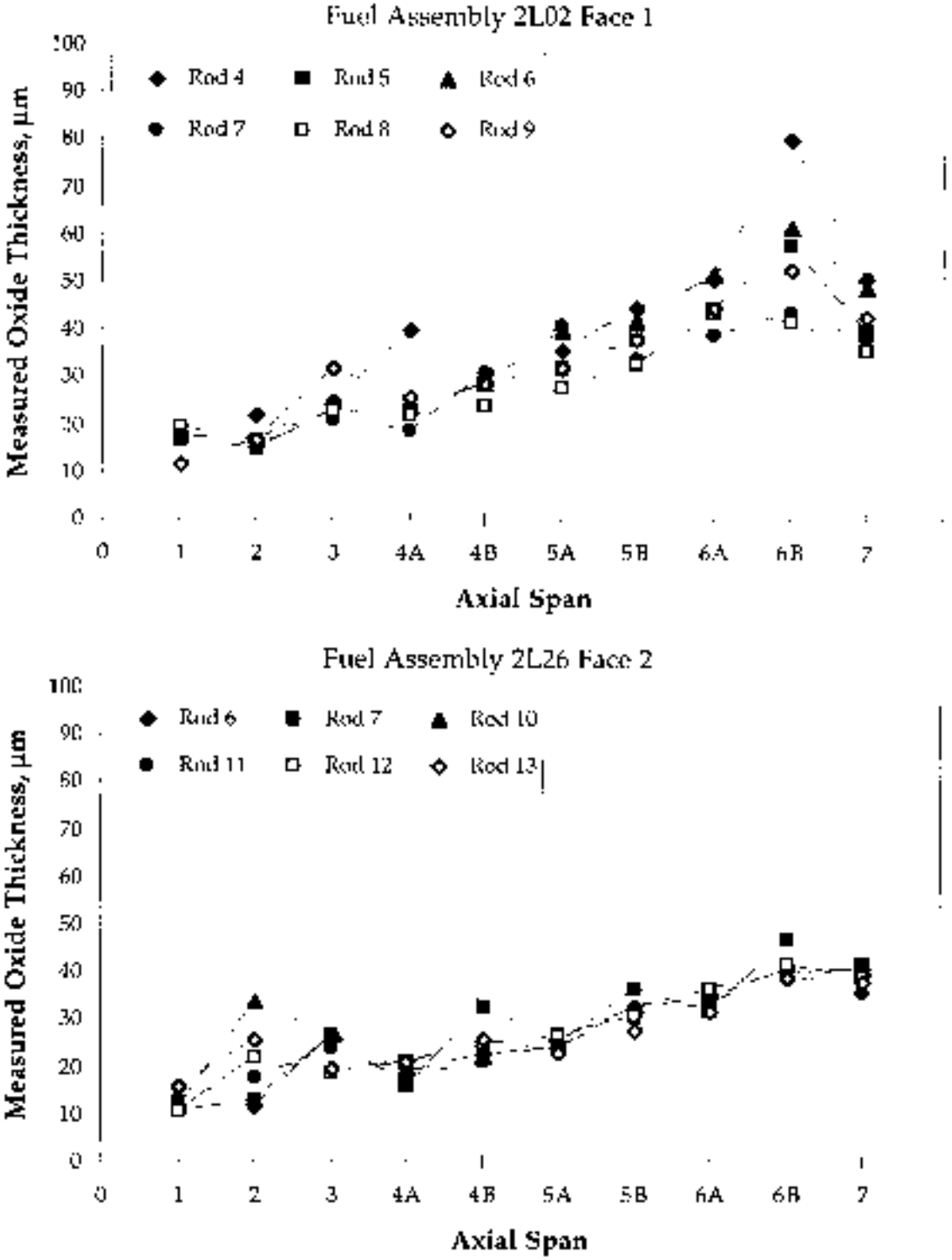

Figure 2-4 Fuel rod oxide thickness profiles measured on Farley-2 2 cycle fuel at EOC10

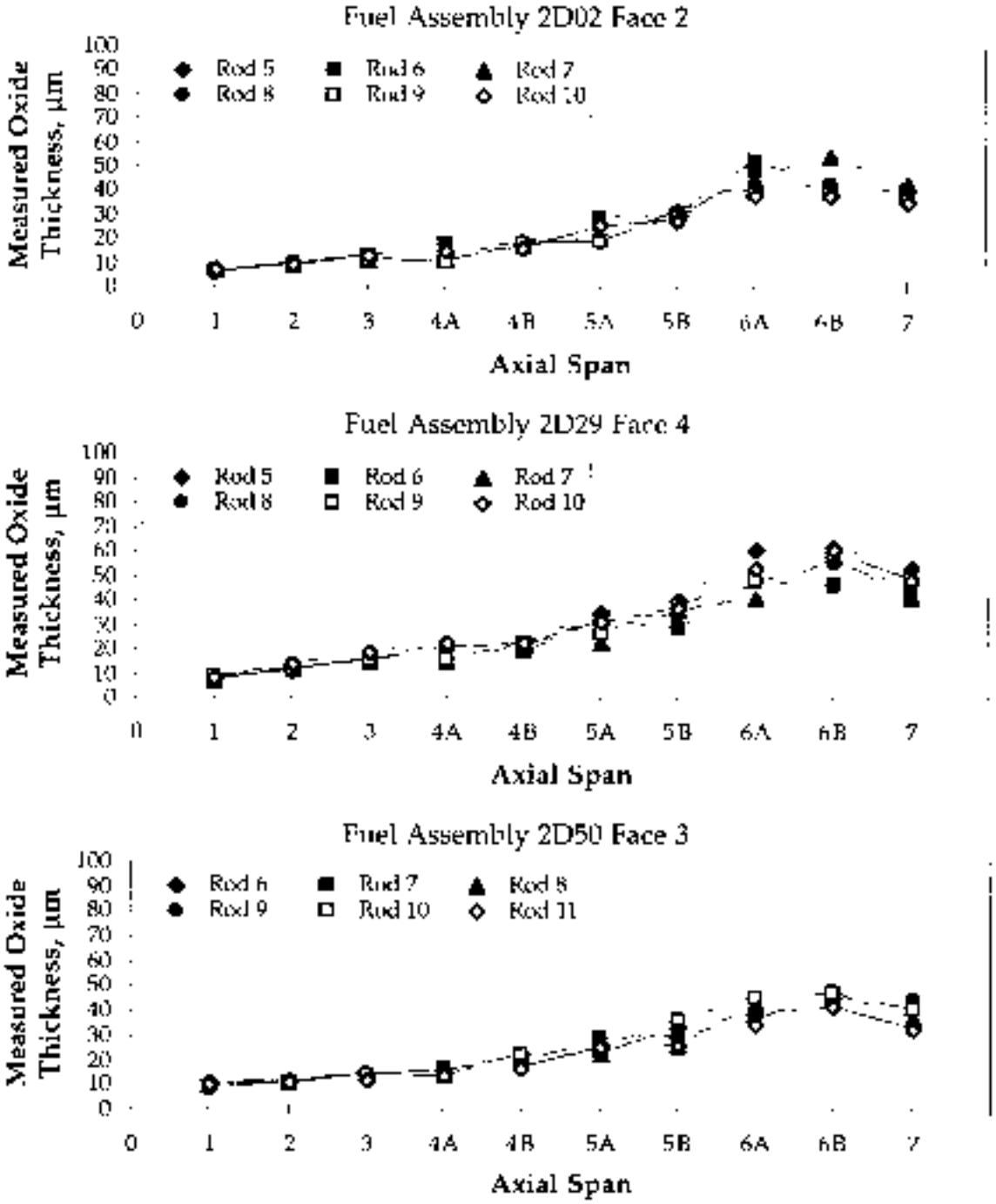

Figure 2-5 Fuel rod oxide thickness profiles measured on Farley-1 2 cycle fuel at EOC13

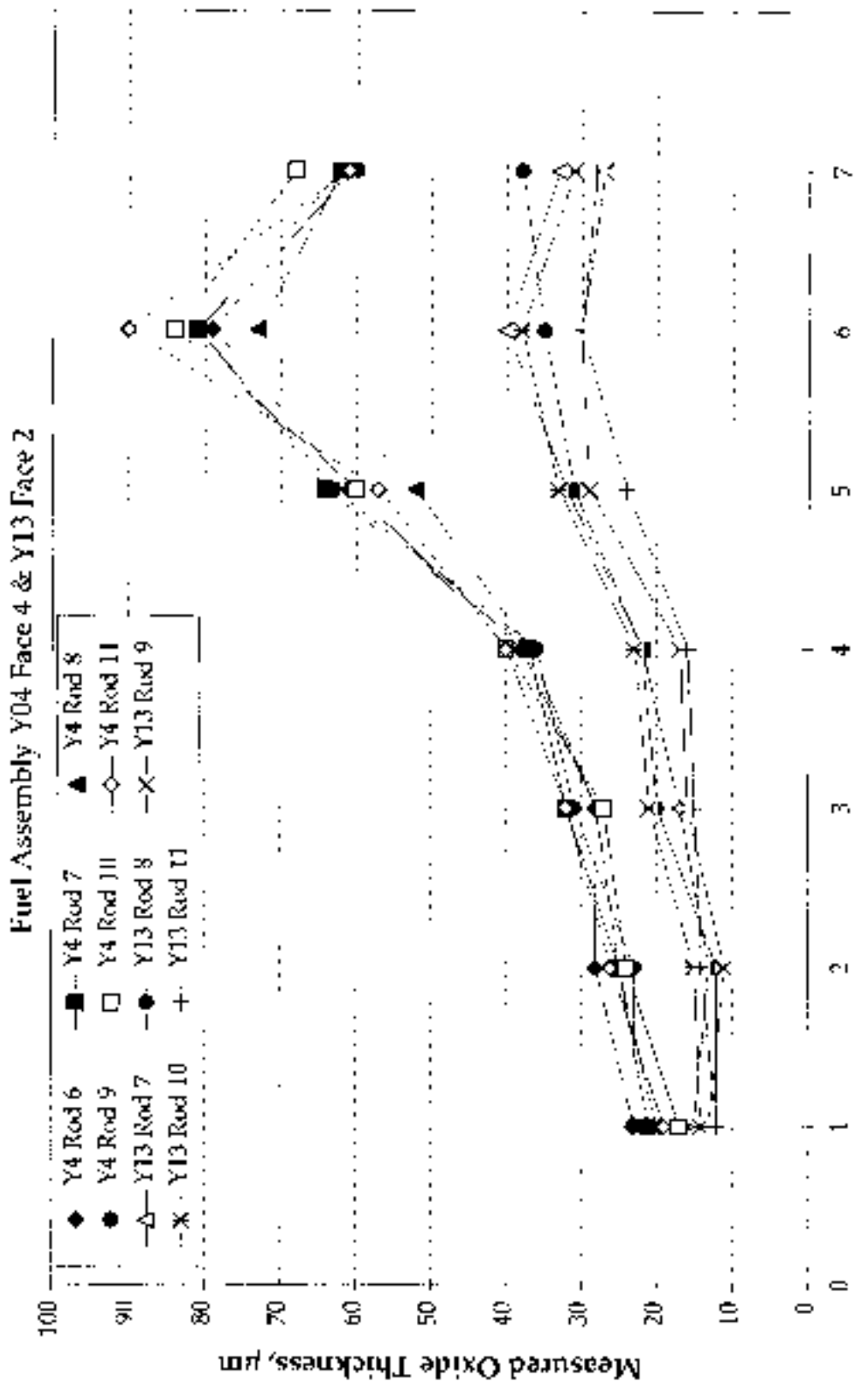

Figure 2-6 Fuel rod oxide thickness profiles measured on Farley-2 3 cycle fuel at EOC10

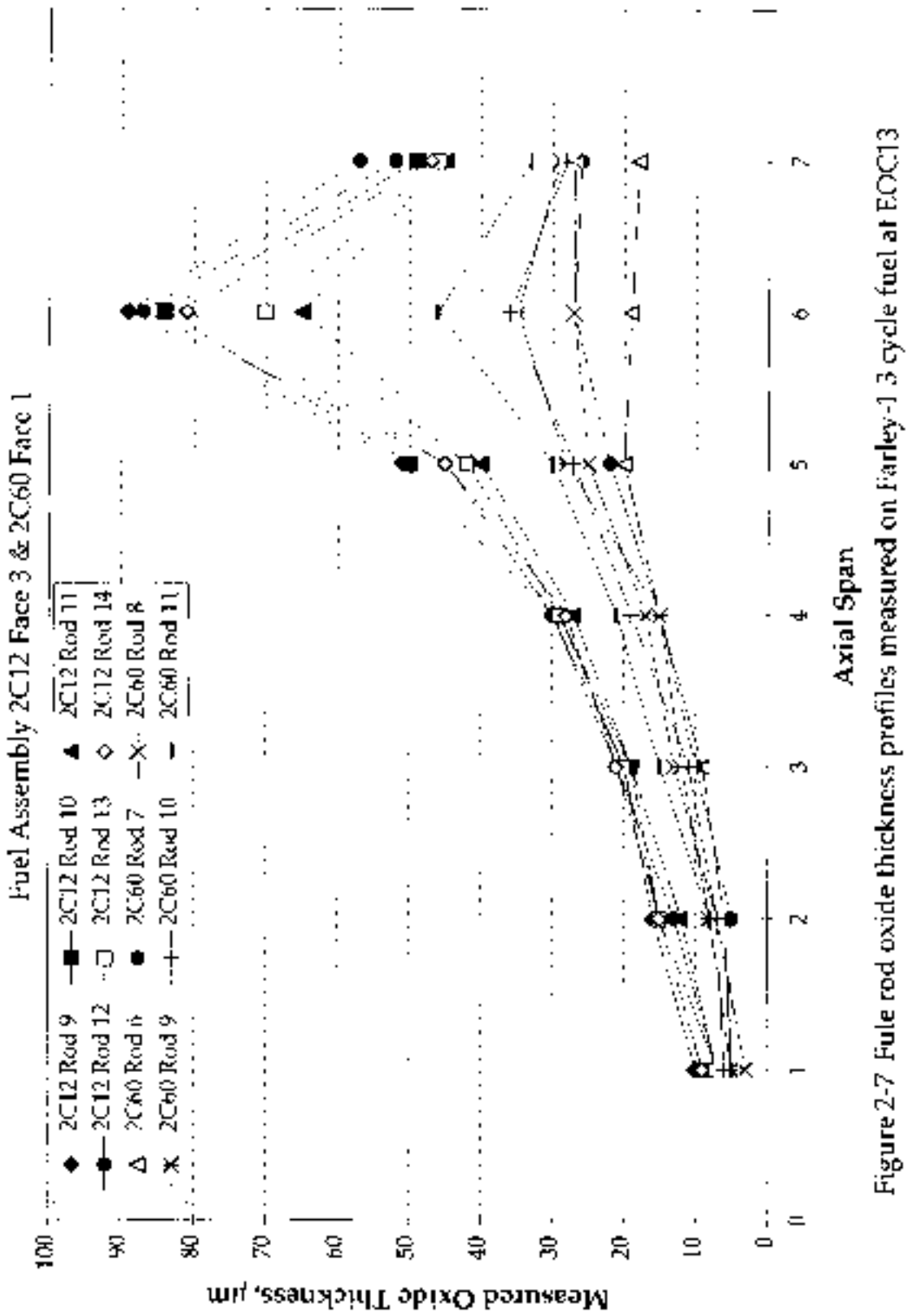

Figure 2-7 Fule rod oxide thickness profiles measured on Farley-1 3 cycle fuel at EOC13

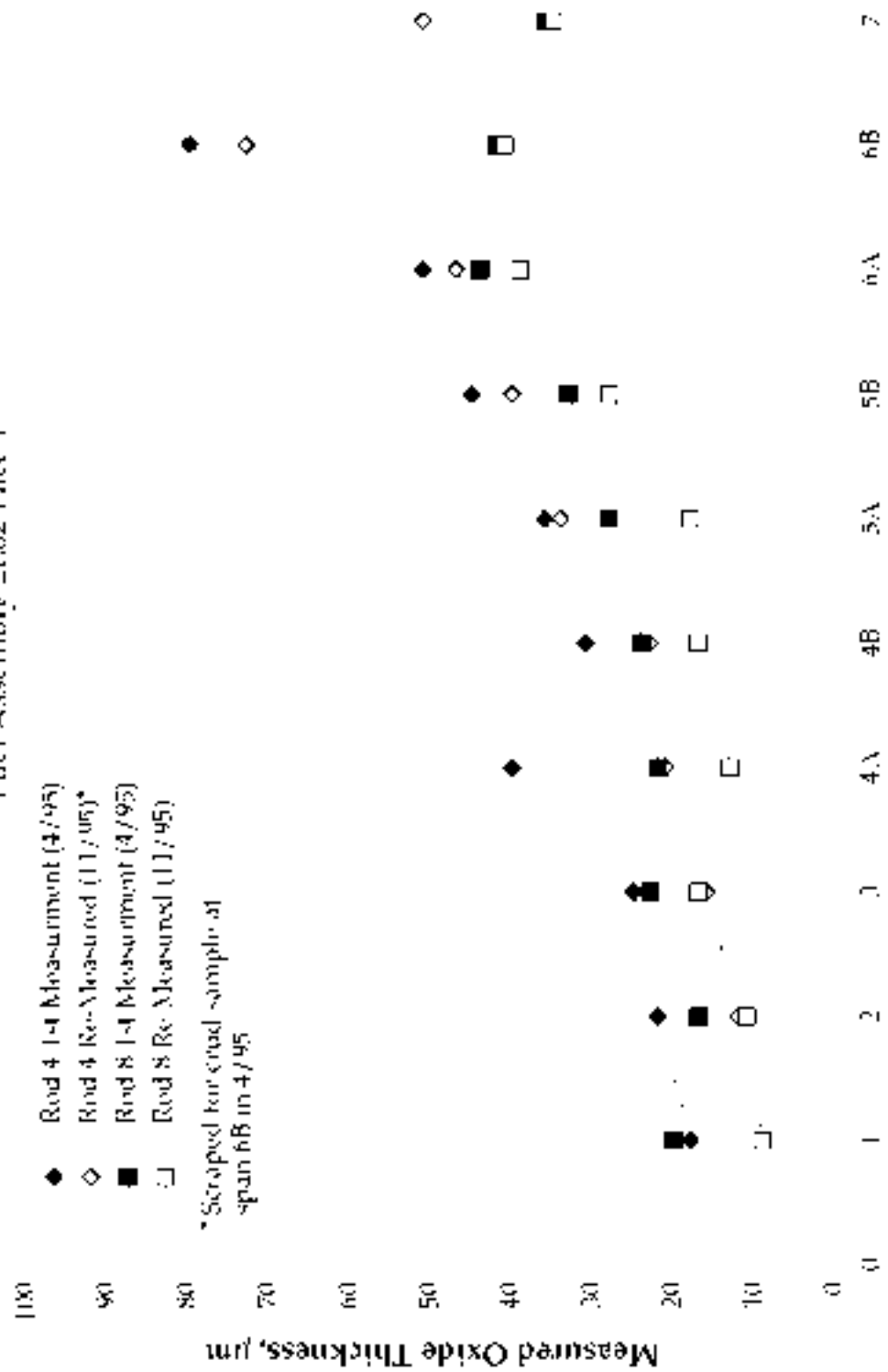

Figure 2-8 Comparison of oxide thickness profiles measured on rods 4 and 8 in fuel assembly 2L02 at Farley-2 EOC10 outage (April 1995) and November 1995

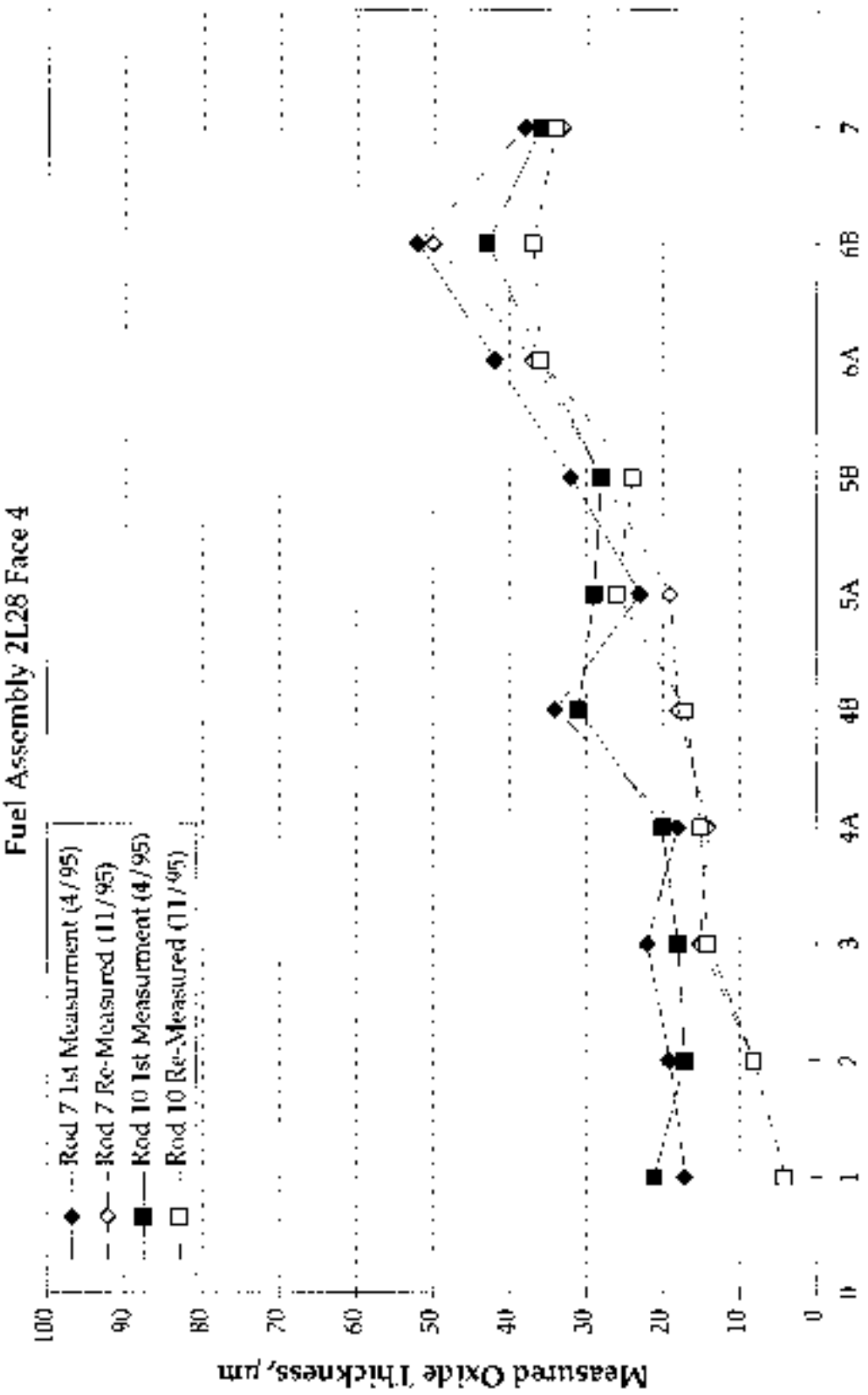

Figure 2-9 Comparison of oxide thickness profiles measured on rods 7 and 10 in fuel assembly 2L28 at Farley-2 EOC10 outage (April 1995) and November 1995

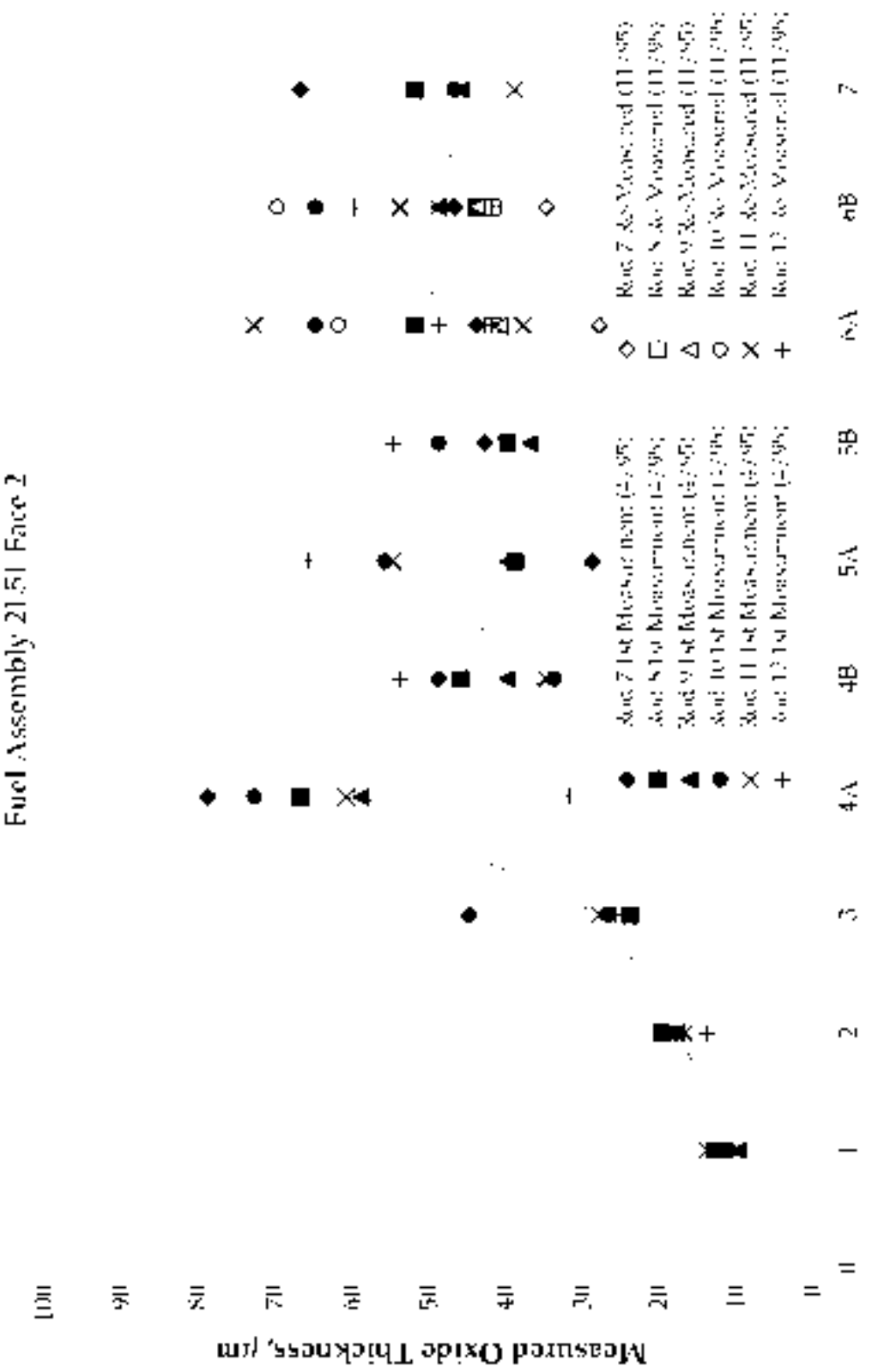

Figure 2-10 Comparison of oxide thickness profiles at spans 6A and 6B measured on rods 7, 10, and 11 in fuel assembly 21.51 at Farley 2 EOC10 outage (April 1995) and November 1995

2.3 WITHIN ASSEMBLY CORROSION VARIABILITY

A comparison of the oxide thickness values of adjacent rods on the same face of a fuel assembly can provide an insight of the presence of material variability or other unusual situations, since the adjacent rods should have generally experienced about the same physical and chemical duties during plant operation. The exceptions include different fuel rod design features and variable crud deposition patterns.

Figures 2-11 through 2-16 show comparisons of the rod peak oxide thickness values for the once, twice, and thrice burnt fuel in the F2C10 and F1C13 data base. Each column represents one peripheral face of a fuel assembly and the data points represent the rod peak oxide thickness at span 6A or 6B for Vantage-5 fuel or span 6 for standard fuel design. The cycle average radial peaking factor (PF1) for the rods measured is shown for each assembly. The number shown beneath the rod peaking factor is the sum of the radial peaking factors of the subject rod and its nearest neighbor in the adjacent assembly (PF12). It can be seen that the peak oxide values for adjacent rods within an assembly are generally within a small scatter band, except some once and twice burnt rods in the post-Zn F2C10 fuel. The two once burnt assemblies with larger data scatter bands , 2M19 and 2M56, also show anomalously higher oxide points at the peak span 6B, as seen in Figure 2-1. Thus, it cannot be certain whether the higher than expected oxide values in these two assemblies were due to a cladding material variability or a measurement interference due to the presence of the black deposit.

In the twice burnt assemblies in the F2C10 data, a total of 5 out of 134 rods in 4 assemblies had oxide exceeding 60 μm, see Figure 2-13. The two highest corrosion rods, in assemblies 2L02 and 2L51, were among the rods re-measured in absence of the black deposit in the November campaign. Thus, it is believed that at least some of the large data scatters in the F2C10 twice burnt fuel rods resulted from a material variability, since measurement repeatability was not an issue. For most assemblies, material variability as implied from comparing side-by side rods was not a significant issue. But, the very few higher corrosion rods (>60μm) in the twice burnt reload are suspected to result from a material variability because in most cases, only 1 or 2 out of 4 or 6 rods on the same assembly face showed unusually high corrosion. Another probable cause of corrosion variability among side-by-side rods is a variable crud deposition pattern, as induced by local thermal hydraulic conditions. The crud data available from this study, however, does not have enough information to allow such an assessment. Environmental (water chemistry) factors are not likely to be the reason for the variations seen in the F2C10 oxide measurements (Figure 2-11 and 2-13) because only a few assemblies exhibited large variability. Most of the assemblies with large variability were associated with the highest operating duty history. In some assemblies with the higher variability, the oxide measurements for those rods showed atypical axial variations which may possibly be attributable to local hydraulic effects or measurement anomalies.

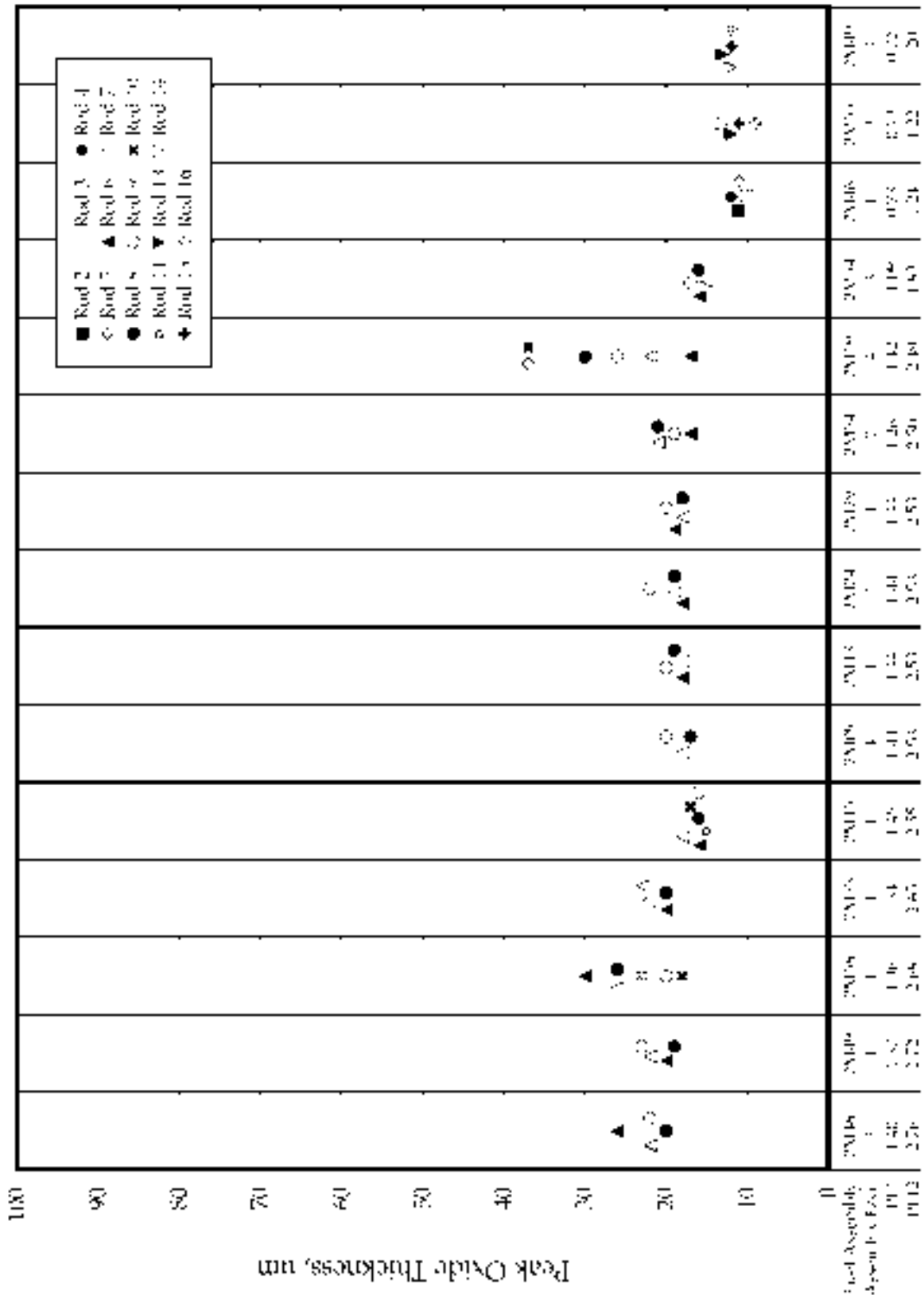

Figure 2-11 Rod peak (span a) oxide thickness for post-Zn P2C10 1 cycle rods in 15 assembly faces shown in decreasing value of PF12, the sum of peaking factor for subject rod and its nearest neighbor

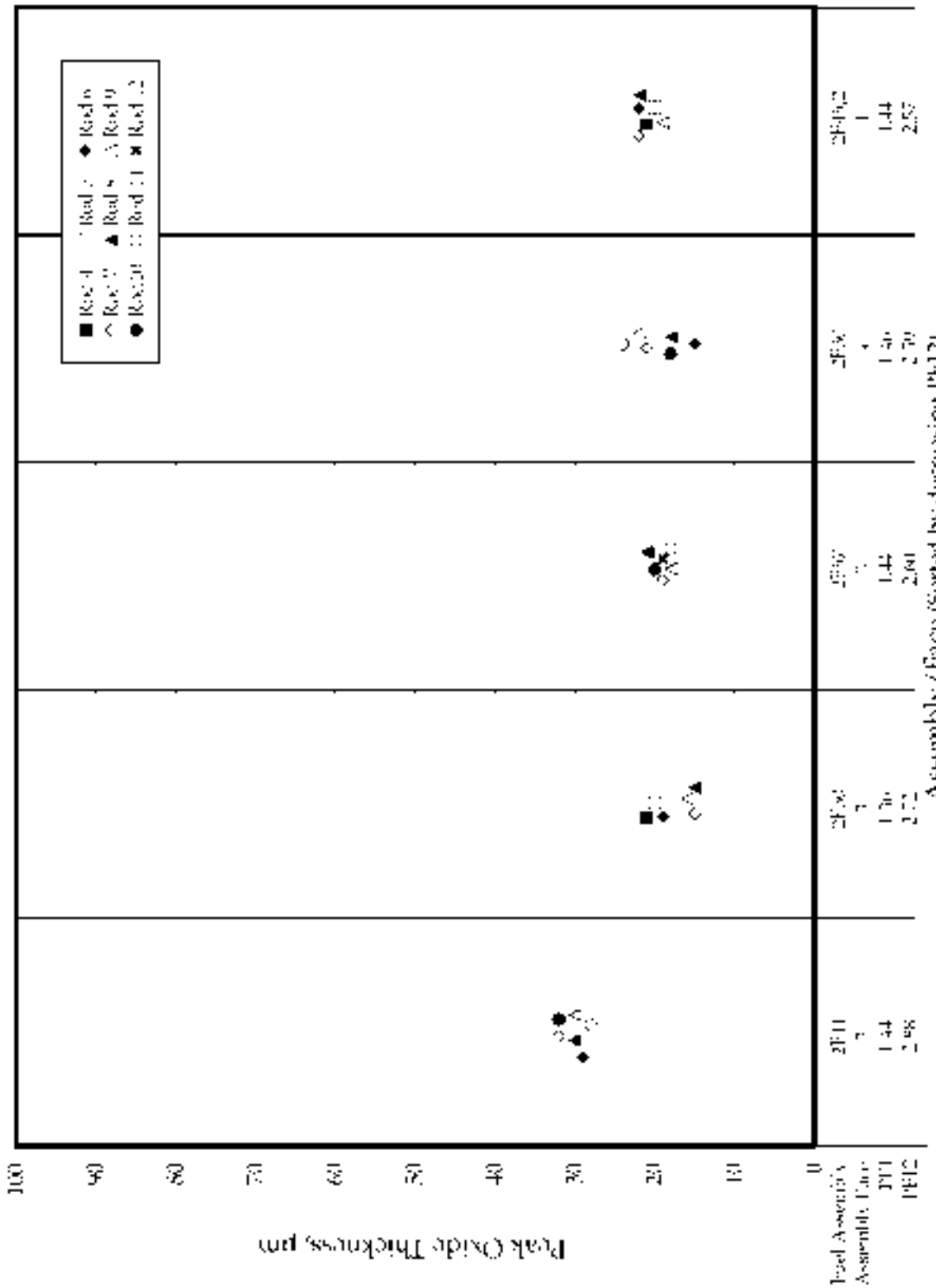

Figure 2-12 Rod peak (span 6) oxide thickness for non-Zn F1C13 1 cycle rods in 5 assembly faces shown in decreasing value of PF12, the sum of peaking factor for subject rod and its nearest neighbor

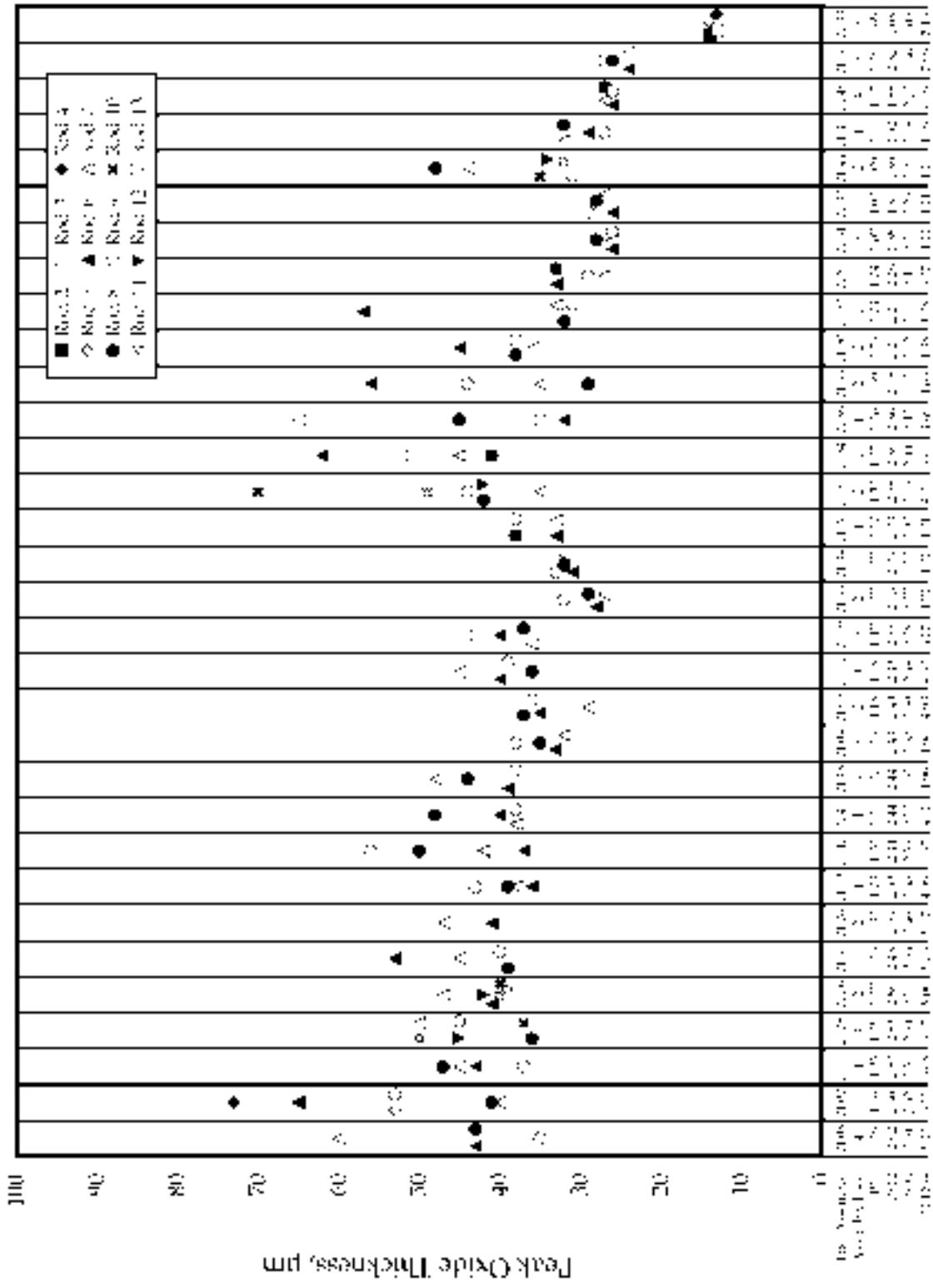

Figure 2-13 Rod peak (span 6) oxide thickness for Post-Zn E2C10 2 cycle rods in X2 assembly faces shown in decreasing value of PF1234, the sum of peaking factor for subject rod and its nearest neighbor during both cycles

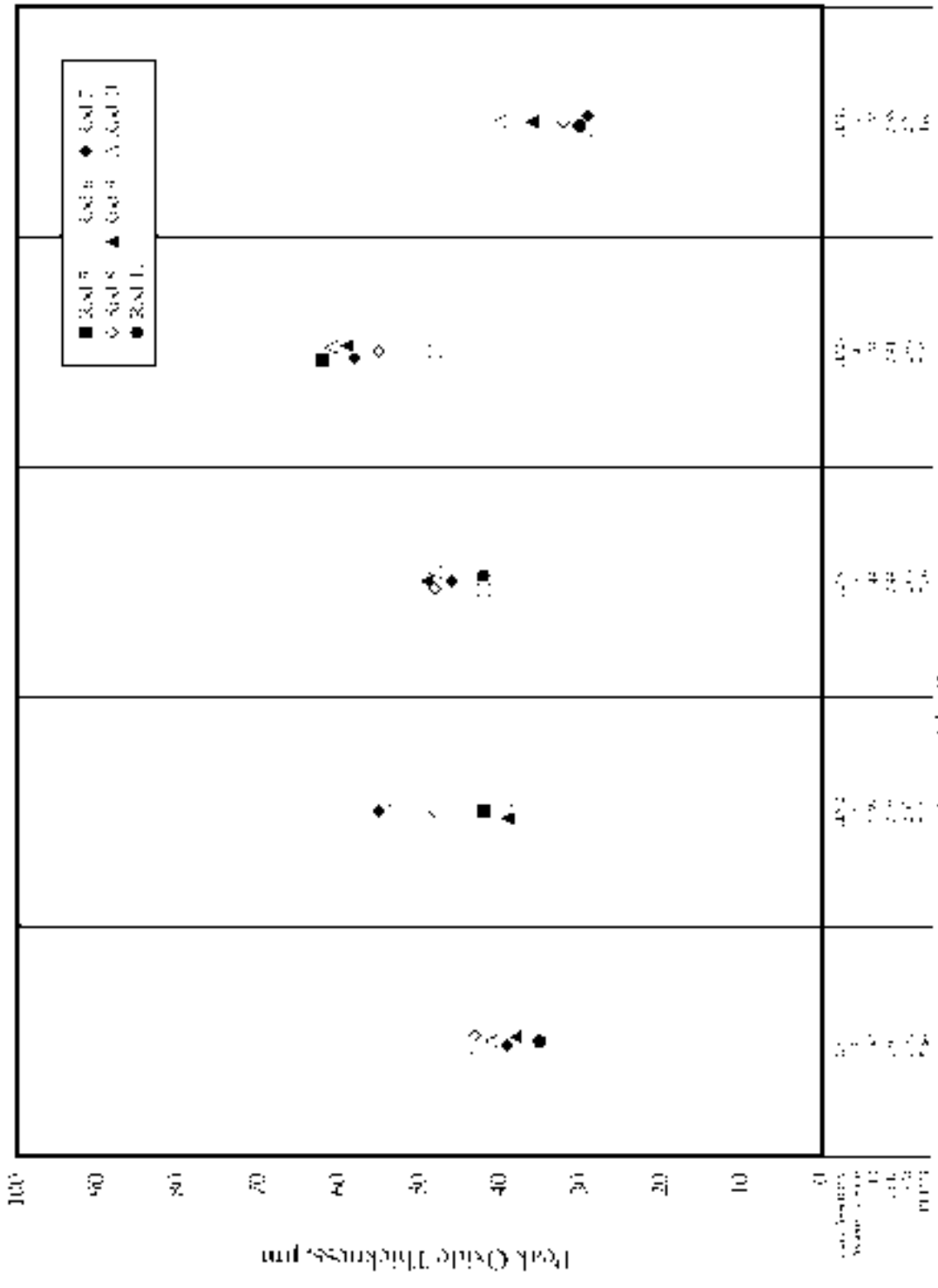

Figure 2-14 Rod peak lspan fc oxide thickness for non-Zn FC13 2 cycle rods in 5 assembly faces shown in decreasing value of PF1234, the sum of peaking factor for subject rod and its nearest neighbor during both cycles

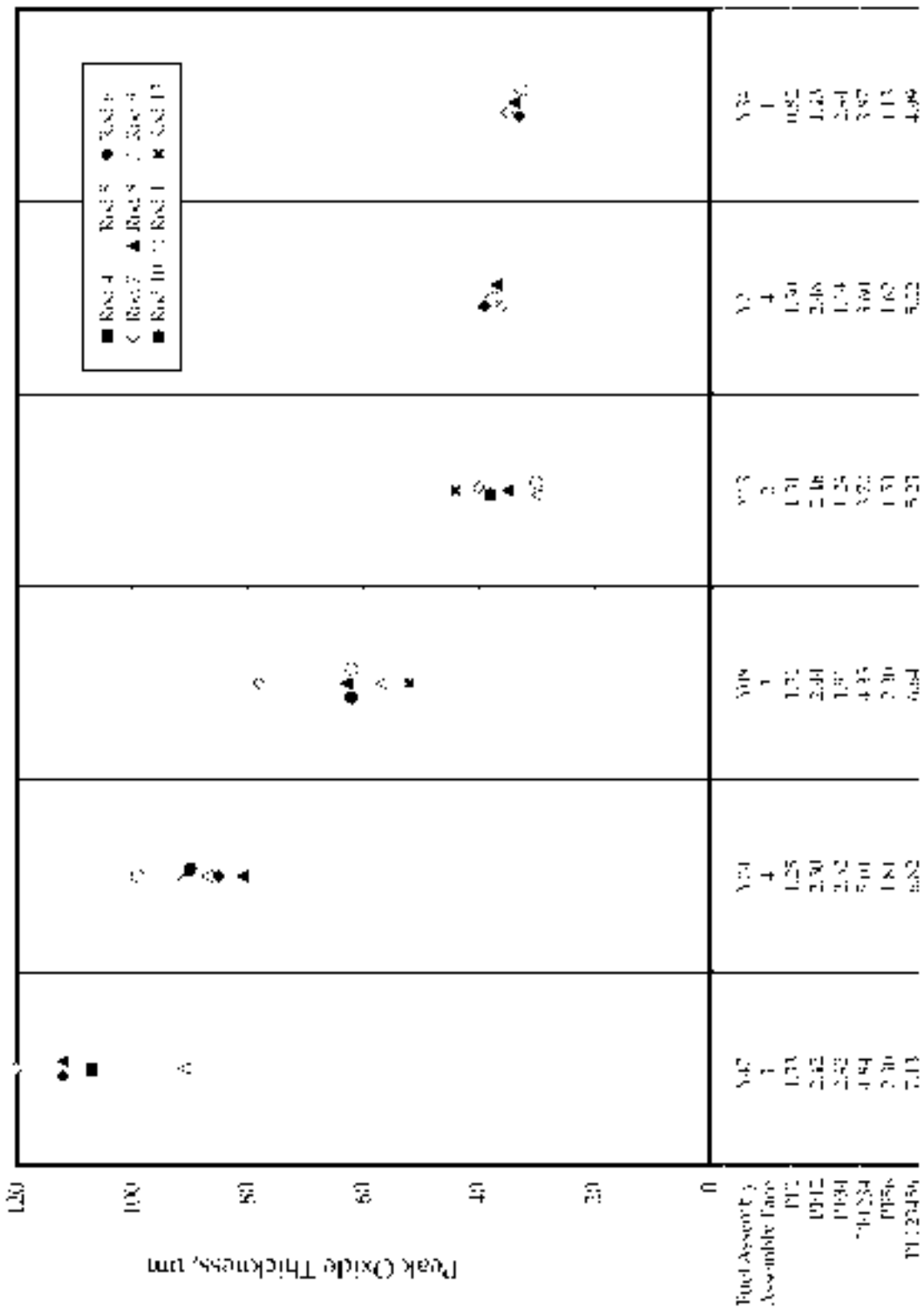

Figure 2-15 Rod peak (span 6) oxide thickness for post-Zn F2C11 3 cycle rods in 6 assembly faces shown in decreasing value of PF12456, the sum of peaking factor for subject rod and its nearest neighbor during 3 cycles

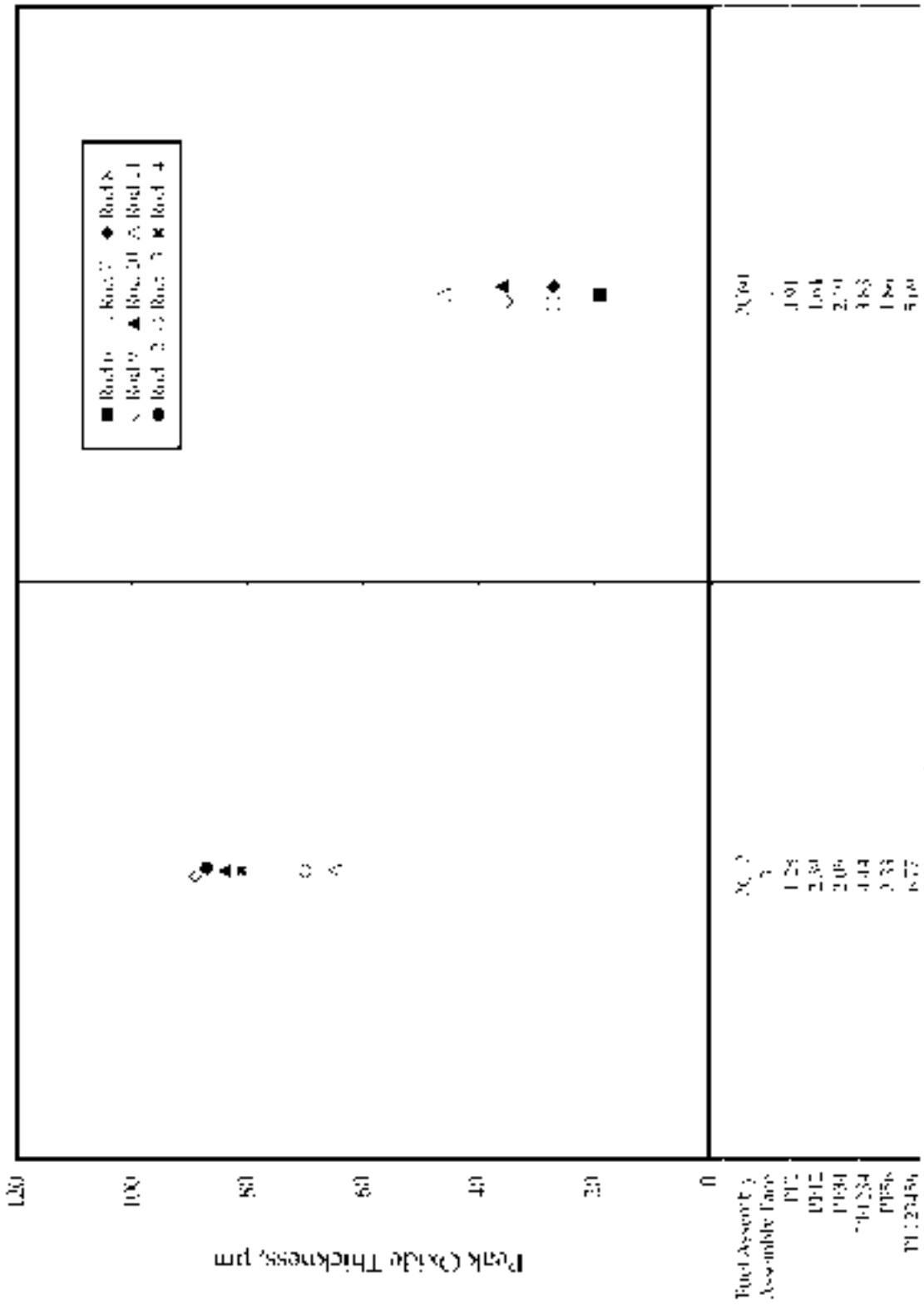

Figure 2-16 Rod peak (span 6) oxide thickness for non-Zn FIC13.3 cycle rods in 2 assembly faces shown in decreasing value of PF123456, the sum of peaking factor for subject rod and its nearest neighbor during 3 cycles

2.4 ASSEMBLY-TO-ASSEMBLY CORROSION VARIABILITY

The data shown in Figures 2-11 to 2-16 also provide a comparison of fuel rod corrosion from assembly to assembly within a reload. The comparison provides an insight of the effect of thermal/hydraulic duty, including in-core location, on fuel rod corrosion.

Figures 2-11 and 2-12 show the once burnt rods in the F2C10 and F1C13 data base, respectively. The data are plotted in a decreasing order of the sum of the peaking factors of the subject and nearest neighboring rods, PF12. A correlation of rod oxide thickness with PF12 can be seen, with the only exception, assembly 2M19 in F2C10 (Figure 2-11). The aberrant behavior of 2M19 is likely the result of measurement interference as shown in Figure 2-1 and discussed earlier. For assemblies with a PF12 value of <2.65, the rod peak oxide thickness was <~20-22μm. Only assemblies with a PF12 >2.65 had higher peak oxide thickness exceeding 22 and up to 32 μm. The high PF12 values (>2.65) resulted from a fresh assembly being placed next to another fresh assembly. Placing two fresh assemblies next to each other did not increase the rod corrosion if the PF12 value is low (<2.65) as shown for 2M54. The higher fuel rod corrosion for the high PF12 fuel is believed to result from simultaneous boiling of adjacent rods within the gap between two fresh assemblies. The results shown in Figures 2-11 and 2-12 also indicate that there was no difference in the oxide thickness between the once burnt rods of comparable T/H duty in the F2C10 and F1C13 fuel. In fact, the assembly having the highest average oxide thickness is 2E11 in F1C13, which had the highest PF12 among all once burnt rods measured. A similar comparison is not shown for F2C9 to F2C10, however, as described in Section 3 there are differences in the oxide thickness between once burnt rods of comparable T/H/ duty in those cycles.

For twice and thrice burnt fuel, the peaking factors of the rod and its nearest neighbor for each cycle all will contribute to the cladding oxide thickness. Figures 2-13 and 2-14 show the rod peak oxide thickness for the twice burnt assemblies for the F2C10 and F1C13 fuel. The data are arranged in the decreasing order of the sum of the peaking factors for the subject rods and its nearest neighbors in the adjacent assembly for both cycles, PF1234. The PF12 values for the first and second cycles are also shown. It can be seen that the assembly with the highest amount of corrosion in F2C10, 2L02, had the second highest PF1234 of 5.18. This assembly was placed next to another fresh assembly during the first cycle (Cycle 9) operation, and was next to a fresh assembly with a high peaking factor during the second cycle (Cycle 10). Assemblies with the second highest amount of corrosion, 2L54 and 2L51, were also placed next to a fresh assembly during the first cycle and had the highest PF12 for the first cycle, although its neighbor during the second cycle was not a fresh assembly, resulting in a relatively low PF1234 value of only 4.87. The PF1234 and the first cycle PF12 were both higher in the F1C13 twice burnt rods, but a correlation between the rod corrosion and the PF values cannot be clearly established. However, the assembly with the thickest oxide, 2D29, had the highest rod peaking factor of 1.20 among all the F1C13 2 cycle assemblies (Table A8) during its second cycle (Cycle 13) of operation, again suggesting the

importance of thermal duty in determining the oxide thickness. Corrosion of the thrice burnt rods also show a clear correlation with the cumulative rod power history, Figure 2-15 and 2-16.

The assembly-to-assembly corrosion comparisons indicate that placing high power fresh assemblies adjacent to each other will increase the thermal duty of the peripheral rods, resulting in higher cladding corrosion. It is less clear how a small increase in the thermal duty will substantially increase the cladding oxide thickness. This subject is further discussed later.

3

OXIDE DATA INTERPRETATION USING PFCC MODEL

3.1 METHODOLOGY AND ACCURACY OF PFCC MODEL

The rod peak oxide thickness for the three sets of data shown in the tables in Appendix B are plotted as a function of the rod average burnup, Figure 3-1. It can be seen that the post-Zn F2C10 cladding oxide data appear to be generally higher than the pre-Zn F2C9 data at comparable burnups. Similarly, a few of the twice burnt data in the post-Zn F2C10 fuel also appear to be higher than comparable non-Zn F1C13 data. The differences between the three data sets are, however, too subtle to allow an intuitive assessment of whether zinc injection contributed to the apparently higher cladding oxide values in the F2C10 data. This is because the subtle differences could have resulted from differences in the fuel operational duty, cladding material, and a statistical bias due to a different size data set. To normalize the differences in fuel duty, the EPRI PFCC model was employed to calculate the predicted oxide thickness. The differences between the predicted and measured rod peak oxide are compared and a statistical analysis is performed to assess whether the Zn injection in Cycle 10 resulted in a different behavior in cladding corrosion.

The PFCC model is a parametric corrosion model incorporating factors which have been known to contribute to in-reactor corrosion of Zircaloy cladding. The relative weight of each parameter was quantified using a set of fuel rod corrosion data from five reactors for benchmarking and qualification[3-4]. The factors incorporated in the PFCC model are shown schematically in Figure 3-2. For calculation of the fuel rod wall temperature, and hence the corrosion controlling metal-oxide interface temperature, T_{MO}, a single channel thermal hydraulic (SCM) code is included in PFCC[4]. Inputs to the SCM code include the operational histories of fuel rod radial and axial peaking factor, fuel rod and assembly design parameters, plant power history and thermal/hydraulic parameters. No flow turbulence and mixing of water from outside of the channel are assumed in the SCM code. The wall temperature of a rod is calculated by assuming that the water surrounding the rod is heated by the enthalpy output from the subject rod and parts of its surrounding 8 rods. Thus, some coupling effects of surrounding rods are included in the calculation. Calculations performed to take into account the thermal coupling effect of neighboring rods are included in calculations of heated rod diameter for each rod as shown in Appendix A. It should be noted that, since inter-channel

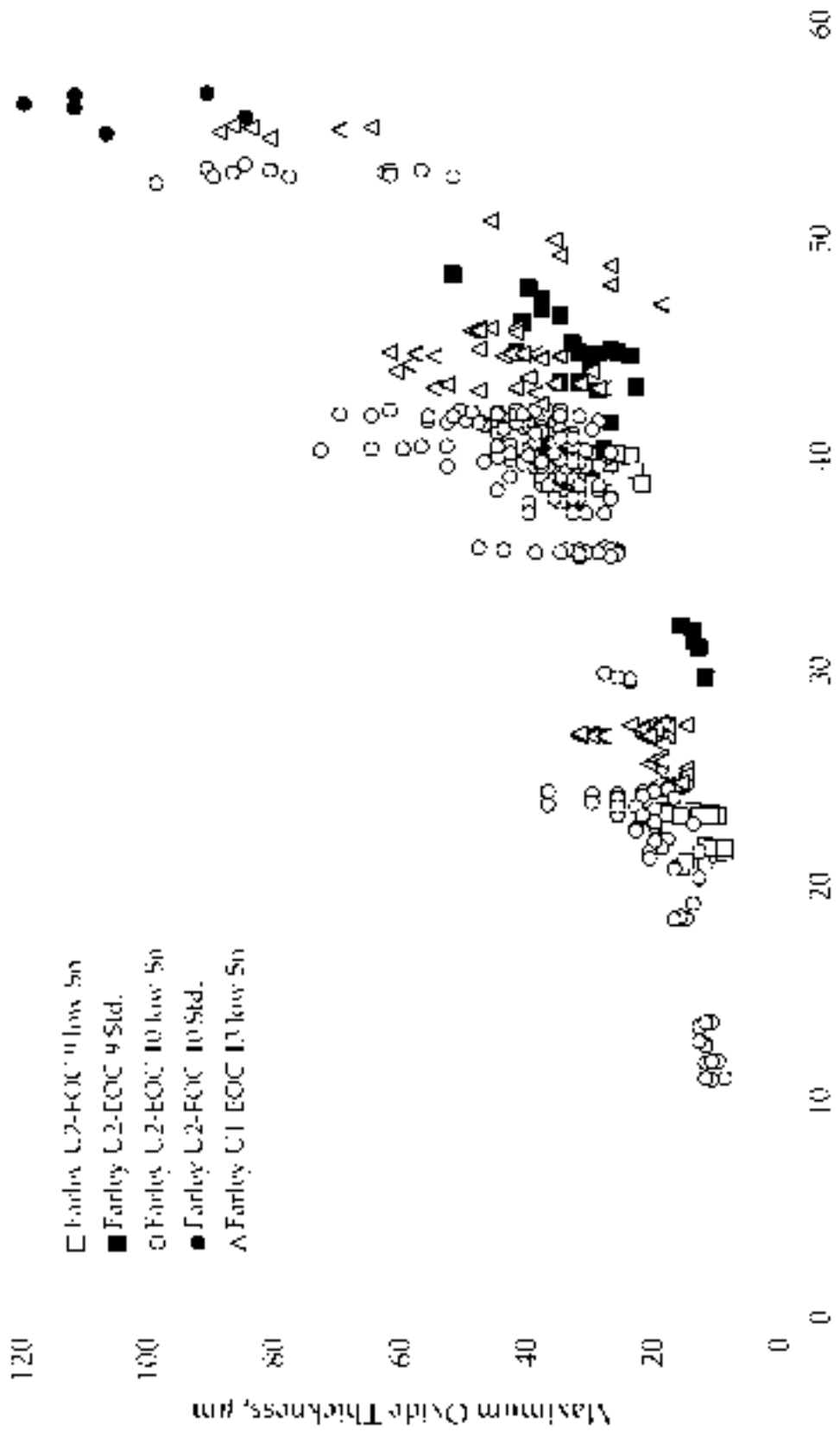

Figure 3-1 Rod peak oxide thickness as a function of rod average burnup for Farley-1 EOC13, and Farley-2 EOC9 and 10 data

mixing is not included in the SCM model, under-prediction of the wall temperature may exist when boiling takes place on a fuel rod surface. (VIPRE or an equivalent model is needed to treat flow mixing.) This may be the case for some of the high peaking rods in the present study as will be discussed later.

Appendix A shows the fuel parameters, including power histories, RCS Li histories, and axial peaking factors used in the PFCC calculations for the rod peak oxide thickness. The predicted peak oxide thickness values are shown in Appendix B.

The accuracy of oxide thickness prediction using PFCC or any other models is determined by the accuracy of the corrosion rate, T/H treatments in the model, and the input data. The overall accuracy of the PFCC model for predicting the rod peak oxide thickness is illustrated in Figure 3-3 for the 45 benchmark and qualification rods used for PFCC development[(4)]. It can be seen that the accuracy is within ±20 μm over the measured oxide thickness range of 100 μm. The 6 circle points close to the +20 μm line came from the initial core fuel at Millstone-3 using standard Zircaloy-4 cladding. It is believed that this cladding lot was more susceptible to corrosion causing significant under-prediction. Excluding this cladding lot, the majority of the predicted oxide thickness values were within ~±10 μm of the measured values. It should be noted that the model was adjusted to provide a slight conservatism at the higher thickness regime. In general, prediction accuracy increases with better knowledge in cladding manufacturing characteristics and better accuracy in input data. One limitation of this PFCC version is its treatment of cases where boiling-induced crud deposition and chemical hideout takes place. All but 4 out of the 45 benchmark and qualification rods had a peak heat flux of <96 W/cm^2, suggesting no boiling on the rod surface. The 4 high power rods had a peak heat flux ranging 100-104 W/cm^2. Although those 4 rods were predicted to have some degrees of subcooled boiling, the rods were reported to be free of deposits, and the cladding corrosion was within the range expected from model calculations.

Many of the Farley-1 EOC13, Farley-2 EOC9 and EOC10 rods had a peak heat flux of >100 W/cm^2 during the first cycle, and subcooled boiling was predicted. The thermal duty was highest for F1C13 rods and lowest for F2C9 rods. Figure 3-4 shows the axial profiles of the rod wall temperature for rod #9 on face #1 in F2C10 assembly 2M15. It can be seen that the rod wall temperature exceeded the system saturation temperature of 343.5°C at spans 6 and 5 throughout the whole cycle.

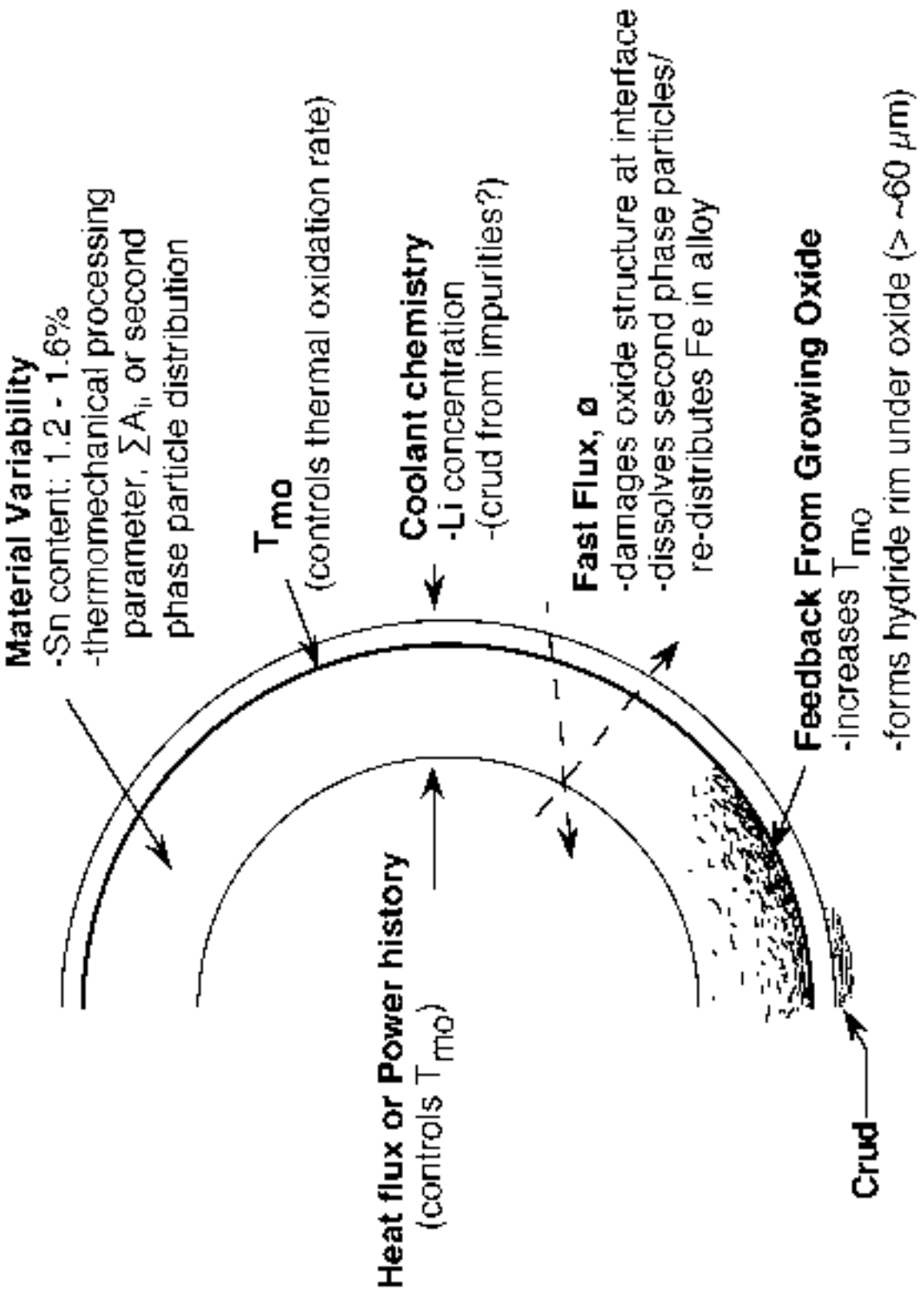

Figure 3-2 Factors known to contribute to zircaloy cladding corrosion

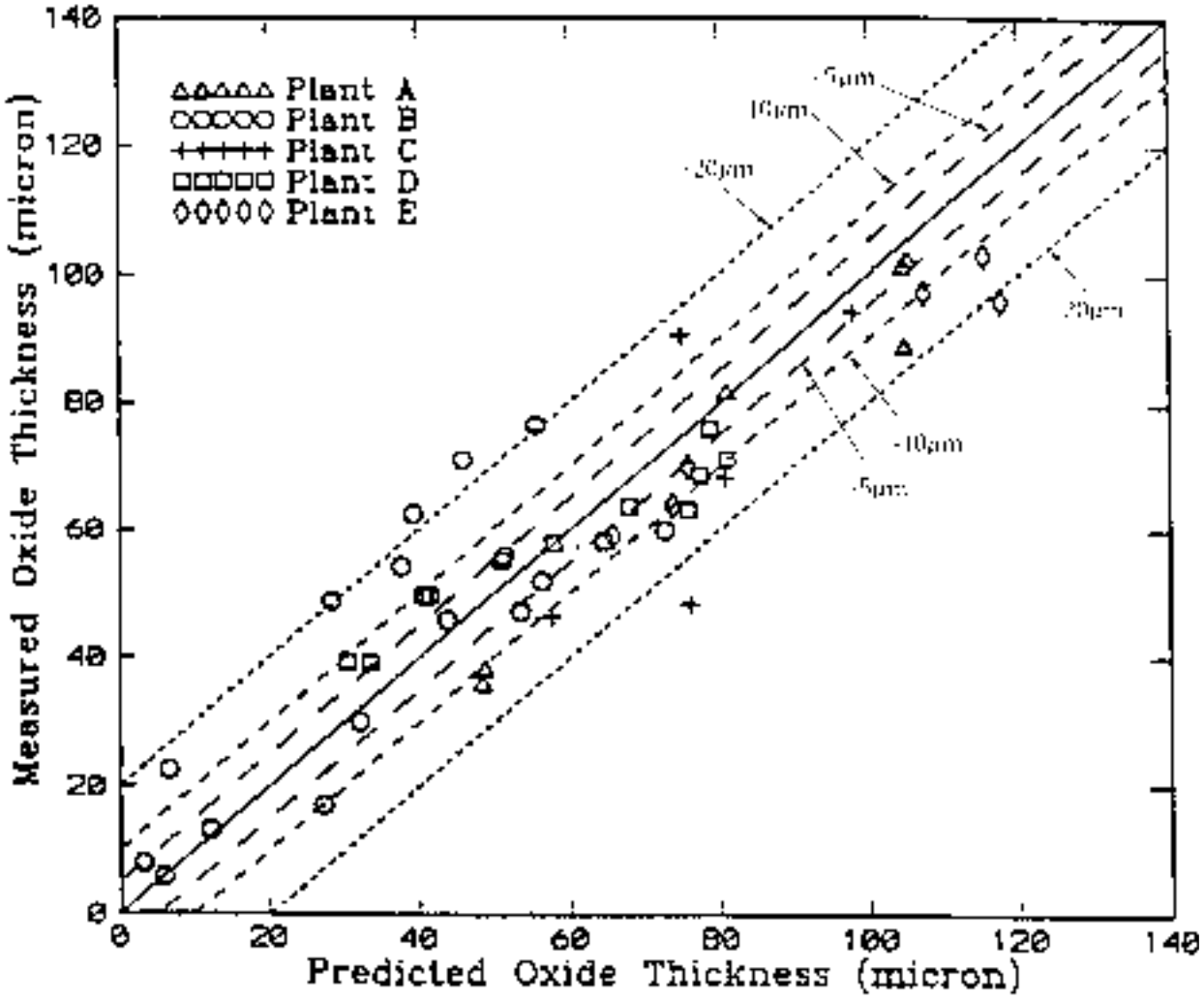

Figure 3-3 Measured vs. Calculated peak oxide thicknesses of 45 benchmark and qualification rods

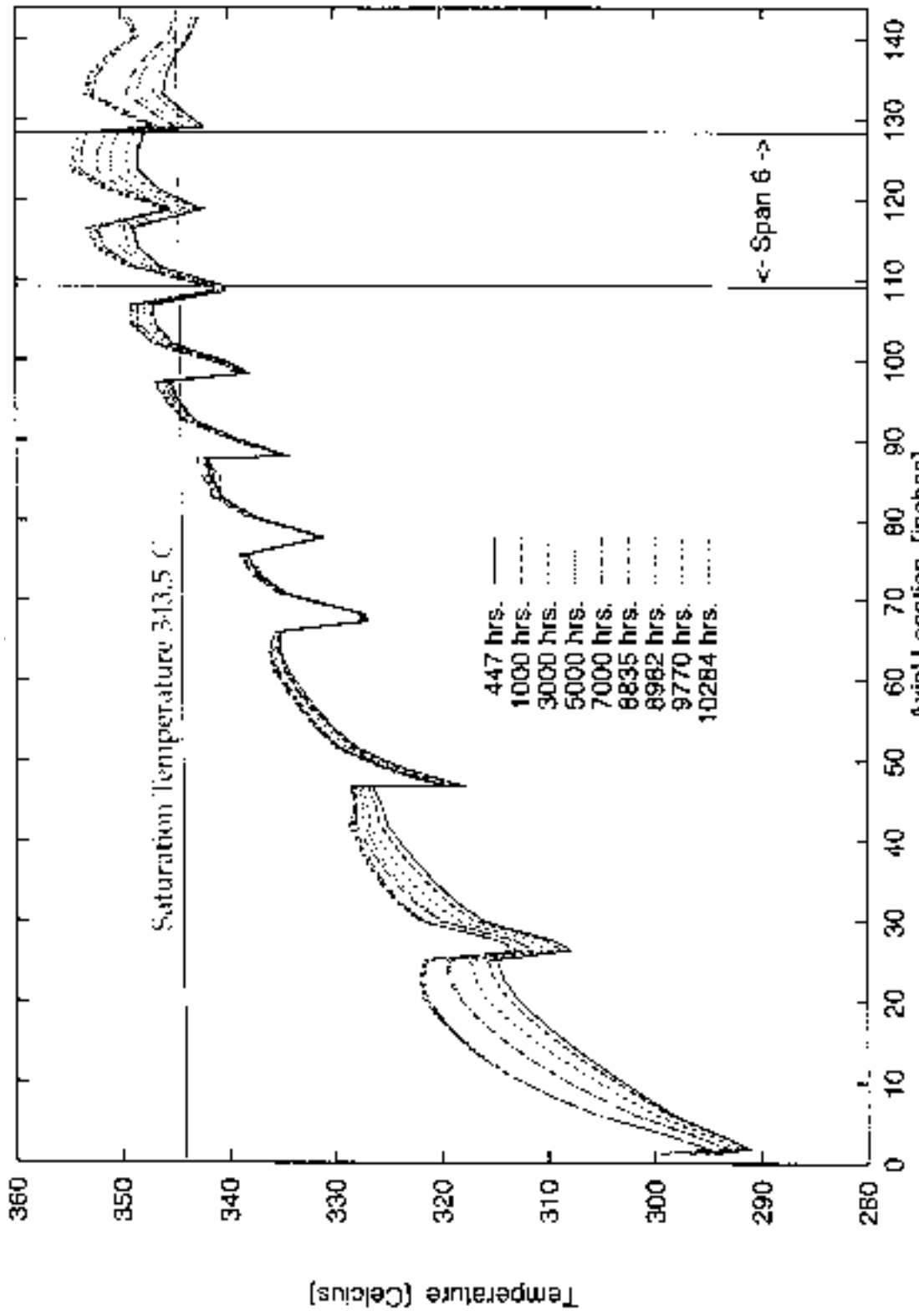

Figure 3-4 Metal/Oxide interface temperature distributions for 2V115F1R9

3.2 COMPARISON OF MEASURED AND PREDICTED OXIDE THICKNESS

The PFCC calculated peak oxide thickness for spans 6A and 6B or 6 are shown in the tables in Appendix B. Relevant information, such as the radial peaking factors for each rod are shown in tables in Appendix A.

The measured oxide thickness values are plotted against the PFCC predicted values in Figures 3-5 to 3-15. For Vantage-5 rods with IFM grids, two data points for each rod, one each from spans 6A and 6B, are shown in the figures.

3.2.1 Once Burnt Rods

Figures 3-5 to 3-7 show the measured versus predicted oxide thickness values for the once burnt rods in F2C9, F2C10, and F1C13, respectively. It can be seen that the pre-Zn F2C9 rods, Figure 3-5, behaved as-predicted from the PFCC model, with an average shift of only 1 μm from the prediction (solid) line. The standard deviation was 2.9 μm. All measured data fall within the ±10 μm lines. The average shift, $\bar{x}$, and the standard deviation, σ, are calculated using the formula shown in Appendix C.

The post-Zn F2C10 data, Figure 3-6, had on average 8 μm higher than the predicted values, and a standard deviation of 4 μm. The non-Zn F1C13 data, Figure 3-7, had a similar positive bias of 7 μm and a standard deviation of 5 μm. Although the majority of the data were within the ±10 μm lines, both data sets had a small portion which exceeded the +10 μm line. The two highest points in the F2C10 data, Figure 3-6, may have been affected by measurement biases as discussed earlier.

The results indicate that the once burnt fuel in the post-Zn F2C10 data behaved essentially the same as the non-Zn F1C13 data. Both the post-Zn F2C10 and non-Zn F1C13 data were on the average 6-7 μm higher than the pre-Zn F2C9 data.

3.2.2 Twice Burnt Rods

The twice burnt pre-Zn F2C9 rods were from Standard assemblies (not Vantage-5). The measured oxide values were on the average 5 μm less than the PFCC predicted values, Figure 3-8. Essentially all data fall within the ±10 μm accuracy limit. Thus, the pre-Zn F2C9 behaved as predicted.

The measured oxide thickness values were on the average 6 and 3 μm higher than the predicted values for the F2C10 and F1C13 data, respectively, Figures 3-9 and 3-10. Again, the majority of the data behaved as predicted within the ±10μm lines. It appears that the post-Zn F2C10 data had substantially more points exceeding the +10 μm line. However, this is anticipated as there are 7.4 times more points in the F2C10 data. In

fact, a smaller standard deviation of 7 µm for the F2C10 data, as compared to the 10 µm value for the non-Zn F1C13 data, also indicates that the apparently higher population of high oxide data points in the F2C10 data set is statistically anticipated. The only potential engineering significance between the two data sets are the 5 highest points (>60 µm) in the F2C10 data. However, those five points came randomly from 4 different assembly faces, as shown in Figure 2-13, suggesting no clear systematic trend due to an effect from the RCS, such as the Zn addition.

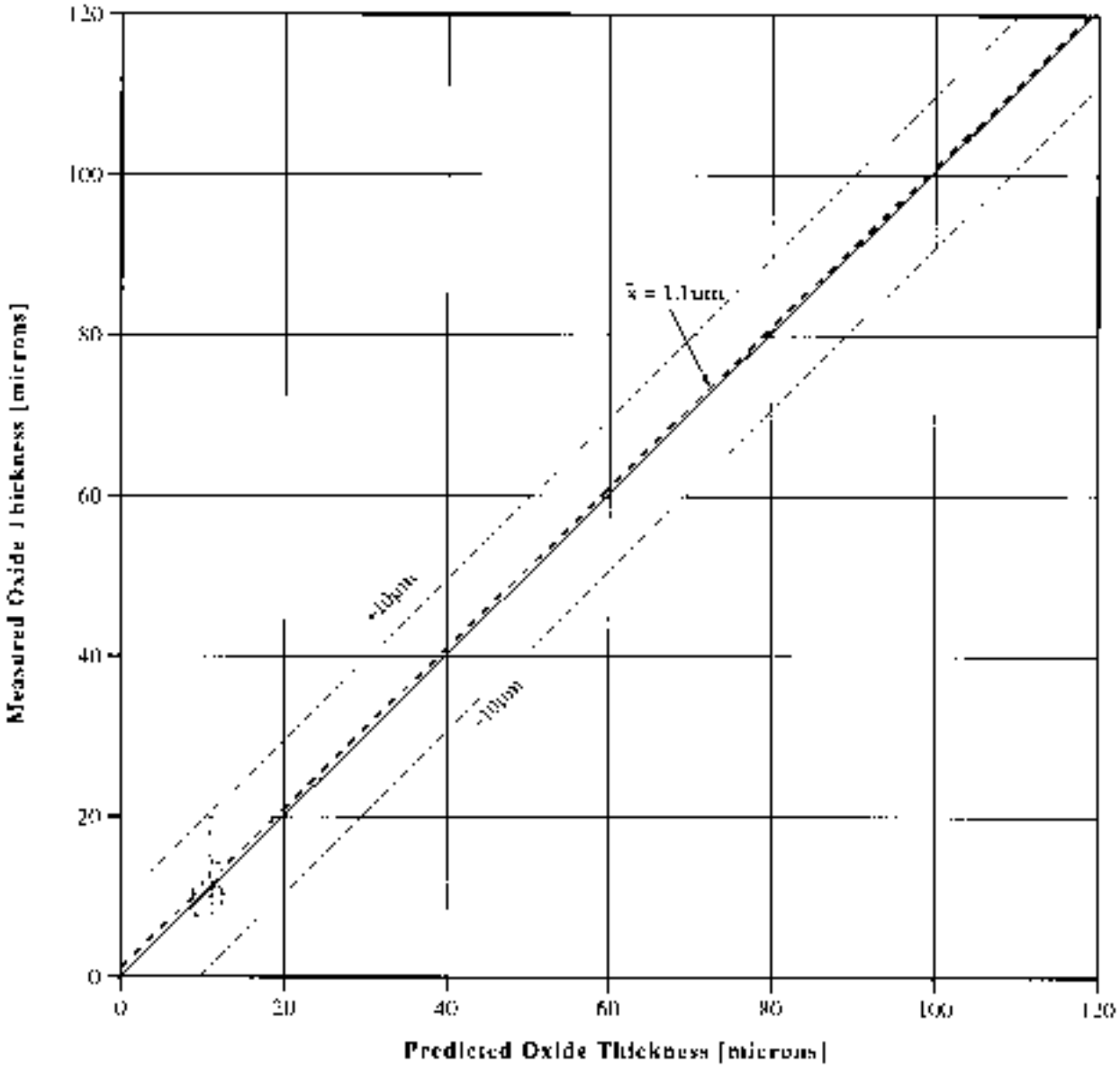

Figure 3-5 Pre-Zn F2C9 1 cycle rod oxide thickness at span 6

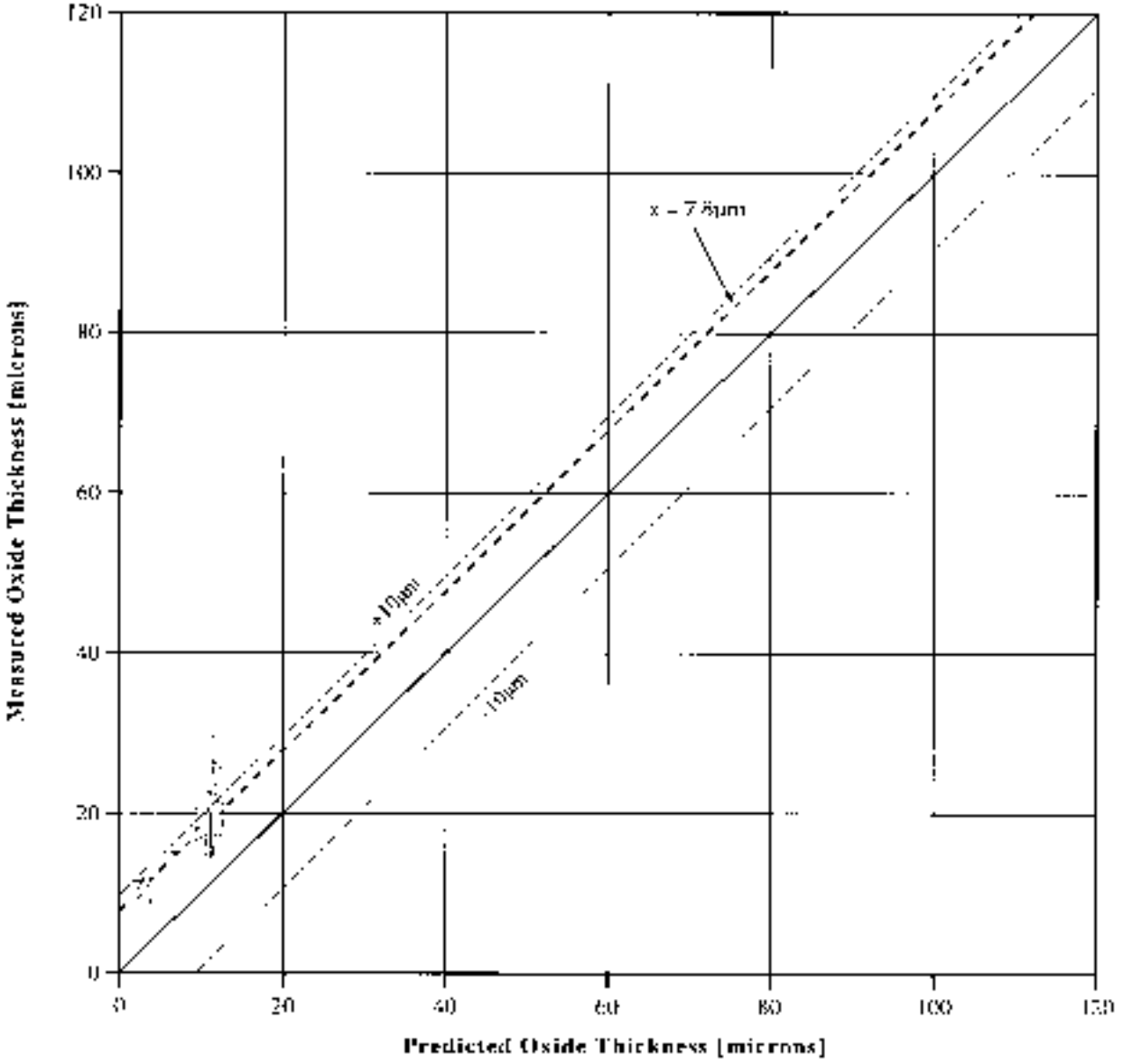

Figure 3-6 Post-Zn F2C10 1 cycle rod oxide thickness at span 6

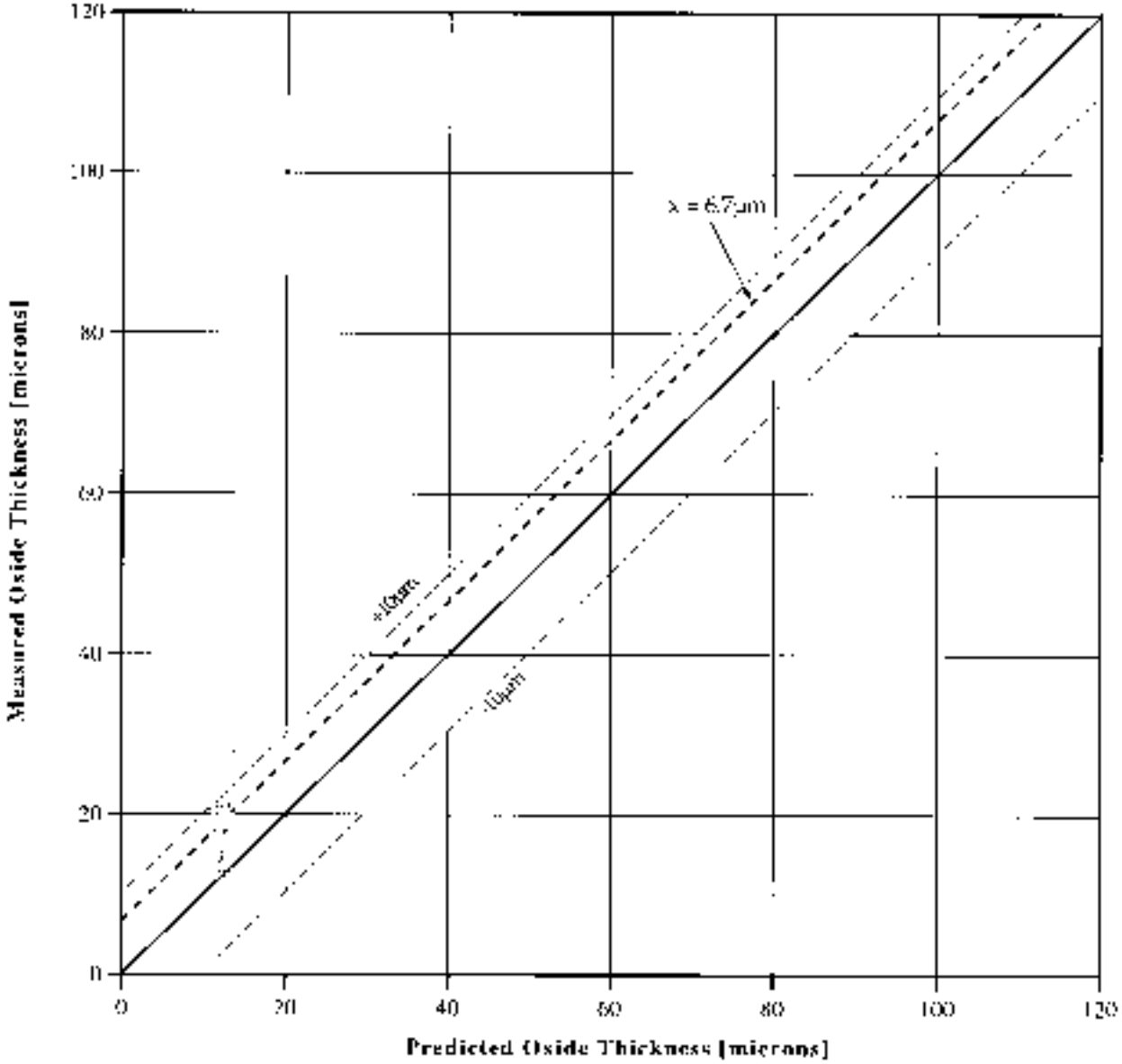

Figure 3-7 Non-Zn F1C13 1 cycle rod oxide thickness at span 6

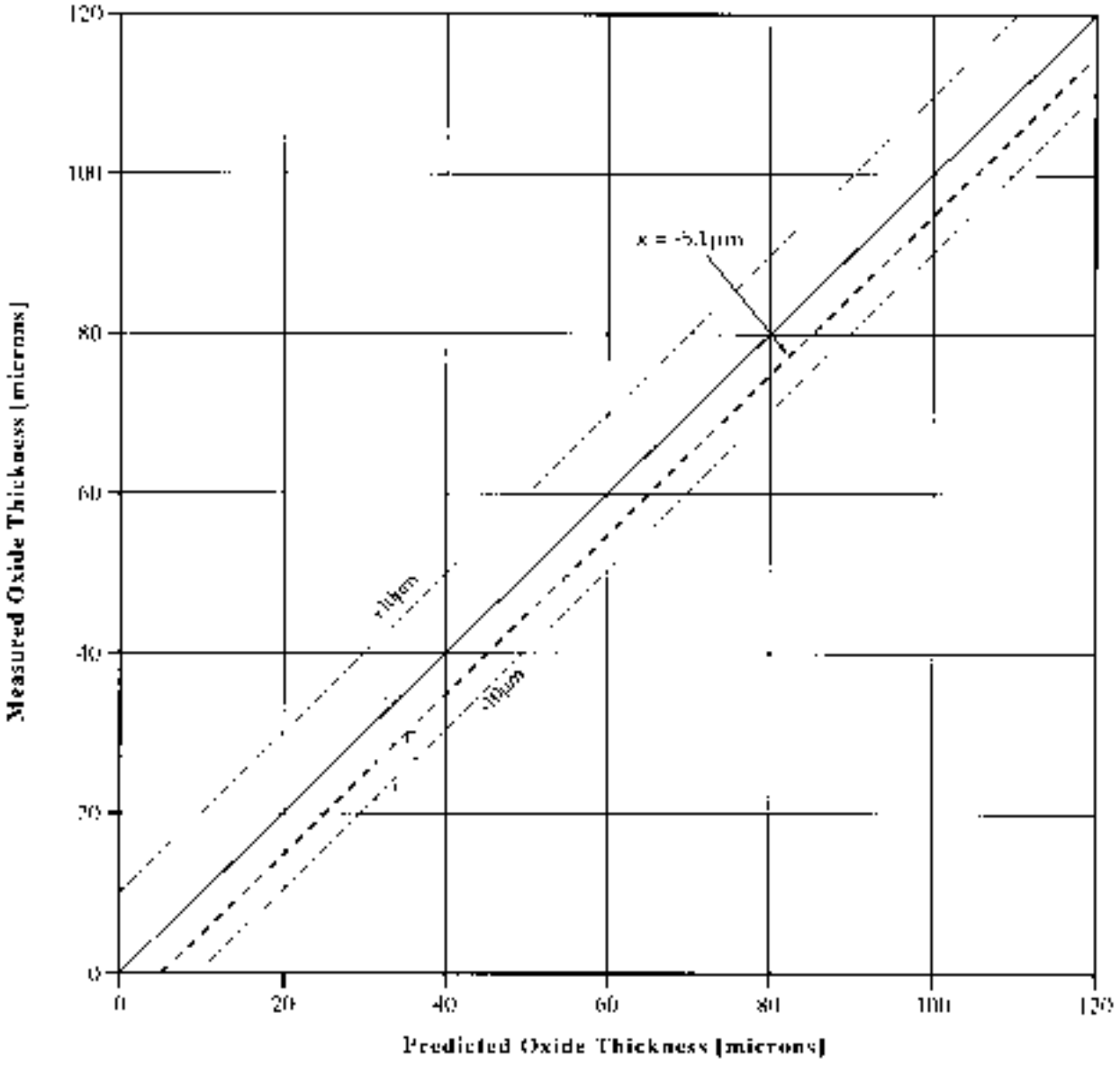

Figure 3-8 Pre-Zn F2C9 2 cycle rod oxide thickness at span 6

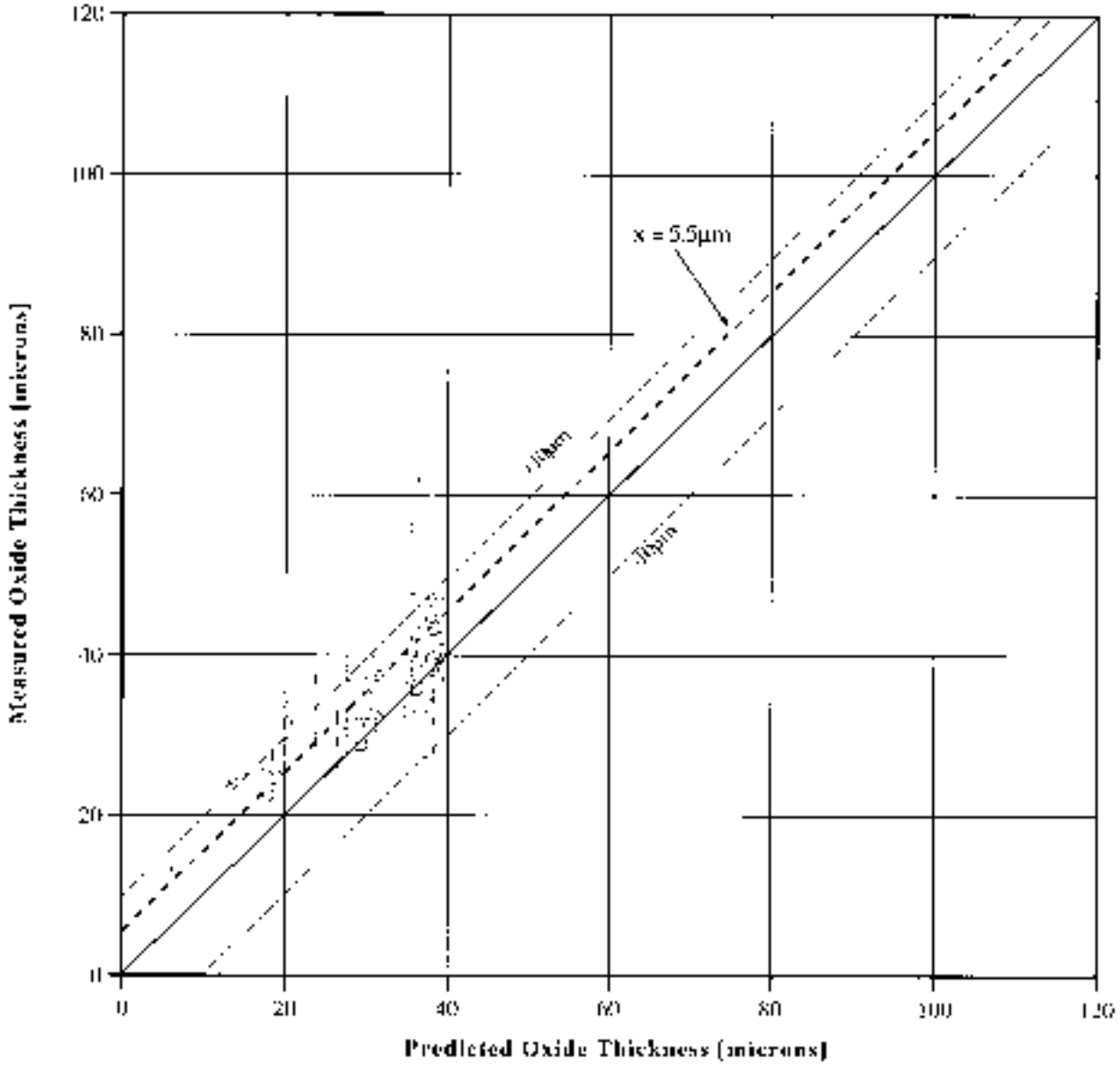

Figure 3-9 Post-Zn F2C10 2 cycle rod oxide thickness at span 6

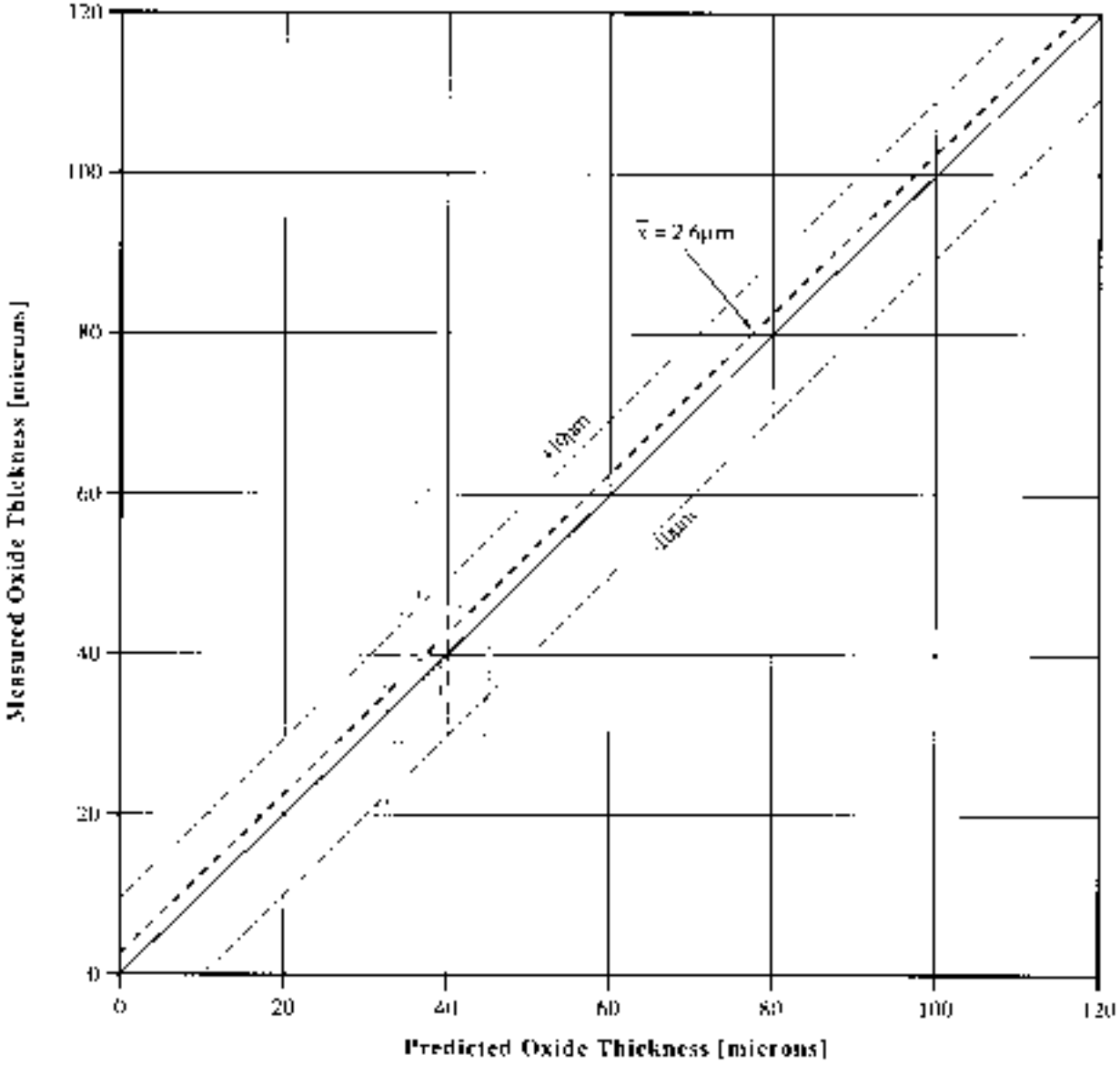

Figure 3-10 Non-Zn F1C13 2 cycle rod oxide thickness at span 6

The twice burnt data in the three sets of data again indicate that both the post-Zn F2C10 and non-Zn F1C13 rods behaved similarly. Both are on the average 3-6 μm higher than the PFCC prediction, and both are 8-11 μm higher than the pre-Zn F2C9 data. A few high corrosion rods in the F2C10 fuel could have resulted from factors other then Zn injection, such as material variability.

3.2.3 Thrice Burnt Rods

The thrice burnt oxide data for the F2C10 and F1C13 rods are shown in Figures 3-11 and 3-12, respectively. The F2C9 data did not contain any trice burnt low Sn cladding and are thus not included in this comparison. Both sets were from low tin rods in Standard fuel assemblies, so only the rod peak oxide data at span 6 are shown. As shown in the figures, most data fall within the ±20 μm lines, except 3 points in the F2C10 data. The average shift from the PFCC predicted values is 0.3 and -6 μm for the F2C10 and F1C13 data, respectively. The standard deviations of 12-13 μm for both thrice burnt data sets are relatively larger than that of the lower burnup rods, reflecting fewer data points and an increased uncertainty in the input data, and a greater scatter in measured oxide thickness at higher burnups.

The thrice burnt data again indicate that the post-Zn F2C10 and the non-Zn F1C13 rods behaved similarly and were generally within prediction of the PFCC model. In the F2C10 data, three rods had measured oxide data higher than the predicted values by 20 μm. But the data base is small in both cases.

3.3 COMPOSITE MEASURED VS. PREDICTED OXIDE DATA

The composite data for the F2C9, F2C10 and F1C13 low Sn rods are shown in Figures 3-13, 3-14, and 3-15, respectively.

As can be seen, there are substantially more points and also larger scatter in the F2C10 data, giving an impression of larger deviations from the PFCC predictions than the F2C9 and F1C13 data. A statistical interpretation, however, suggests that both F2C10 and F1C13 are comparable as the percentage of data exceeding the +20 μm line are about the same 3% (14 out of 428 and 4 out of 132 points for F2C10 and F1C13, respectively). When a linear regression analysis is performed, the best fitted lines for the F2C10 and F1C13 data are nearly the same as shown in Figures 3-16 and 3-17, respectively. Comparison of the regression line with the solid line in the figures indicates that the PFCC model, on the average, slightly under-predicts the F2C10 data in the thin oxide (lower burnup) regime and slightly over predicts the thicker

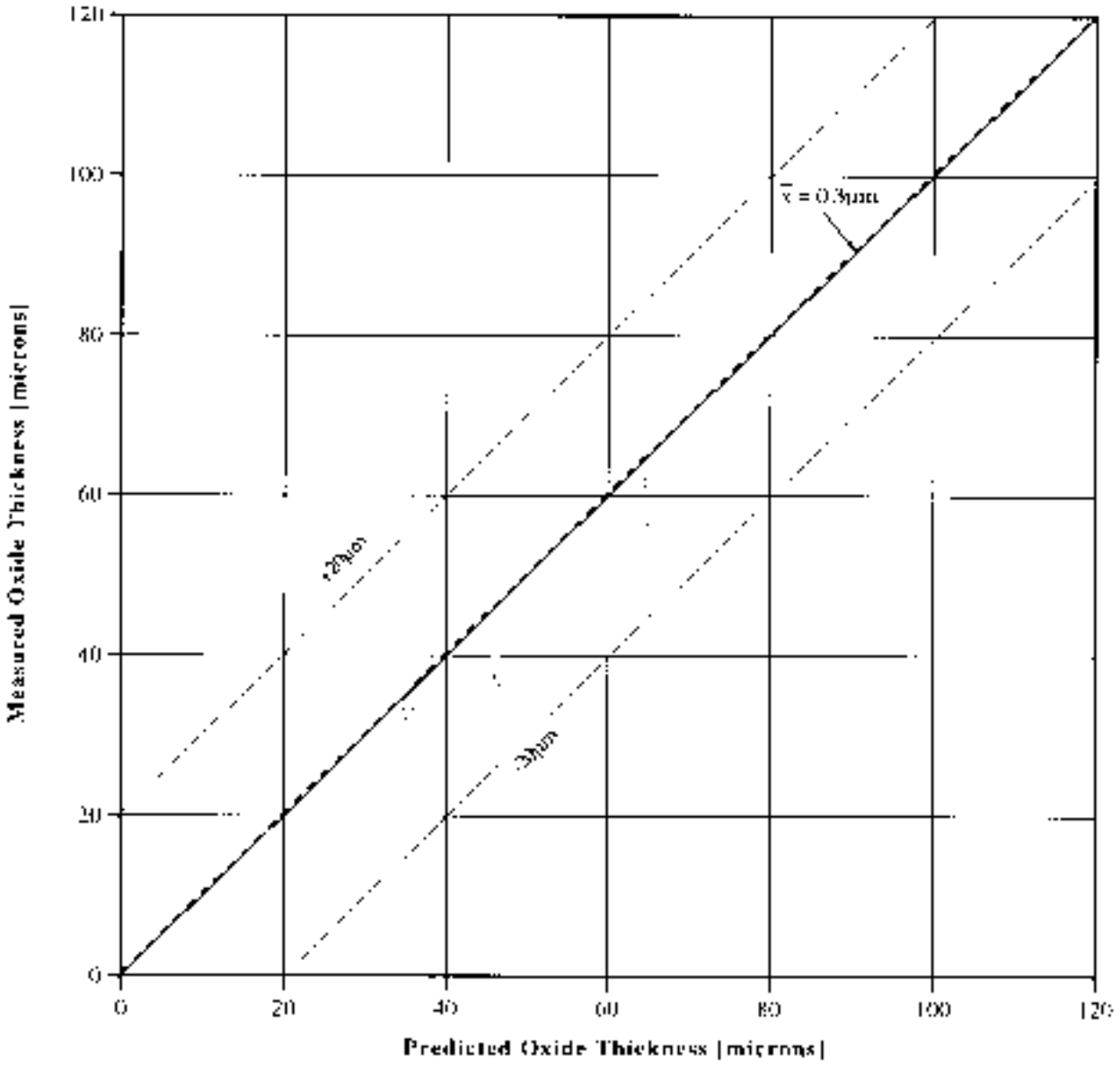

Figure 3-11 Post-Zn F2C10 3 cycle rod oxide thickness at span 6

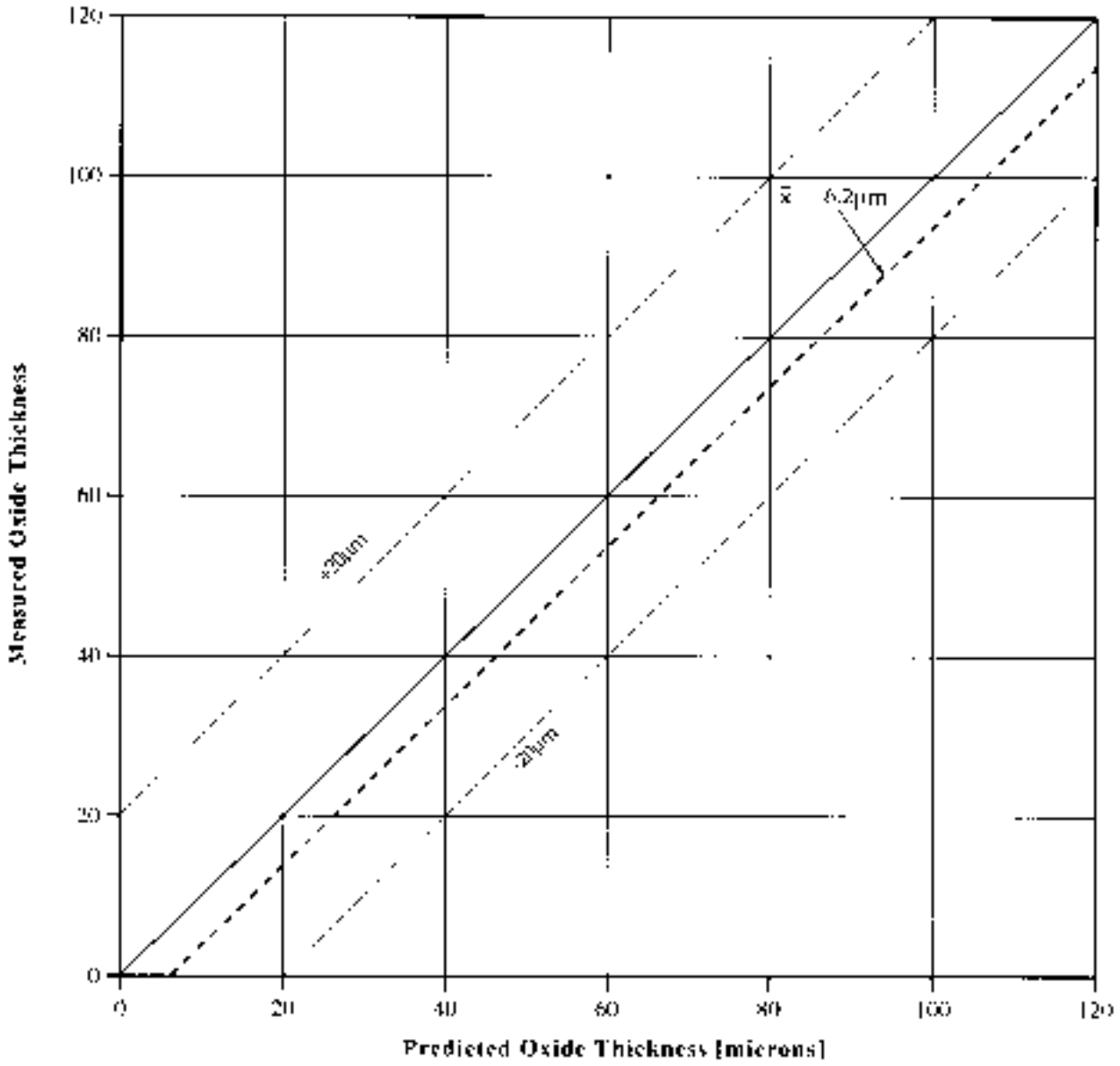

Figure 3-12 Non-Zn F1C13 3 cycle rod oxide thickness at span 6

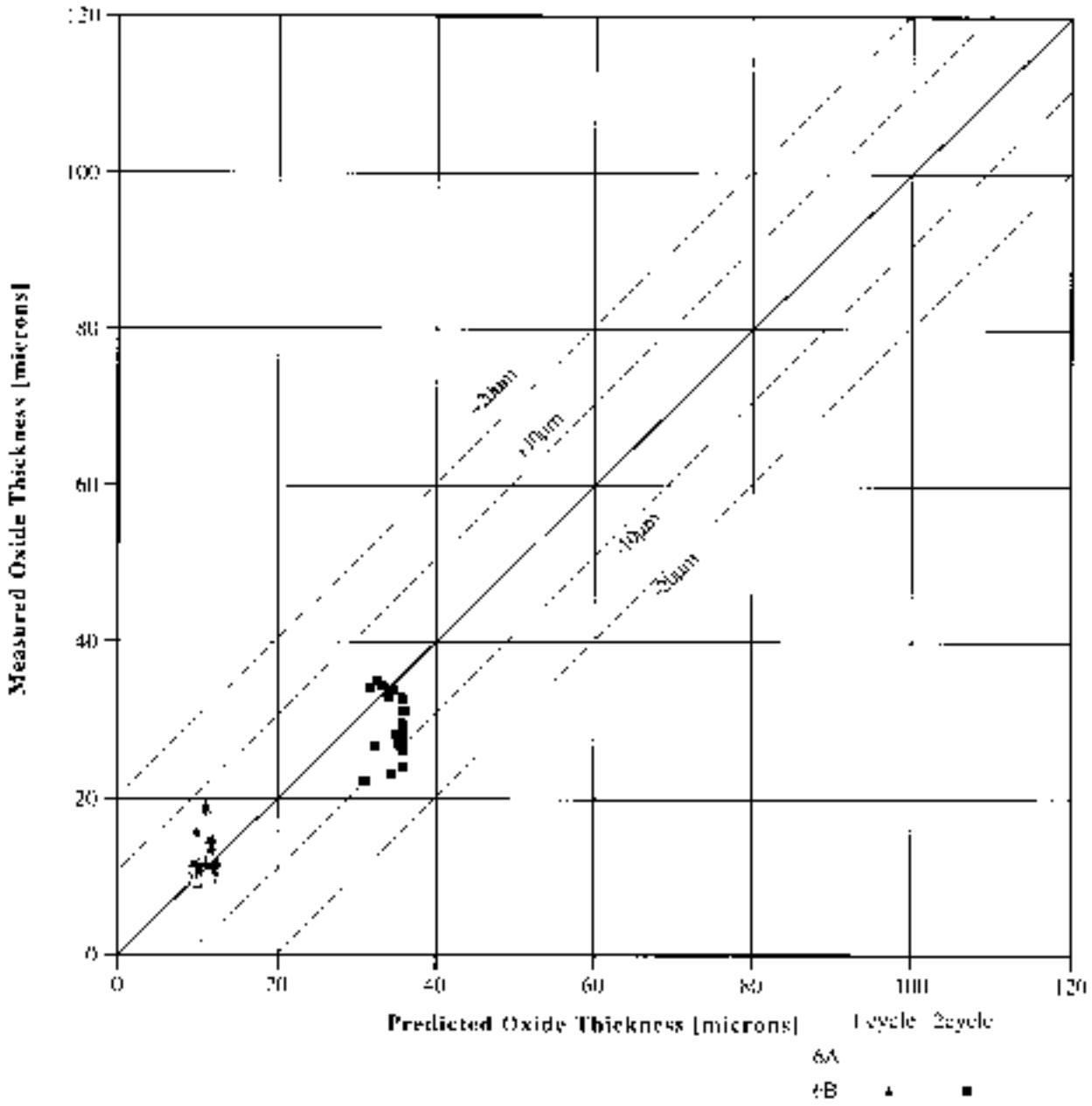

Figure 3-13 Non-Zn F2C9 oxide thickness at span 6

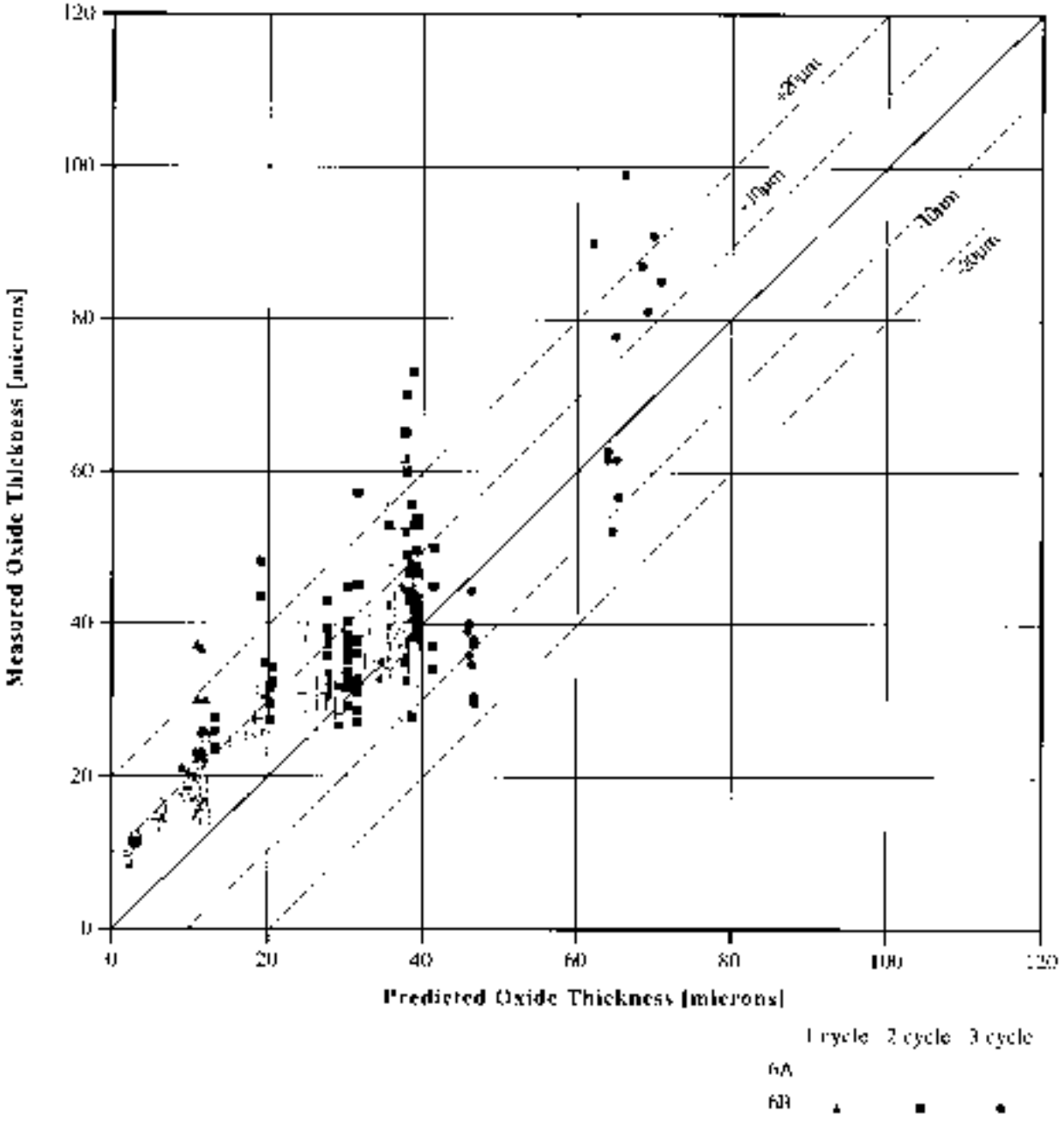

Figure 3-14 Post-Zn F2C10 oxide thickness at span 6

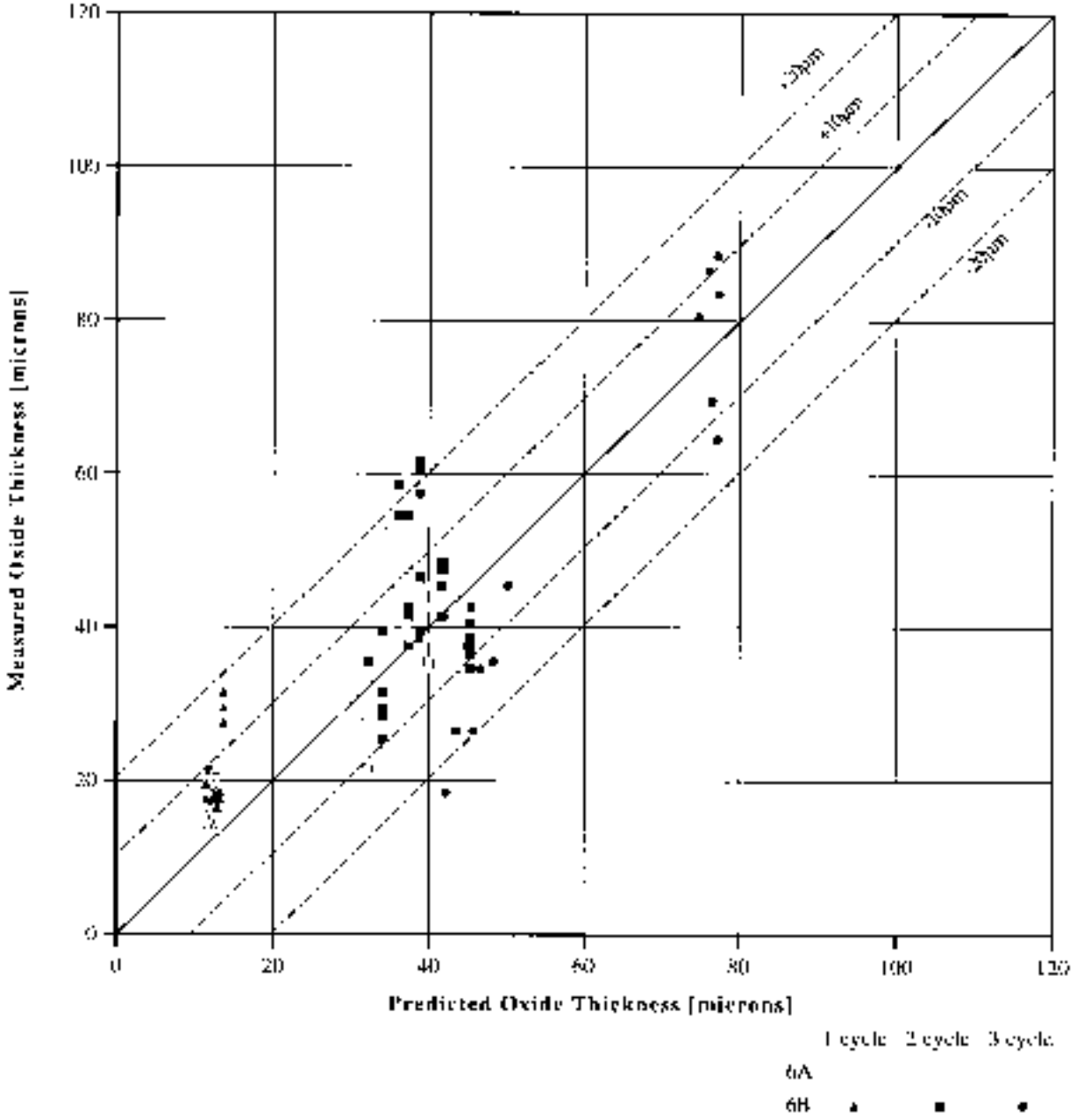

Figure 3-15 Non-Zn F1C13 oxide thickness at span 6

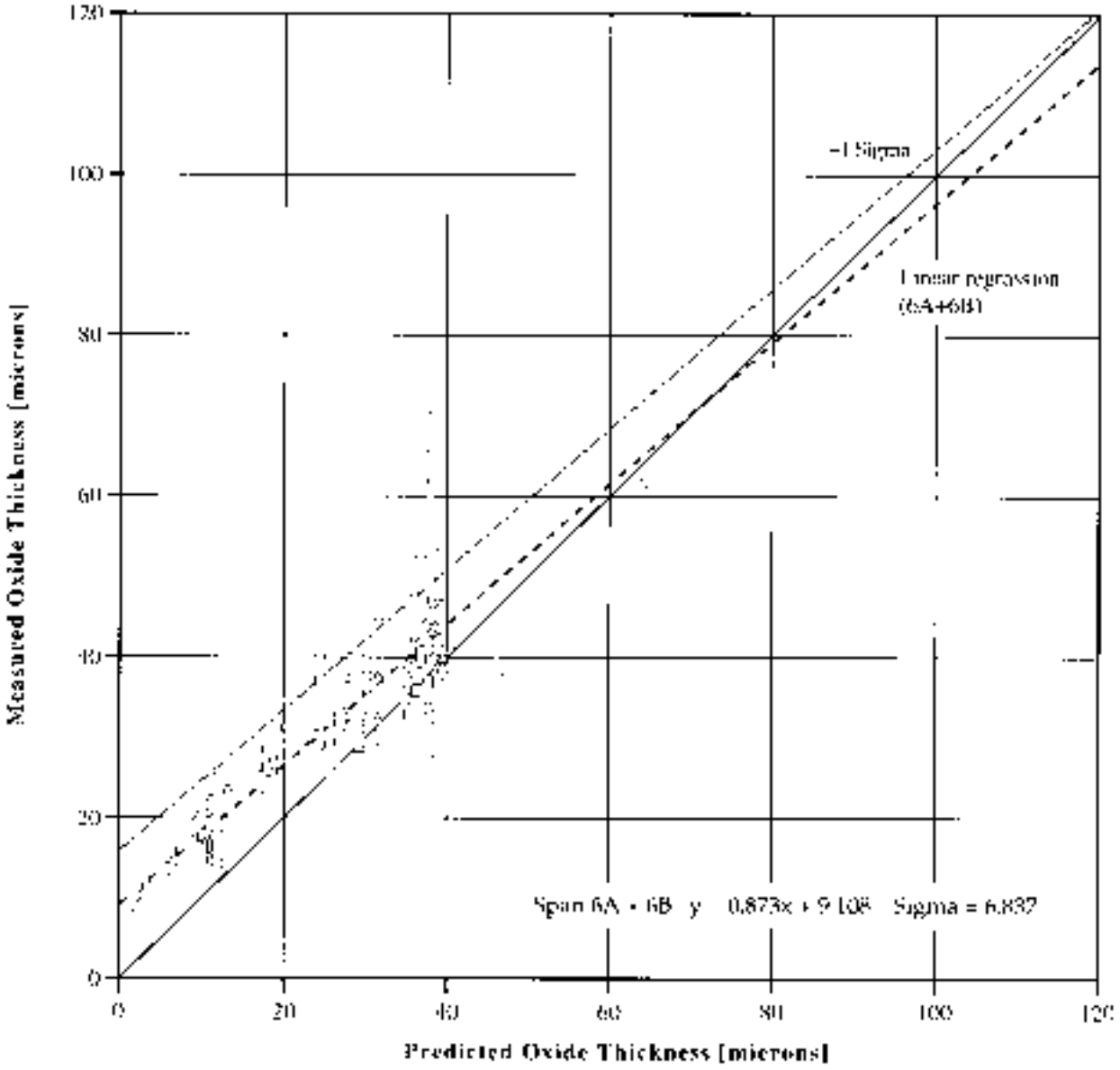

Figure 3-16 Post-Zn F2C10 oxide thickness at span 6

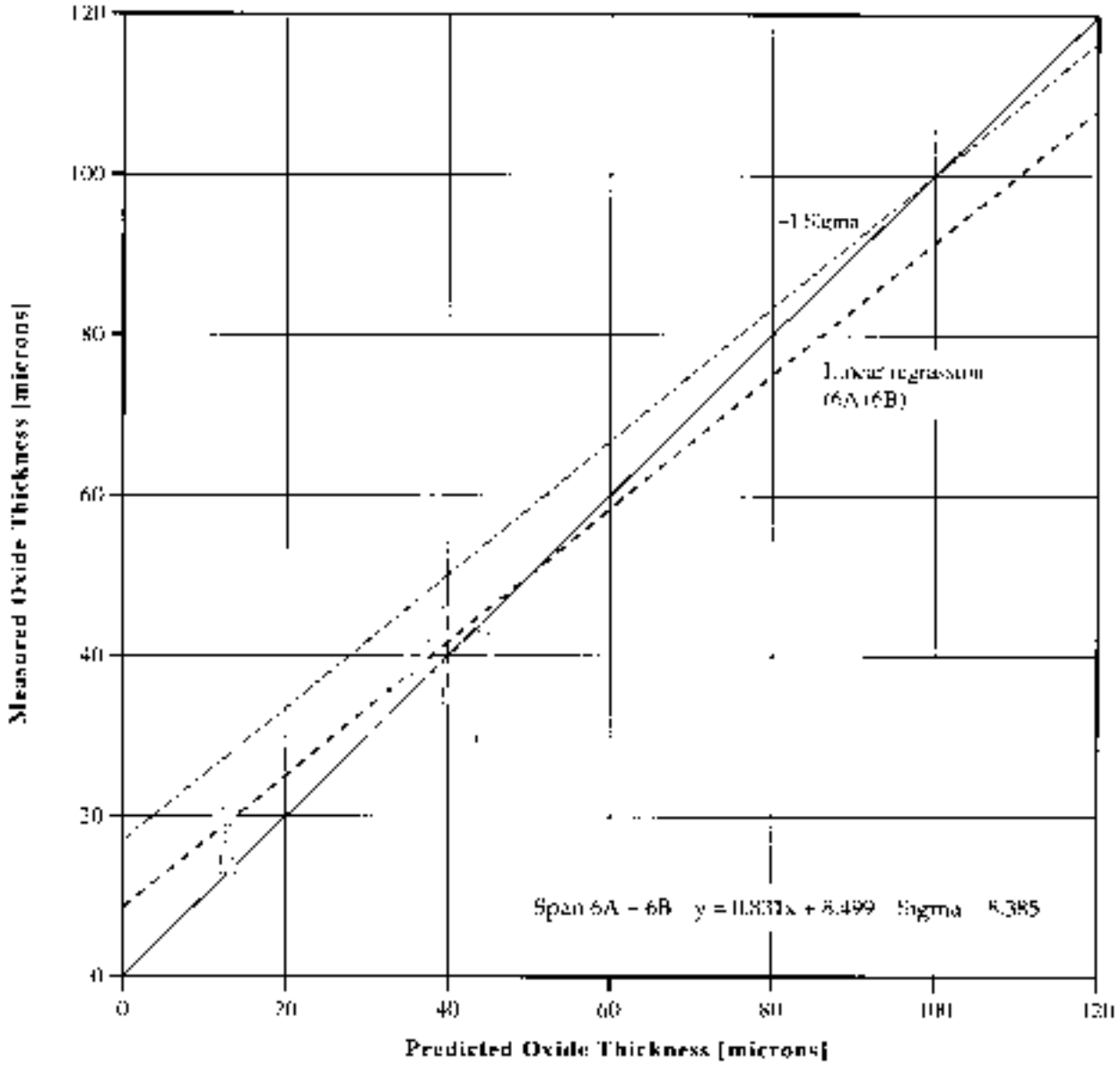

Figure 3-17 Non-Zn F1C13 oxide thickness at span 6

oxide (higher burnup) regime. Calculations using the regression equations in the figures indicate that the under-predictions are 7 and 5 μm at 20 μm, and 4 and 2 μm at 40 μm for F2C10 and F1C13 data, respectively. The over-predictions are 4 and 8 μm at 100 μm for F2C10 and F1C13, respectively.

The F2C9 composite data are not statistically compared as the data base of Improved low tin Zircaloy rods is too small.

3.4 COMPARISON OF CYCLE-TO CYCLE DATA

Another way to evaluate the statistical meaning of the data is to compare the average shift, $\bar{x}$, and standard deviation, σ, of the measured data against PFCC prediction separately for once, twice, and thrice burnt rods. The values are shown in Table 3-1. As mentioned earlier, these values are calculated using the expressions discussed in Appendix C.

Table 3-1 Average shift, $\bar{x}$, from PFCC prediction, and standard deviation, for the once, twice, and thrice burnt rods in F2C9, F2C10, and F1C13 data.

	$\bar{x}$, μm	σ,μm	$\bar{x}+1\sigma$, μm
F2C9			
Once burnt	1.1	2.9	4.0
Twice burnt	-5.1	4.4	-0.7
F2C10			
Once burnt	7.8	3.7	11.5
Twice burnt	5.5	7.1	12.6
Thrice burnt	0.3	13.5	13.8
F1C13			
Once burnt	6.7	4.8	13.5
Twice burnt	2.6	9.7	12.3
Thrice burnt	-6.2	12.1	5.9

The oxide data and the statistical values are also shown in Figures 3-18, 3-19, and 3-20 for the once, twice, and thrice burnt rods, respectively. For the once burnt rods, it can be seen that the F2C10 and F1C13 data are statistically nearly the same, and both are about 5 μm higher than the F2C9 data. The two highest data points in F2C10 are from assembly 2M19 and the possibility of measurement bias was discussed earlier. The two cycle rods, Figure 3-19, in F2C10 and F1C13 data are again statistically similar, and both are 7-10 μm higher than the F2C9 data. The few highest data points representing 5 rods in the F2C10 data came randomly from four assemblies. The thrice burnt rods, Figure 3-20, show a difference of about 6-7 μm between the F2C10 and F1C13 rods. However, the data bases of the thrice burnt rods are relatively small.

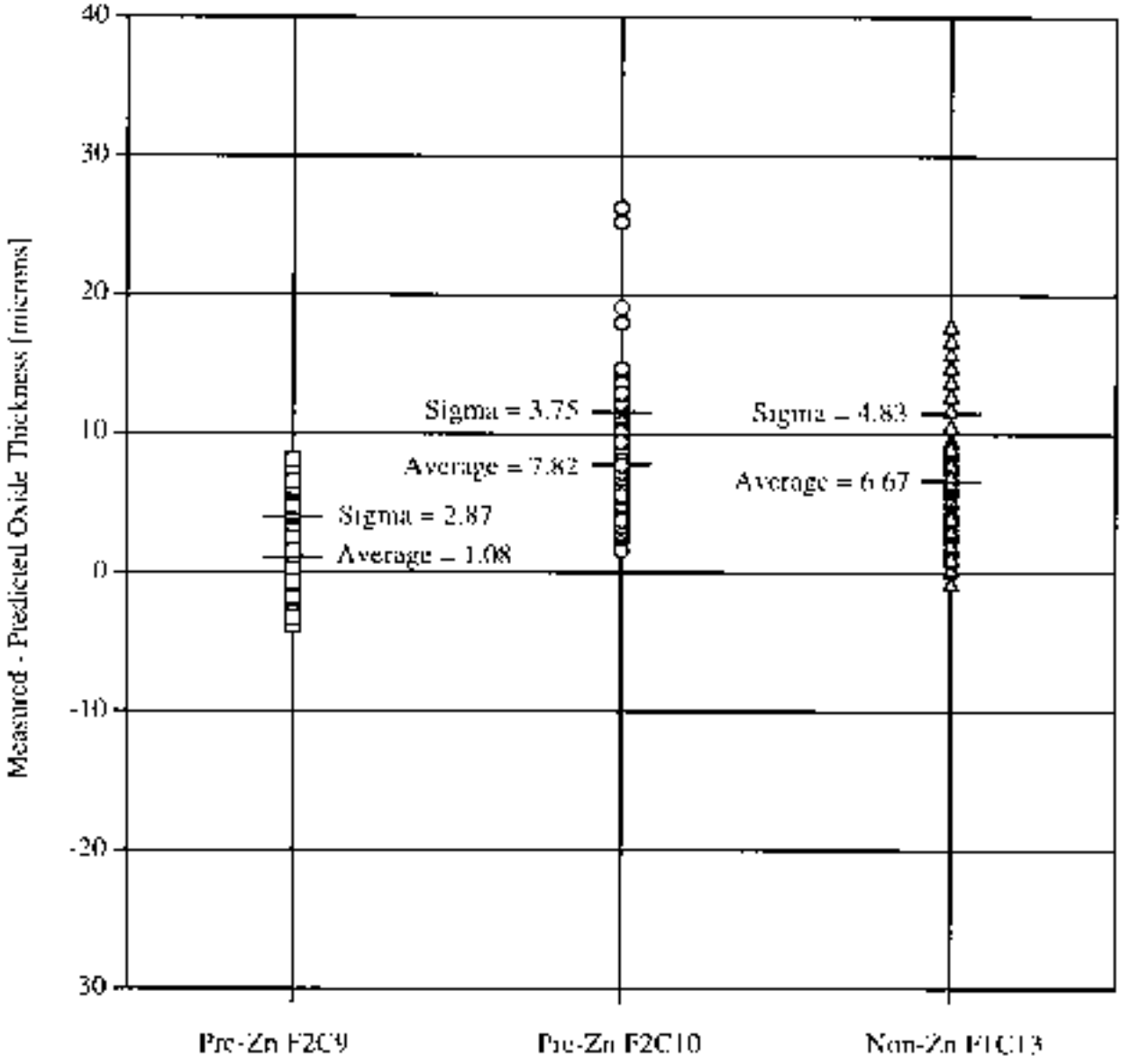

Figure 3-18 (Measured - Predicted) oxide thickness span 6 after one cycle of irradiation

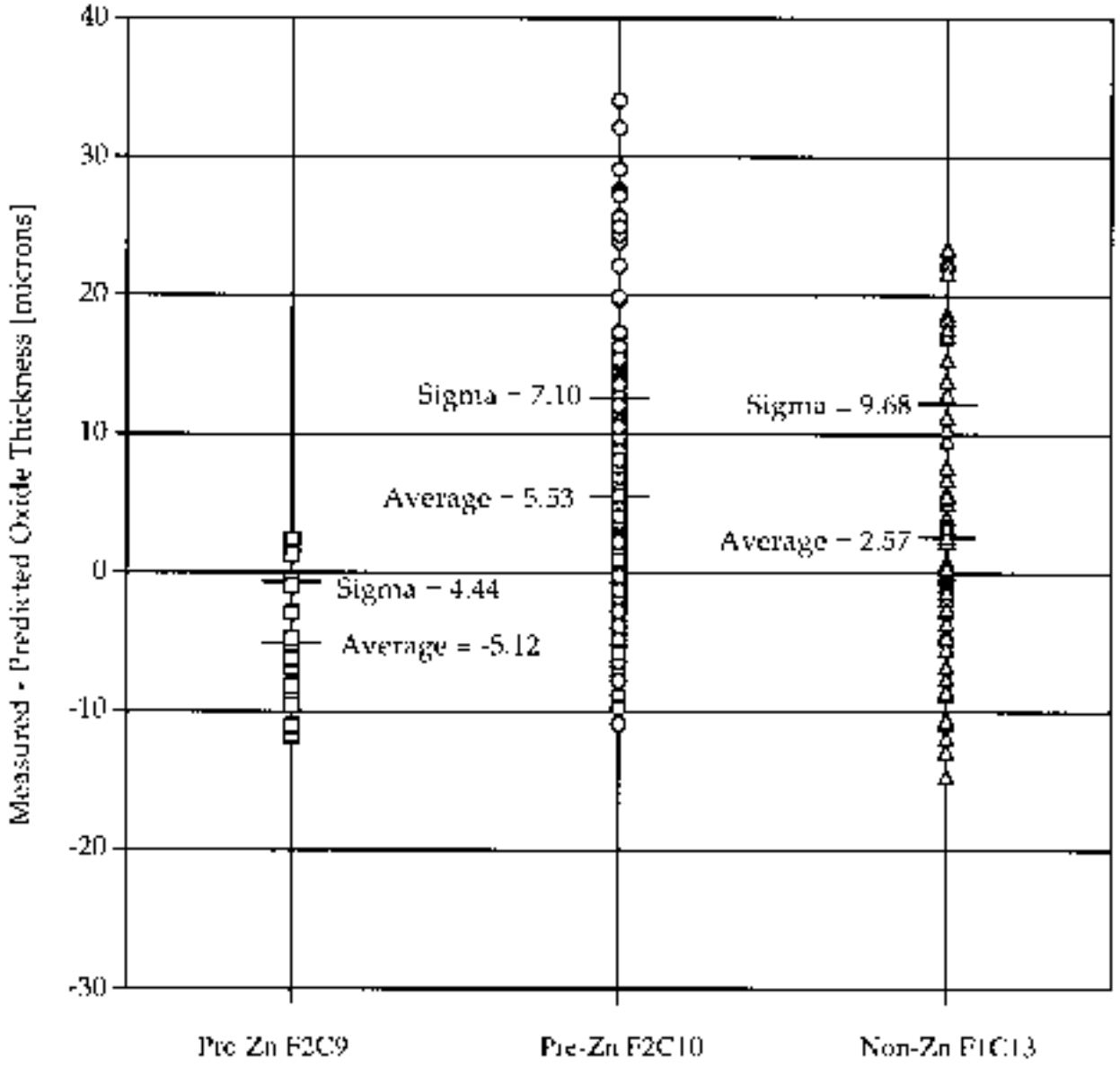

Figure 3-19 (Measured - Predicted) oxide thickness span 6 after two cycles of irradiation

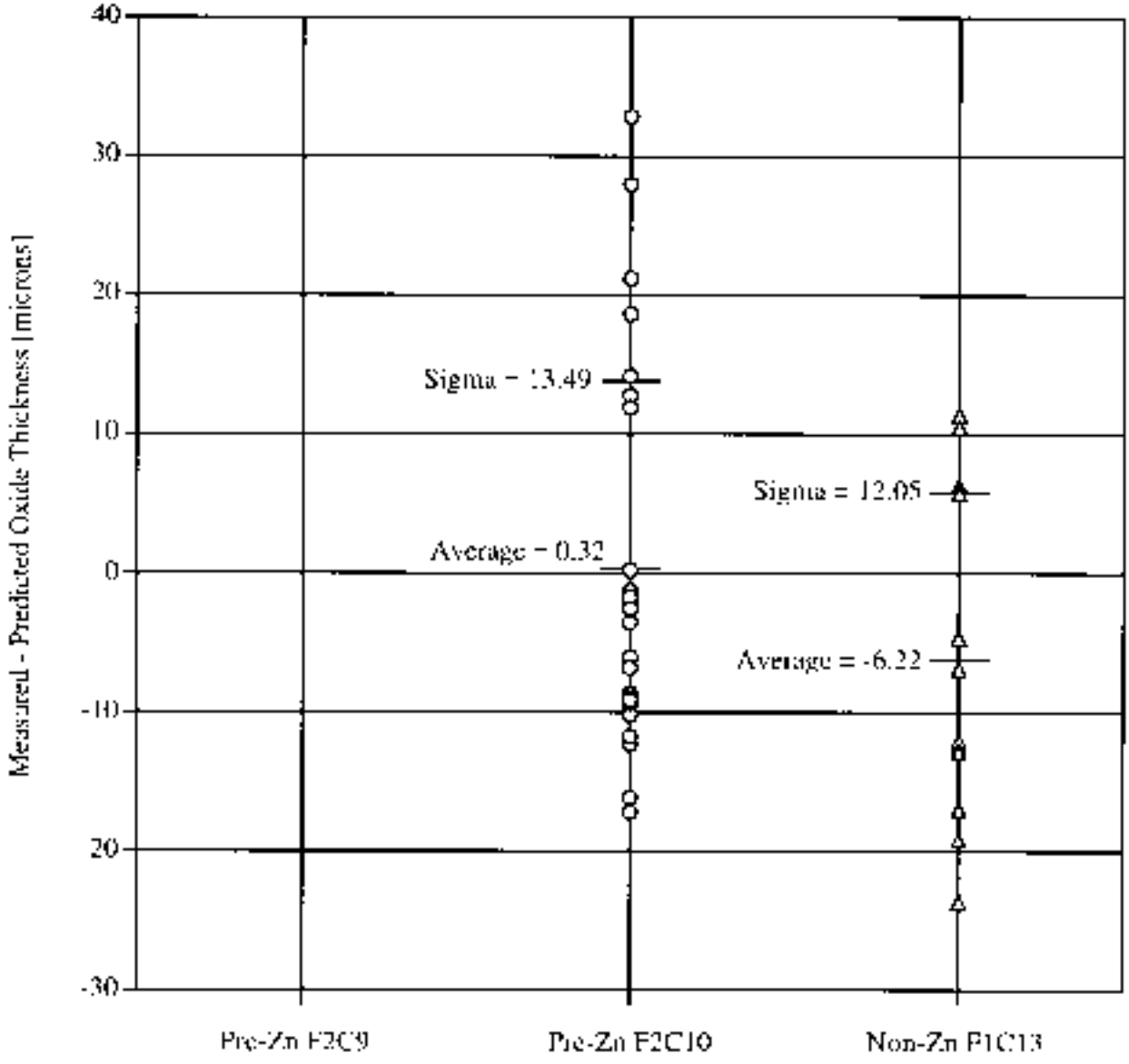

Figure 3-20 (Measured - Predicted) oxide thickness span 6 after three cycles of irradiation

4

DISCUSSION AND CONCLUSIONS

4.1 OXIDE DATA COMPARISON

The data analyses presented in Sections 2 and 3 indicate that the rod oxide thickness data obtained at Farley-2 EOC10 after the zinc injection are generally higher than the data obtained at EOC9 prior to the zinc injection. The increases in the oxide thickness were accompanied by not only the zinc injection, but also increases in the thermal/hydraulic duty. The difference in the T/H duty is believed to be a major contributor to the increased cladding corrosion in the F2Cl0 data, as discussed in Section 4.3 below.

When the post-Zn EOC10 data were compared with the Farley-1 EOC13 data of comparable design, the differences in the oxide thickness are small. After taking into account a potential measurement interference of one once burnt assembly (2Ml9) in the EOC10 data, the once burnt assemblies in the F2Cl0 and FlCl3 data had about the same corrosion behavior as based on both oxide data comparisons in Section 2 and the PFCC analysis with statistical comparisons in Section 3. This is important evidence suggesting that the zinc injection did not contribute to increased cladding corrosion of the Farley-2 EOC10 rods, as the first cycle rods had the highest thermal duty and are expected to be more susceptible to a crud-induced corrosion enhancement.

The twice burnt rods in the F2C10 and F1C13 data also showed similar behavior, as based on the PFCC analysis and statistical comparisons of the PFCC results. However, buried in the statistics are four (out of the 134) F2C10 rods having a peak oxide exceeding the highest peak oxide of 62 μm in the F1C13 data. Those four higher corrosion rods had peak oxide up to 73 μm, with one rod showing mild oxide spallation. The relatively higher corrosion of those few rods may not be related to the zinc injection, based on the following three reasons. First, many plants have also reported cladding oxide thickness values in the 60-75 μm range at about the same burnup of low 40 GWd/MT[8,9]. (Most of those data came from Standard 1.5-1.6 wt.% Sn cladding, whereas the F2C10 twice burnt rods had Improved 1.3-1.4 wt.% Sn cladding.) For example, some Millstone-3 rods were measured at ~70-75 μm and showed oxide spalling at EOC3[9]. Second, those four rods came randomly from three different assemblies, where adjacent rods had the same duty and behaved normally. Third, both

F2C10 and F1C13 had the same ~3% of the measured rods with the relatively high oxide thickness of ≥60 μm.

Overall, the post-Zn F2C10 and the non-Zn F1C13 rods had higher corrosion than the pre-Zn F2C9 rods. The increased corrosion is attributable to increases in the T/H duty, as discussed later. The post-Zn F2C10 cladding corrosion was only marginally higher than the F1C13 rods, but based on the PFCC model no statistical differences between the two data sets can be discerned. The upper range of the oxide thickness of the F2C10 and F1C13 rods, being 20-30, 60-73, and 80-100 μm for the once, twice, and thrice burnt rods, respectively, have also been reported sporadically by plants without zinc injection. On this basis, it is not likely that the zinc injection contributed to a significant effect on the fuel rod corrosion at Farley-2 EOC10. The only corrosion observation of significant engineering importance is the 6 twice burnt rods with peak oxide thickness >60 μm. Likely explanations for those higher corrosion rods are: (1) random cladding material variability, and (2) random crud deposition due to local rod power variations.

4.2 CLADDING MATERIAL VARIABILITY

Cladding material variability due to subtle differences in alloy chemical composition and cladding thermo-mechanical processing or surface finish can result in rod-to-rod corrosion variability. The high corrosion Millstone-3 rods mentioned above came from the initial core fuel and are believed to have resulted from a corrosion susceptible cladding lot[9]. However, cladding material quality has been steadily improved through tighter alloy chemistry and notably thermo-mechanical process controls since the mid-1980s, as the whole industry has gained better knowledge in Zircaloy in-reactor corrosion mechanisms. This is particularly true after the introduction of low tin cladding. A review of the manufacturing records by Westinghouse and Southern Nuclear staff found that the tin content in the cladding lots used in the F2C10 Improved Zircaloy rods were within the specified range of 1.3-1.4 wt.%, and the cumulative annealing parameter was near the desired value of ~10^{-17} h. From the rod-to-rod corrosion assessment presented in Section 2, it was also found that material variability was not an issue for the majority of the cladding in the F2C9, F2C10 and F1C13 rods. However, the random occurrence of those few high corrosion rods in the twice burnt F2C10 could fit the pattern of a material variability effect. Until samples of the high corrosion cladding or its archive can be made available for a detailed laboratory testing and analysis, this material variability issue cannot be unequivocally resolved.

4.3 ROD THERMAL/HYDRAULIC DUTY AND SUBCOOLED BOILING

Fuel rod thermal duty or heat flux, as partially indicated by the radial peaking factor, affects the rod wall temperature and thus could have a significant effect on the cladding corrosion rate. As shown in Figures 2-11 to 2-15, the rod peak oxide thickness in general increases with increasing rod thermal duty.

Using the radial peaking factor as a guide, the once burnt rods that were measured in this program had a range of 1.22-1.37, 0.65-1.45, and 1.31-1.47 for the F2C9, F2C10, and F1C13, respectively. The twice burnt rods had a range of 0.70-1.34, 0.60-1.39, and 1.31-1.47 during their first cycle operations, respectively. For Farley-2, the subcooled boiling has been estimated to take place at a radial peaking factor of ~1.37-1.38. Thus, none of the F2C9 rods are expected to have noticeable subcooled boiling. Many of the once and twice burnt rods in the F2C10 and F1C13 data are estimated to have subcooled boiling. The peak F1C13 rods had higher T/H duty than that of the F2C10 rods. This explains why thicker and textured deposits were found on the hotter spans of the once burnt F1C13 rods.

The T/H duty of a rod is influenced by the peaking factor of the rod and its neighboring rods. A simplified (SCM model) approach is to consider the enthalpy inputs of the 8 nearest adjacent rods surrounding the water channel of the subject rod, as discussed in Appendix A. A parameter that can represent the thermal duty of a rod is the effective power peaking factor, RPF_{eff}, which is defined as RPF_{eff} = RPF (DE/DH), where RPF is the rod peaking factor, DE the hydraulic diameter, and DH the heated diameter of the subject rod. Calculations for DE and DH are shown in Equations A5 and A7 in Appendix A, respectively. DE is the value accounting for the assembly geometry. DH accounts for the rod power distribution of the subject and the 8 nearest neighboring rods. The DH value decreases as the rod power peaking factor of neighboring rods increases, thus, producing a larger RPF_{eff} value.

Using the RPF_{eff} approach, the role of higher T/H duty in causing higher corrosion of the F2C10 and F1C13 rods is illustrated in Figure 4-1. The figure shows deviation of the measured oxide data from the PFCC calculated values as a function of the RPF_{eff} for the once burnt rods (excluding 2M19 rods) in the F2C10 and F1C13 data base. It can be seen that the measured values were on the average 5 μm higher than the predicted values for a RPF_{eff} <~1.37-1.39, but increased significantly for rods with RPF_{eff} > ~1.38 and reached an average value of 15 μm at a RPF_{eff} of 1.44. Thus, the higher than expected oxide thickness of the high power rods in the F2C10 and F1C13 data can be attributed to the boiling duty of these rods.

In summary, the correlation shown in Figure 4-1 illustrates that higher T/H duty of the F2C10 and F1C13 once and twice burnt rods contributed to the higher than expected oxide thickness values. The boiling duty of a high power rod is intensified when it is placed next to another high power assembly, resulting in simultaneous subcooled boiling of adjacent rods. It is not clear how this would result in an increased corrosion rate since the wall temperature is not largely impacted. One postulated explanation is that significant subcooled boiling lead to local radiolytic production of oxidizing species, which can increase the corrosion rate of Zircaloy. Another possibility is formation of crud deposits during operation to cause a thermal impedance effect or hideout of lithium inside the crud deposit. Neither of the explanations can be substantiated without supporting test data.

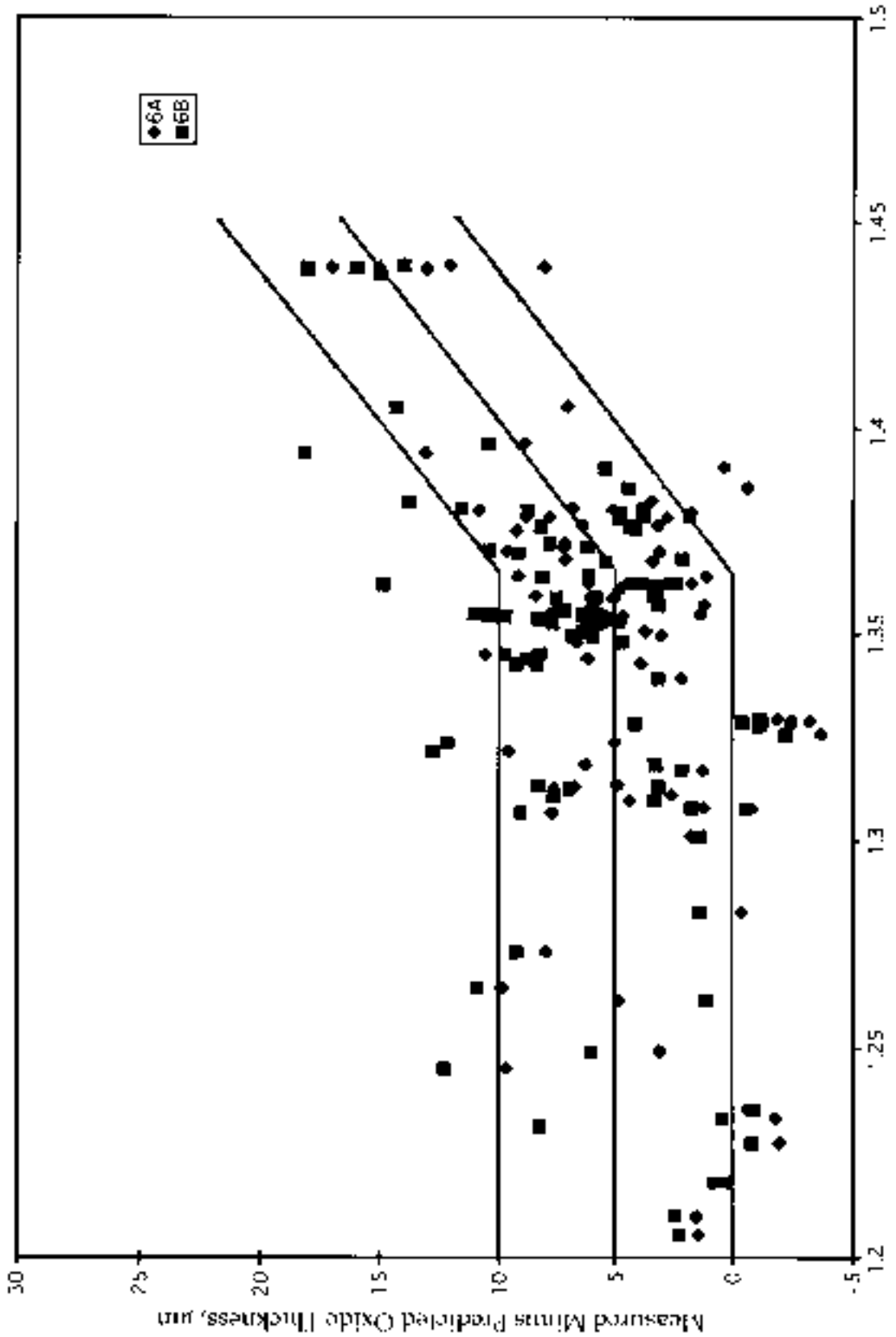

Figure 4-1 One Cycle Oxide Thickness Data in the P2C9, P2C10, and P1C13 Data Base (except assembly 2M19)

4.4 ZINC AND RCS CHEMISTRY EFFECTS

The difficulty encountered in assessing the effect of zinc injection in Cycle 10 on fuel rod corrosion at Farley-2 resulted mainly from a simultaneous increase in the T/H duty from Cycle 9 to Cycle 10. Analyses of the available data base suggest that the major contributor to the increased corrosion of the F2C10 rods was the increased T/H duty, rather than zinc injection. However, the boiling duty of the Farley-2 Cycle 10 rods is only relatively mild when compared to some high temperature plants.[10] It is not clear whether deposition of zinc might eventually occur if the degree of boiling exceeds the Farley-2 experience.

Zinc may deposit on fuel rods as zinc borate or zinc ferrite. Deposition of zinc borate may cause localized flux suppression. Zinc ferrite has been commonly observed in fuel rod deposits in BWRs where zinc at a concentration of 5 to 10 ppb is maintained in the reactor water. Zinc concentrations of up to ~20% of the total metallic deposits have been reported on fuel rod surfaces. Its presence in the crud deposits increases the tenacity of the iron oxide crud to the rod surfaces, but not the total loading of the crud. As high as 2000 to 4000 mg/dm^2 of metallic deposits in oxide forms have been reported at the peak loading location of rods with a burnup of 40 GWd/MT[6], but no evidence of crud-induced cladding corrosion acceleration has been reported to-date. This may be due to the 40-50°C lower rod wall temperature in BWRs than that in PWRs.

Based on the BWR experience, an interaction of zinc with nickel ferrite deposits may take place if the RCS coolant concentration of the corrosion products is high and subcooled boiling is significantly increased from the Farley-2 experience base. At present, there is not sufficient solubility data in existence to allow quantification of the conditions that will lead to such an interaction. In summary, while the Farley-2 experience indicated no significant effect of zinc injection on cladding corrosion, the same cannot be said for certainty if the fuel duty is increased. A fuel T/H duty analysis and coolant chemistry review should be performed and, if the conditions exceed the Farley-2 experience, a fuel surveillance program should be implemented to ascertain fuel reliability.

5

REFERENCES

1. "Evaluation of Zinc Addition on Fuel Cladding Corrosion at the Halden Test Reactor," EPRI TR-106357, August 1996

2. "Evaluation of Zinc Addition to the Primary Coolant of PWRs," EPRI TR-106358 V1, October 1996

3. B. Cheng, P. M. Gilmore, and H. H. Klepfer, "PWR Zircaloy Fuel Cladding Corrosion Performance, Mechanisms and Modeling," presented at ASTM 11th International Symposium on Zirconium in the Nuclear Industry, Garmisch, Germany, September 1995, (to be published by ASTM)

4. "EPRI PWR Fuel Cladding Corrosion (PFCC) Model," EPRI TR-105387, December 1995

5. "Evaluation of Fuel Rod Leakage Mechanisms - Summary Report," EPRI TR-104721, December 1994

6. H. A. Levin, S. E. Garcia, "BWR Fuel Experience with Zinc Injection," NACE 7th International Symposium on Environmental Degradation of Materials in Nuclear Power Systems - Water Reactors, Breckenridge, Colorado, August 1995, NACE, Houston

7. J. H. Davies, E. V. Hoshi, R. D. Reager, R. W. Warner, and S. K. Yagnik, "Hot Cell Characterization of Zinc Rich Crud Layers," presented at Halden Enlarged Program Meeting, Loen, Norway, May 1996

8. Proceedings, EPRI - Utility Workshop on PWR Fuel Corrosion, Washington, D.C., July l993, ed. B Cheng

9. "Evaluation of the Impact of Elevated Lithium Concentrations on Zircaloy-4 Fuel Clad Oxidation in the Millstone-3 PWR," EPRI TR-105662, December 1995

10 Primary Water Chemistry, Fuel Rod Corrosion and Crud Deposition in PWRs", EPRI TR-107255, December 1996

Appendix A

PFCC INPUT DATA AND CALCULATIONS

A.1 PFCC INPUT VALUES

The Farley data provided by EPRI was in Westinghouse RENAC format. This data was converted into PFCC input format. Table A1 contains a summary of the PFCC input values. Farley core average heat flux was 5.29 kw/ft.

Table A1 Farley PFCC Inputs

	Farley 1			Farley 2		
	Cycle 11	**Cycle 12**	**Cycle 13**	**Cycle 8**	**Cycle 9**	**Cycle 10**
UNI Data Block - Input Units Control						
Input Units	British	British	British	British	British	British
Time Units	Hours	Hours	Hours	Hours	Hours	Hours
SYS Data Block - Reactor System Parameters						
System Pressure	2250	2250	2250	2250	2250	2250
Inlet Coolant Mass Flux	2.44E+06	2.44E+06	2.44E+06	2.48E+06	2.32E+06	2.28E+06
Inlet Coolant Temperature	542.7	542.7	542.7	542.4	543.9	542.1
FUE Data Block - Fuel Rod Modeling Parameters[a]						
Pellet Outside Diameter	.3225	.3088	.3088	.3225	.3088	.3088
Rod Outside Diameter	.3740	.3600	.3600	.3740	.3600	.3600
Cladding Thickness	.0225	.0225	.0225	.0225	.0225	.0225
Length of Fuel Column	144	144	144	144	144	144
% Theoretical Fuel Density	95.78	96.03	96.12	95.6404	95.509	95.4097
FA-to-FA gap (DA	0.158	0.186	0.186	0.158	0.186	0.186
Equivalent Hydraulic Dia.[b]	.4922	.5399	.5399	.4922	.5399	.5399
Effective Heated Diameter	See Section 2.1.2 for calculation					
HEA Data Block - Heat Transfer Coefficient						

Table A1 Farley PFCC Inputs (continued)

All Default Values are Used						
***OXI Data Block Oxidation Model Parameters**						
Oxidation Model	EPRI/SLI	EPRI/SLI	EPRI/SLI	EPRI/SLI	EPRI/SLI	EPRI/SLI
Size of s-k_{ox} Table	1	1	1	1	1	1
Oxide Thermal Conduct.	0.015	0.015	0.015	0.015	0.015	0.015
C1 Coefficient	5.8876E+10	5.8876E+10	5.8876E+10	5.8876E+10	5.8876E+10	5.8876E+10
Q1 Coefficient	33662.7	33662.7	33662.7	33662.7	33662.7	33662.7
D3 Multiplier	2.0	2.0	2.0	2.0	2.0	2.0
C0 Multiplier	8.198E+06	8.198E+06	8.198E+06	8.198E+06	8.198E+06	8.198E+06
Q2 Exponent	24825.0	24825.0	24825.0	24825.0	24825.0	24825.0
Q2U Exponent	9135.6	9135.6	9135.6	9135.6	9135.6	9135.6
CLI Lithium Multiplier	0.65	0.65	0.65	0.65	0.65	0.65
CFE Multiplier	2.0E-02	2.0E-02	2.0E-02	2.0E-02	2.0E-02	2.0E-02
	Farley 1			**Farley 2**		
	Cycle 11	**Cycle 12**	**Cycle 13**	**Cycle 8**	**Cycle 9**	**Cycle 10**
CPHI Multiplier	1.2E-04	1.2E-04	1.2E-04	1.2E-04	1.2E-04	1.2E-04
P0 Power Coefficient	0.24	0.24	0.24	0.24	0.24	0.24
Cladding Tin Content	1.38	1.38	1.38	1.38	1.38	1.38
Particle Size Dist. SA	8E-18	8E-18	8E-18	8E-18	8E-18	8E-18
***LIT Data Block Lithium Chemistry Information**						
See Section 2.1.4 for Lithium Concentration Curves						
***SPA Data Block - Spacer Grid Modeling Parameters**[c]						
Number of Spacer Grids	7[d]	10[e]	10	7	10	10
Spacer Grid Height	0	0	0	0	0	0
Spacer Grid Effects Mult.	1.0	1.0	1.0	1.0	1.0	1.0
***AXI Data Block - Power and Flux Shape Profiles**						
See Section 2.1.5 for Axial Power and Flux Profiles						
***POW Data Block Power Time History Information**						
Average Power[f] [kw/ft]	5.2	5.2	5.2	5.2	5.2	5.2
See Section 2.1.3 for Additional Power History Inputs						

a. The Fuel Modeling Parameters, with the exception of the Effective Heated Diameter, re,ain constant for a fuel rod. A rod inserted in Cycle 8 will have the same Fuel Modeling Parameters for all subsequent cycles (Effective Heated Diameter excluded).

b. See Section 2.1.1 for a description of how the Equivalent Hydraulic Diameter is calculated.

c. The Spacer Grid Modeling Parameters remain constant for a fuel rod. A rod inserted in Cycle 8 will have the same Spacer Grid Modeling Parameters for all subsequent cycles.

d. Rods with 7 spacer grids do not have Intermediate flow mixers. The axial locations of the 7 spacers are: 1.796, 26.317, 46.867, 67.417, 87.967, 108.517, and 129.067.

e. Rods with 10 spacer grids have Intermediate Flow Mixers modeled as spacers. The axial locations of the 7 spacers and the 3 IFMs are: 1.796, 26.317, 46.867, 67.417, 77.694, 87.967, 98.244, 108.517, 118.794, and 129.067.

f. The values presented here are for the 100% power case. The Farley-1 PFCC analysis was performed assuming the plant was operating at this full power for Cycles 11, 12, and 13. Please see Section 2.1.3 for the time dependent plot used for Farley-2 PFCC input.

A.2 EQUIVALENT HYDRAULIC DIAMETER

The equivalent hydraulic diameter is calculated for each fuel rod analyzed in the Farley analysis. Since the hydraulic diameter is a function of only geometry, it remains constant for every cycle that the fuel rod is in the core. The values of the hydraulic diameter used in the Farley analysis can be found in Table A1.

The equivalent hydraulic diameter is defined as:

$$DE = 4\frac{\text{Cros section available for flow}}{\text{Wetted perimeter}} = 4\frac{A}{P} \qquad \text{Eq. (A1)}$$

The geometry around a rod on the face of a assembly is presented in Figure A1. We choose the control area to be centered on the rod of interest and is comprised of 9 rods (1 full rod at the center and 4 quarter rod at the corners and 4 half rods on the side). The area available to the flow is represented by the shaded area which is equal to the control area (the dashed rectangle) minus the area occupied by the rods in the control area.

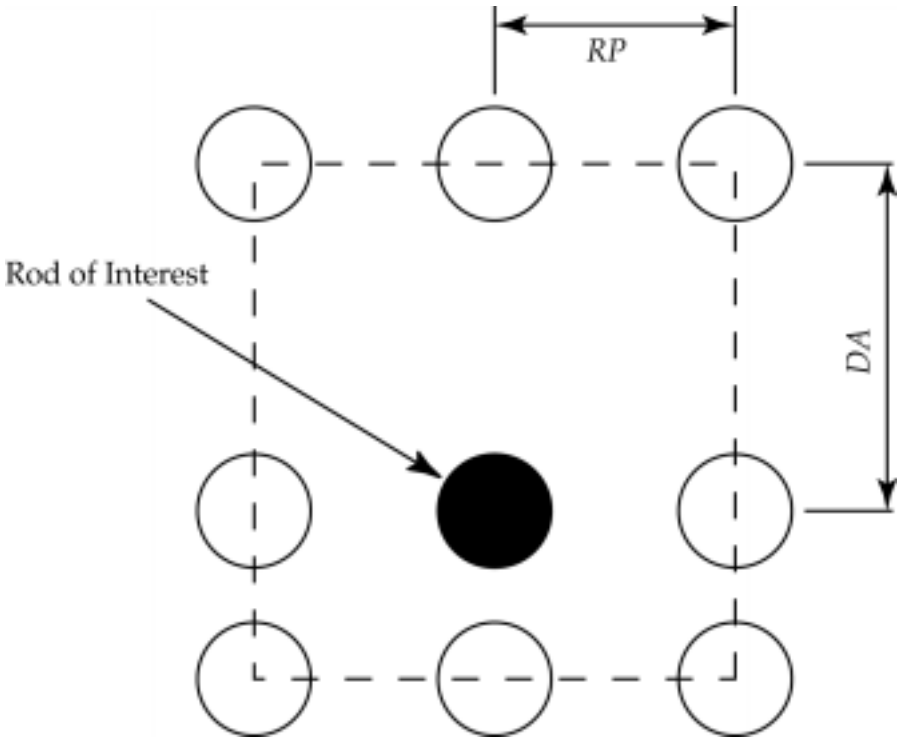

Figure A1 Sample Fuel Rod Geometry for Equivalent Hydraulic Diameter Calculation

The area occupied by the rods in the control area is:

$$A_{rods} = \left[1\ (\ 1\ \text{Rod}\ ) + 4\left(\frac{1}{4}\ \text{Rods}\right) + 4\left(\frac{1}{2}\ \text{Rods}\right)\right] \cdot \frac{\pi d^2}{4} = \pi d^2 \qquad \text{Eq. (A2)}$$

which leads to the area available for flow:

$$A = A_{control} - A_{rods} = (RP + RP)(RP + DA) - \pi d^2 \qquad \text{Eq. (A3)}$$

where:

RP = Rod Pitch

DA = Inter Assembly Distance, and

d = Rod Diameter.

The Wetted Perimeter is simply:

$$P = 4\pi d \qquad \text{Eq. (A4)}$$

Substituting Equations (A3) and (A4) into Equation (A1), the expression for the Equivalent Hydraulic Diameter is obtained:

$$DE = 4\frac{A}{P} = \frac{(RP + RP)(RP + DA) - \pi d^2}{\pi d} \qquad \text{Eq. (A5)}$$

A.3 EFFECTIVE HEATED DIAMETER

The effective heated diameter is calculated for each fuel rod analyzed in the Farley analysis. The heated diameter varies from cycle to cycle for a fuel rod since it is a function of geometry and power distribution. The values of the effective heated diameters used in the Farley analysis can be found in the Tables located in Section A.4.

The effective heated diameter can be calculated for Rod R1 in Figure A2 as:

$$DH_1 = R_1 \frac{\sum_{i=1}^{4} DE_1 \sum_{j=1}^{9} f(i,j)}{\sum_{i=1}^{4}\sum_{j=1}^{9} R_j f(i,j)} \qquad \text{Eq. (A6)}$$

where:

DH_k = effective heated diameter for rod k,

R_j = rod radial power factor for rod j,

DE_i = equivalent hydraulic diameter of subchannel i, and

f(i,j) = fraction of rod j that is in contact with subchannel i.

Substituting the appropriate values for f(i,j) into Equation (A6), one obtains our expression for the effective heated diameter:

$$DH_1 = R_1 \frac{\sum_{i=1}^{4} DE_i}{R_1 + \frac{1}{2}\left[R_2 + R_3 + R_5 + R_8\right] + \frac{1}{4}\left[R_4 + R_6 + R_7 + R_9\right]} \qquad \text{Eq. (A7)}$$

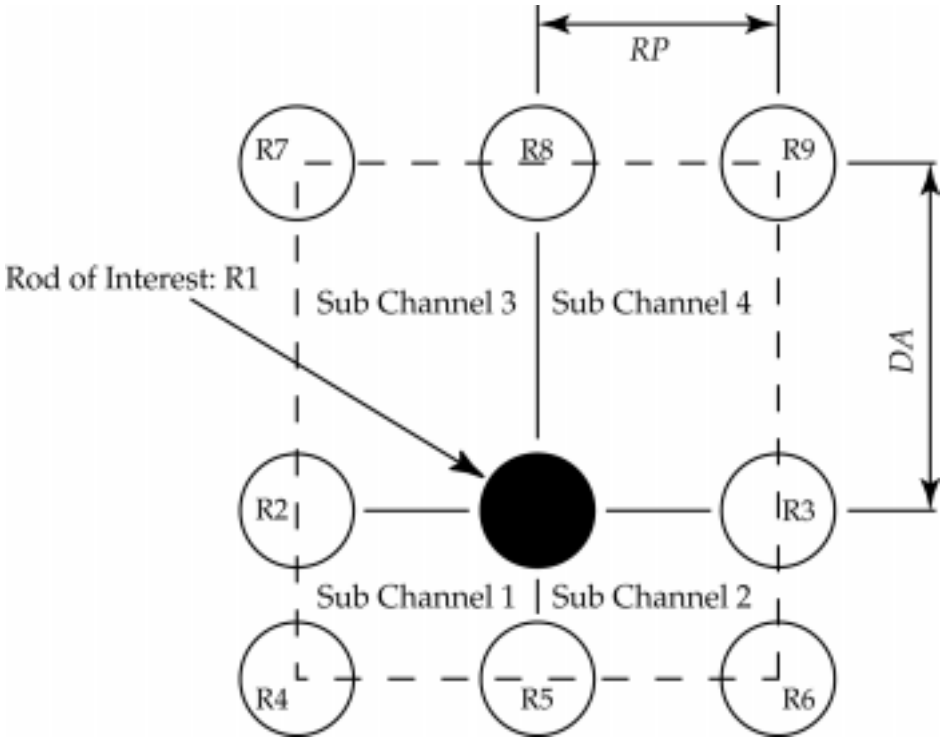

Figure A2 Sample Flow Area for Effective Heated Diameter Calculation

A.4 CORE AVERAGE POWER HISTORY INPUT

The *POW data block input card allows the user to input power history information into PFCC. For Farley-1, the Average Power is a constant 5.2 kw/ft for each cycle (see Table A1). For Farley-2, the Average Power is presented in Figure A3.

The Rod Radial Power Factors (RPF) and the Fast Flux Multipliers (FF Mult) are treated as constants for each individual rod and cycle in the Farley analysis. Values for RPF and FF Mult, along with the Effective Heated Diameter (Heated Dia) are presented in Tables A2 through A9.

The *POW data block input card is also used to input the index of the Axial Power Shape Profile and the Axial Fast Neutron Flux Profile as a function of time. The axial profiles are presented in Section A.6.

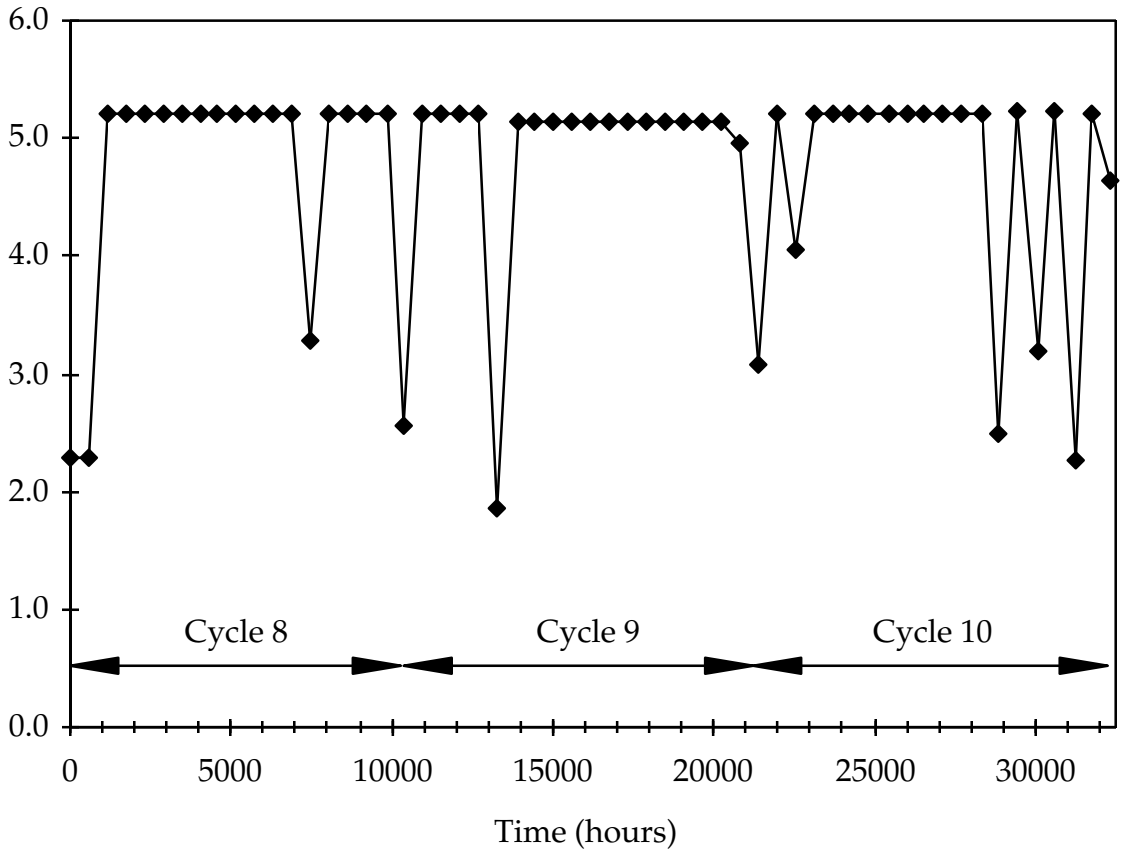

Figure A3 Farley-2 Input Average Power Level

Table A2 Farley-2 EOC10 1-Cycle Rods Power Inputs

Assembly	Face	Rod	RPF	FF Mult	Heated Dia	Assembly	Face	Rod	RPF	FF Mult	Heated Dia
2M15	1	6	1.45	1.409	0.5746	2M56	1	6	1.41	1.405	0.5460
2M15	1	7	1.45	1.409	0.5746	2M56	1	7	1.39	1.403	0.5429
2M15	1	8	1.45	1.409	0.5746	2M56	1	8	1.37	1.402	0.5429
2M15	1	9	1.45	1.409	0.5746	2M56	1	9	1.35	1.400	0.5427
2M15	1	10	1.45	1.409	0.5749	2M56	1	10	1.33	1.398	0.5422
2M15	1	11	1.45	1.409	0.5753	2M56	1	11	1.31	1.396	0.5386
2M09	4	7	1.44	1.408	0.5749	2M55	1	6	1.30	1.395	0.5370
2M09	4	8	1.44	1.408	0.5746	2M55	1	7	1.33	1.398	0.5431
2M09	4	9	1.44	1.408	0.5742	2M55	1	8	1.35	1.400	0.5422
2M13	1	6	1.44	1.408	0.5755	2M55	1	9	1.37	1.402	0.5458
2M13	1	7	1.44	1.408	0.5751	2M54	2	6	1.22	1.388	0.5350
2M13	1	8	1.44	1.408	0.5746	2M54	2	7	1.25	1.390	0.5419
2M13	1	9	1.44	1.408	0.5742	2M54	2	8	1.27	1.392	0.5421
2M24	1	6	1.45	1.409	0.5761	2M54	2	9	1.28	1.393	0.5427
2M24	1	7	1.45	1.409	0.5773	2M54	3	6	1.09	1.375	0.5728
2M24	1	8	1.44	1.408	0.5759	2M54	3	7	1.09	1.375	0.5728
2M24	1	9	1.43	1.407	0.5738	2M54	3	8	1.09	1.375	0.5728
2M29	3	6	1.45	1.409	0.5761	2M54	3	9	1.09	1.375	0.5728
2M29	3	7	1.45	1.409	0.5773	2M55	3	13	0.80	1.348	0.6015
2M29	3	8	1.44	1.408	0.5759	2M55	3	14	0.75	1.343	0.5869
2M29	3	9	1.43	1.407	0.5738	2M55	3	15	0.70	1.339	0.5877
2M19	4	5	1.40	1.404	0.5728	2M55	3	16	0.65	1.334	0.5698
2M19	4	6	1.42	1.406	0.5783	2M46	1	2	0.65	1.334	0.5666
2M19	4	7	1.42	1.406	0.5748	2M46	1	3	0.70	1.338	0.5837
2M19	4	8	1.43	1.407	0.5768	2M46	1	4	0.75	1.343	0.5827
2M19	4	9	1.43	1.407	0.5745	2M46	1	5	0.80	1.348	0.5973
2M19	4	10	1.44	1.408	0.5773	2M49	3	13	0.79	1.347	0.6045
2M46	3	6	1.42	1.406	0.5456	2M49	3	14	0.74	1.343	0.5874
2M46	3	7	1.40	1.405	0.5413	2M49	3	15	0.70	1.338	0.5931
2M46	3	8	1.39	1.403	0.5437	2M49	3	16	0.65	1.334	0.5736
2M46	3	9	1.37	1.401	0.5397						
2M49	1	6	1.34	1.399	0.5387						
2M49	1	7	1.36	1.401	0.5419						
2M49	1	8	1.38	1.402	0.5430						
2M49	1	9	1.39	1.404	0.5435						

Table A3 Farley-2 EOC10 2-Cycle Rods Power Inputs

Assembly	Face	Rod	C9 RPF	C10 RPF	C9 FF Mult	C10 FF Mult	C9 Heated Dia	C10 Heated Dia
2L55	2	6	1.39	1.07	1.336	1.373	0.5622	0.5407
2L55	2	7	1.39	1.06	1.336	1.372	0.5633	0.5383
2L55	2	8	1.38	1.05	1.335	1.372	0.5612	0.5374
2L55	2	9	1.38	1.04	1.335	1.371	0.5623	0.5345
2L26	2	6	1.37	1.05	1.334	1.371	0.5583	0.4966
2L26	2	7	1.37	1.06	1.334	1.372	0.5583	0.5005
2L26	2	10	1.37	1.08	1.334	1.374	0.5583	0.4998
2L26	2	11	1.37	1.08	1.334	1.374	0.5583	0.4987
2L26	2	12	1.37	1.08	1.334	1.375	0.5591	0.4984
2L26	2	13	1.36	1.08	1.334	1.374	0.5560	0.4984
2L54	1	6	1.37	1.10	1.334	1.376	0.5583	0.5474
2L54	1	7	1.37	1.10	1.334	1.376	0.5591	0.5484
2L54	1	8	1.36	1.09	1.334	1.376	0.5565	0.5451
2L54	1	9	1.36	1.09	1.333	1.375	0.5573	0.5462
2L51	2	7	1.36	1.09	1.333	1.375	0.5546	0.5475
2L51	2	8	1.36	1.09	1.334	1.375	0.5550	0.5471
2L51	2	9	1.36	1.09	1.333	1.375	0.5544	0.5465
2L51	2	10	1.37	1.09	1.334	1.375	0.5570	0.5462
2L51	2	11	1.37	1.09	1.334	1.375	0.5562	0.5462
2L51	2	12	1.37	1.09	1.335	1.375	0.5562	0.5462
2L56	1	6	1.36	1.09	1.333	1.376	0.5576	0.5475
2L56	1	7	1.36	1.09	1.333	1.375	0.5566	0.5475
2L56	1	8	1.36	1.09	1.334	1.375	0.5555	0.5471
2L56	1	9	1.36	1.09	1.333	1.375	0.5552	0.5467
2L28	4	7	1.36	1.09	1.333	1.375	0.5597	0.4998
2L28	4	8	1.35	1.09	1.333	1.375	0.5566	0.4989
2L28	4	9	1.35	1.10	1.332	1.376	0.5577	0.5018
2L28	4	10	1.35	1.10	1.333	1.376	0.5583	0.5013
2L28	4	11	1.35	1.09	1.332	1.375	0.5585	0.4979
2L28	4	12	1.35	1.09	1.332	1.375	0.5585	0.4987
2L48	4	6	1.31	1.12	1.328	1.378	0.5605	0.5079
2L48	4	7	1.30	1.13	1.328	1.379	0.5570	0.5112
2L48	4	8	1.30	1.13	1.328	1.379	0.5573	0.5089
2L48	4	9	1.30	1.14	1.328	1.380	0.5571	0.5121
2L40	3	6	1.31	1.13	1.328	1.378	0.5605	0.5102
2L40	3	7	1.30	1.13	1.328	1.379	0.5570	0.5089
2L40	3	8	1.30	1.14	1.328	1.379	0.5573	0.5117
2L40	3	9	1.30	1.14	1.328	1.380	0.5571	0.5108
2L43	1	6	1.31	1.13	1.328	1.378	0.5605	0.5102

Table A3 Farley-2 EOC10 2-Cycle Rods Power Inputs (continued)

Assembly	Face	Rod	C9 RPF	C10 RPF	C9 FF Mult	C10 FF Mult	C9 Heated Dia	C10 Heated Dia
2L43	1	7	1.30	1.13	1.328	1.379	0.5570	0.5089
2L43	1	8	1.30	1.14	1.328	1.379	0.5573	0.5117
2L43	1	9	1.30	1.14	1.328	1.380	0.5571	0.5108
2L08	4	6	1.30	1.08	1.328	1.374	0.5361	0.4988
2L08	4	7	1.28	1.08	1.326	1.374	0.5318	0.4995
2L08	4	8	1.27	1.08	1.325	1.374	0.5342	0.5005
2L08	4	9	1.25	1.08	1.324	1.375	0.5295	0.5012
2L02	1	4	1.29	1.07	1.327	1.373	0.5323	0.4970
2L02	1	5	1.29	1.08	1.327	1.374	0.5333	0.4998
2L02	1	6	1.28	1.08	1.326	1.375	0.5335	0.4975
2L02	1	7	1.26	1.09	1.324	1.375	0.5328	0.5010
2L02	1	8	1.24	1.09	1.323	1.375	0.5332	0.5009
2L02	1	9	1.22	1.09	1.321	1.375	0.5299	0.5015
2L37	1	6	1.29	1.14	1.327	1.380	0.5472	0.5097
2L37	1	7	1.26	1.14	1.325	1.380	0.5421	0.5089
2L37	1	8	1.23	1.15	1.322	1.380	0.5409	0.5122
2L37	1	9	1.21	1.15	1.320	1.381	0.5385	0.5117
2L07	4	6	1.28	1.08	1.326	1.374	0.5360	0.4988
2L07	4	7	1.26	1.08	1.324	1.374	0.5328	0.4983
2L07	4	8	1.24	1.09	1.323	1.375	0.5332	0.5023
2L07	4	9	1.22	1.09	1.321	1.375	0.5299	0.5022
2L50	2	6	1.27	1.10	1.325	1.377	0.5701	0.5499
2L50	2	7	1.25	1.10	1.323	1.376	0.5660	0.5499
2L50	2	8	1.23	1.10	1.322	1.376	0.5642	0.5499
2L50	2	9	1.22	1.10	1.321	1.376	0.5635	0.5499
2L53	1	6	1.27	1.10	1.325	1.376	0.5701	0.5499
2L53	1	7	1.25	1.10	1.323	1.376	0.5660	0.5499
2L53	1	8	1.23	1.10	1.322	1.376	0.5642	0.5510
2L53	1	9	1.22	1.09	1.321	1.376	0.5635	0.5471
2L57	3	6	1.27	1.10	1.325	1.377	0.5701	0.5512
2L57	3	7	1.25	1.10	1.323	1.376	0.5660	0.5512
2L57	3	8	1.23	1.10	1.322	1.376	0.5642	0.5509
2L57	3	9	1.22	1.10	1.321	1.376	0.5635	0.5504
2L03	4	6	1.20	1.05	1.319	1.371	0.5286	0.4988
2L03	4	7	1.22	1.06	1.321	1.372	0.5320	0.5009
2L03	4	8	1.24	1.07	1.323	1.373	0.5330	0.5015
2L03	4	9	1.25	1.08	1.324	1.374	0.5338	0.5040
2L05	2	6	1.14	1.08	1.314	1.374	0.5262	0.5023
2L05	2	7	1.17	1.08	1.316	1.374	0.5320	0.5016

Table A3 Farley-2 EOC10 2-Cycle Rods Power Inputs (continued)

Assembly	Face	Rod	C9 RPF	C10 RPF	C9 FF Mult	C10 FF Mult	C9 Heated Dia	C10 Heated Dia
2L05	2	8	1.20	1.08	1.319	1.375	0.5336	0.4987
2L05	2	9	1.22	1.10	1.321	1.376	0.5365	0.5053
2L04	3	6	1.14	1.08	1.314	1.374	0.5262	0.5023
2L04	3	7	1.17	1.08	1.316	1.374	0.5320	0.5007
2L04	3	8	1.20	1.09	1.319	1.375	0.5336	0.5019
2L04	3	9	1.22	1.10	1.321	1.376	0.5365	0.5040
2L01	4	6	1.14	1.07	1.314	1.374	0.5262	0.4995
2L01	4	7	1.17	1.08	1.316	1.374	0.5320	0.5025
2L01	4	8	1.20	1.08	1.319	1.374	0.5336	0.4999
2L01	4	9	1.22	1.09	1.321	1.376	0.5365	0.5033
2L33	2	6	1.13	1.06	1.313	1.372	0.5353	0.5124
2L33	2	7	1.16	1.06	1.316	1.373	0.5411	0.5101
2L33	2	8	1.19	1.07	1.318	1.373	0.5426	0.5107
2L33	2	9	1.21	1.08	1.319	1.374	0.5454	0.5129
2L34	1	6	1.13	1.06	1.313	1.372	0.5353	0.5124
2L34	1	7	1.16	1.06	1.316	1.373	0.5411	0.5101
2L34	1	8	1.19	1.07	1.318	1.373	0.5426	0.5107
2L34	1	9	1.21	1.08	1.319	1.374	0.5454	0.5129
2L36	4	6	1.13	1.06	1.313	1.372	0.5353	0.5124
2L36	4	7	1.16	1.06	1.316	1.373	0.5411	0.5101
2L36	4	8	1.19	1.07	1.318	1.373	0.5426	0.5107
2L36	4	9	1.21	1.08	1.319	1.374	0.5454	0.5129
2L39	3	6	1.13	1.06	1.313	1.372	0.5353	0.5101
2L39	3	7	1.16	1.06	1.316	1.373	0.5411	0.5084
2L39	3	8	1.19	1.07	1.318	1.373	0.5426	0.5101
2L39	3	9	1.21	1.08	1.319	1.374	0.5454	0.5129
2L44	2	7	1.06	1.02	1.307	1.369	0.5739	0.5136
2L44	2	8	1.08	1.02	1.308	1.368	0.5812	0.5167
2L44	2	9	1.08	1.00	1.308	1.367	0.5765	0.5111
2L44	2	10	1.09	0.99	1.309	1.365	0.5769	0.5109
2L44	2	11	1.11	0.98	1.311	1.364	0.5802	0.5109
2L44	2	12	1.12	0.97	1.312	1.363	0.5809	0.5089
2L31	3	6	1.05	1.03	1.306	1.370	0.5761	0.5145
2L31	3	7	1.06	1.02	1.307	1.369	0.5769	0.5113
2L31	3	8	1.08	1.02	1.308	1.368	0.5812	0.5155
2L31	3	9	1.08	1.00	1.308	1.367	0.5779	0.5083
2L46	4	6	1.05	1.02	1.306	1.369	0.5761	0.5142
2L46	4	7	1.06	1.01	1.307	1.368	0.5769	0.5110
2L46	4	8	1.08	1.01	1.308	1.367	0.5812	0.5153

Table A3 Farley-2 EOC10 2-Cycle Rods Power Inputs (continued)

Assembly	Face	Rod	C9 RPF	C10 RPF	C9 FF Mult	C10 FF Mult	C9 Heated Dia	C10 Heated Dia
2L46	4	9	1.08	0.99	1.308	1.366	0.5779	0.5080
2L49	1	6	1.12	0.96	1.312	1.363	0.5804	0.5082
2L49	1	7	1.10	0.97	1.310	1.364	0.5751	0.5100
2L49	1	8	1.09	0.98	1.309	1.365	0.5770	0.5093
2L49	1	9	1.08	1.00	1.308	1.366	0.5750	0.5161
2L30	1	6	1.05	1.03	1.306	1.370	0.5761	0.5145
2L30	1	7	1.06	1.02	1.307	1.369	0.5769	0.5113
2L30	1	8	1.08	1.02	1.308	1.368	0.5812	0.5155
2L30	1	9	1.08	1.00	1.308	1.367	0.5779	0.5083
2L30	3	6	1.39	0.34	1.336	1.305	0.5667	0.7112
2L30	3	7	1.38	0.35	1.335	1.306	0.5636	0.7199
2L30	3	8	1.38	0.36	1.335	1.307	0.5654	0.7144
2L30	3	9	1.37	0.38	1.334	1.308	0.5622	0.7360
2L33	3	2	0.60	0.53	1.265	1.323	0.5788	0.5543
2L33	3	3	0.63	0.57	1.268	1.326	0.5875	0.5728
2L33	3	4	0.67	0.60	1.271	1.329	0.5920	0.5657
2L33	3	5	0.70	0.64	1.274	1.333	0.5996	0.5820

Table A4 Farley-2 EOC10 3-Cycle Rods Power Inputs

Assembly	Face	Rod	C8 RPF	C9 RPF	C10 RPF	C8 FF Mult	C9 FF Mult	C10 FF Mult	C8 Heated Dia	C9 Heated Dia	C10 Heated Dia
Y08	3	7	1.31	1.03	0.94	1.387	1.304	1.362	0.5094	0.5121	0.4425
Y08	3	8	1.31	1.03	0.95	1.388	1.304	1.362	0.5090	0.5118	0.4465
Y08	3	9	1.31	1.03	0.95	1.388	1.304	1.362	0.5087	0.5112	0.4459
Y08	3	10	1.31	1.03	0.95	1.388	1.304	1.362	0.5090	0.5112	0.4456
Y08	3	11	1.31	1.03	0.95	1.387	1.304	1.362	0.5103	0.5115	0.4462
Y08	3	12	1.30	1.03	0.94	1.387	1.304	1.361	0.5076	0.5113	0.4425
Y04	4	6	1.28	1.18	0.85	1.385	1.317	1.353	0.4950	0.4771	0.4768
Y04	4	7	1.26	1.18	0.85	1.384	1.317	1.353	0.4905	0.4763	0.4768
Y04	4	8	1.25	1.19	0.85	1.383	1.318	1.353	0.4913	0.4790	0.4768
Y04	4	9	1.24	1.19	0.85	1.382	1.318	1.353	0.4912	0.4782	0.4768
Y04	4	10	1.23	1.19	0.85	1.382	1.318	1.353	0.4926	0.4782	0.4768
Y04	4	11	1.21	1.19	0.85	1.380	1.318	1.353	0.4886	0.4782	0.4768
Y13	2	7	1.30	0.59	0.68	1.387	1.264	1.336	0.5096	0.4954	0.4521
Y13	2	8	1.31	0.62	0.65	1.387	1.267	1.334	0.5096	0.5078	0.4399
Y13	2	9	1.31	0.64	0.64	1.387	1.269	1.333	0.5067	0.5046	0.4450
Y13	2	10	1.31	0.66	0.62	1.387	1.271	1.331	0.5067	0.5021	0.4427
Y13	2	11	1.31	0.69	0.60	1.387	1.273	1.329	0.5067	0.5046	0.4438
Y13	2	12	1.31	0.72	0.57	1.387	1.276	1.326	0.5067	0.5134	0.4319
Y21	4	6	1.29	0.56	0.70	1.386	1.262	1.338	0.5053	0.4947	0.4526
Y21	4	7	1.30	0.59	0.67	1.387	1.264	1.336	0.5069	0.5056	0.4418
Y21	4	8	1.31	0.62	0.65	1.387	1.267	1.334	0.5078	0.5078	0.4412
Y21	4	9	1.31	0.64	0.64	1.387	1.269	1.333	0.5078	0.5078	0.4412
Y34	1	6	0.77	1.13	0.59	1.346	1.313	1.328	0.5194	0.4748	0.4954
Y34	1	7	0.80	1.14	0.55	1.349	1.314	1.325	0.5249	0.4757	0.4790
Y34	1	8	0.84	1.16	0.52	1.351	1.315	1.322	0.5287	0.4797	0.4807
Y34	1	9	0.86	1.16	0.49	1.353	1.316	1.319	0.5296	0.4778	0.4686

Table A5 Farley-2 EOC9 1-Cycle Rods Power Inputs

Assembly	Rod	RPF	FF Mult	Heated Dia
2L51	F17	1.37	1.350	0.5625
2L51	G17	1.37	1.350	0.5623
2L51	H17	1.37	1.350	0.5623
2L51	I17	1.36	1.349	0.5609
2L51	J17	1.37	1.349	0.5633
2L51	K17	1.36	1.349	0.5621
2L26	E17	1.36	1.349	0.5550
2L26	F17	1.37	1.350	0.5574
2L26	G17	1.37	1.350	0.5560
2L26	H17	1.37	1.350	0.5554
2L26	K17	1.37	1.350	0.5561
2L26	L17	1.37	1.350	0.5563
2L02	A09	1.22	1.336	0.5281
2L02	A10	1.24	1.338	0.5307
2L02	A11	1.26	1.340	0.5307
2L02	A12	1.28	1.342	0.5315
2L02	A13	1.29	1.343	0.5315
2L02	A14	1.29	1.343	0.5301
2L33	A08	1.24	1.338	0.5548
2L33	A09	1.24	1.338	0.5541
2L33	A10	1.26	1.339	0.5565
2L33	A11	1.26	1.340	0.5563
2L33	A12	1.27	1.341	0.5579
2L33	A13	1.27	1.341	0.5570

Table A6 Farley-2 EOC9 2-Cycle Rods Power Inputs

Assembly	Rod	C8 RPF	C9 RPF	C8 FF Mult	C9 FF Mult	C8 Heated Dia	C9 Heated Dia
Y04	F01	1.28	1.18	1.379	1.632	0.4939	0.4747
Y04	G01	1.26	1.18	1.378	1.630	0.4920	0.4753
Y04	H01	1.25	1.19	1.377	1.629	0.4923	0.4763
Y04	I01	1.24	1.19	1.376	1.627	0.4911	0.4762
Y04	J01	1.23	1.19	1.376	1.625	0.4930	0.4758
Y04	K01	1.21	1.19	1.374	1.622	0.4884	0.4757
Y09	H01	1.31	1.21	1.382	1.640	0.5207	0.4769
Y09	I01	1.31	1.21	1.382	1.640	0.5187	0.4789
Y09	Q11	1.30	1.20	1.381	1.637	0.5110	0.4759
Y09	Q12	1.29	1.20	1.380	1.636	0.5095	0.4775
Y09	Q13	1.28	1.19	1.379	1.633	0.5099	0.4776
Y09	Q14	1.26	1.17	1.378	1.629	0.5065	0.4733
Y10	Q06	1.31	1.21	1.382	1.639	0.5204	0.4762
Y10	Q07	1.31	1.21	1.381	1.639	0.5198	0.4765
Y10	Q08	1.31	1.21	1.382	1.640	0.5210	0.4771
Y10	Q09	1.31	1.21	1.382	1.640	0.5200	0.4778
Y10	Q10	1.31	1.21	1.382	1.640	0.5223	0.4771
Y10	Q11	1.31	1.21	1.381	1.639	0.5206	0.4764

Table A7 Farley-1 EOC13 1-Cycle Rods Power Inputs

Assembly	Face	Rod	RPF	FF Mult	Heated Dia
2E30	4	6	1.46	1.391	0.5729
2E30	4	7	1.46	1.391	0.5725
2E30	4	8	1.46	1.391	0.5727
2E30	4	9	1.46	1.390	0.5706
2E30	4	10	1.46	1.391	0.5725
2E30	4	11	1.46	1.391	0.5722
2E57	3	7	1.42	1.387	0.5670
2E57	3	8	1.43	1.388	0.5691
2E57	3	9	1.43	1.388	0.5660
2E57	3	10	1.45	1.389	0.5676
2E57	3	11	1.46	1.390	0.5677
2E57	3	12	1.47	1.391	0.5693
2E45	2	4	1.44	1.388	0.5687
2E45	2	5	1.45	1.390	0.5725
2E45	2	6	1.45	1.390	0.5726
2E45	2	7	1.44	1.389	0.5714
2E45	2	8	1.43	1.388	0.5715
2E45	2	9	1.42	1.386	0.5674
2E11	3	6	1.44	1.388	0.5389
2E11	3	7	1.44	1.388	0.5393
2E11	3	8	1.44	1.388	0.5398
2E11	3	9	1.44	1.388	0.5388
2E11	3	10	1.44	1.389	0.5398
2E11	3	11	1.44	1.388	0.5389
2E50	3	4	1.37	1.381	0.5374
2E50	3	5	1.38	1.382	0.5405
2E50	3	6	1.37	1.382	0.5398
2E50	3	7	1.36	1.380	0.5390
2E50	3	8	1.34	1.378	0.5397
2E50	3	9	1.32	1.376	0.5360

Table A8 Farley-1 EOC13 2-Cycle Rods Power Inputs

Assembly	Face	Rod	C12 RPF	C13 RPF	C12 FF Mult	C13 FF Mult	C12 Heated Diam	C13 Heated Diam
2D07	3	6	1.47	1.09	1.342	1.614	0.5390	0.5002
2D07	3	7	1.47	1.09	1.342	1.614	0.5393	0.5002
2D07	3	8	1.47	1.09	1.342	1.614	0.5406	0.5015
2D07	3	9	1.46	1.09	1.341	1.612	0.5365	0.5016
2D07	3	10	1.47	1.09	1.342	1.614	0.5404	0.5010
2D07	3	11	1.47	1.09	1.342	1.614	0.5393	0.4996
2D50	3	6	1.44	1.18	1.339	1.618	0.5846	0.5111
2D50	3	7	1.43	1.18	1.339	1.618	0.5836	0.5106
2D50	3	8	1.43	1.18	1.339	1.618	0.5814	0.5118
2D50	3	9	1.44	1.18	1.338	1.618	0.5851	0.5121
2D50	3	10	1.44	1.18	1.339	1.617	0.5844	0.5114
2D50	3	11	1.44	1.17	1.339	1.617	0.5852	0.5101
2D02	2	5	1.38	1.09	1.334	1.597	0.5312	0.5004
2D02	2	6	1.37	1.10	1.334	1.598	0.5320	0.5026
2D02	2	7	1.36	1.10	1.333	1.596	0.5312	0.5023
2D02	2	8	1.34	1.11	1.332	1.594	0.5310	0.5035
2D02	2	9	1.33	1.12	1.331	1.592	0.5311	0.5073
2D02	2	10	1.32	1.10	1.329	1.588	0.5285	0.5011
2D29	4	5	1.37	1.18	1.334	1.606	0.5705	0.5107
2D29	4	6	1.37	1.19	1.333	1.606	0.5701	0.5135
2D29	4	7	1.35	1.19	1.332	1.604	0.5693	0.5131
2D29	4	8	1.34	1.20	1.331	1.602	0.5691	0.5155
2D29	4	9	1.32	1.20	1.330	1.599	0.5662	0.5146
2D29	4	10	1.31	1.19	1.329	1.596	0.5667	0.5118
2D41	4	6	1.30	1.15	1.328	1.590	0.5663	0.5499
2D41	4	7	1.31	1.15	1.329	1.592	0.5679	0.5487
2D41	4	8	1.32	1.15	1.329	1.593	0.5679	0.5492
2D41	4	9	1.32	1.14	1.330	1.594	0.5663	0.5475
2D41	4	10	1.34	1.15	1.331	1.597	0.5690	0.5490
2D41	4	11	1.35	1.15	1.332	1.600	0.5717	0.5484

Table A8 Farley-1 EOC13 2-Cycle Rods Power Inputs

Assembly	Face	Rod	C11 RPF	C12 RPF	C13 RPF	C11 FF Mult	C12 FF Mult	C13 FF Mult	C11 Heated Dia	C12 Heated Dia	C13 Heated Dia
2C12	3	9	1.30	0.87	0.96	1.406	1.633	1.839	0.5102	0.4569	0.4442
2C12	3	10	1.30	0.88	0.96	1.406	1.633	1.841	0.5110	0.4582	0.4444
2C12	3	11	1.29	0.89	0.96	1.406	1.633	1.841	0.5099	0.4581	0.4430
2C12	3	12	1.28	0.90	0.95	1.405	1.634	1.842	0.5106	0.4584	0.4432
2C12	3	13	1.28	0.91	0.95	1.405	1.633	1.841	0.5102	0.4590	0.4432
2C12	3	14	1.26	0.91	0.94	1.403	1.630	1.838	0.5074	0.4581	0.4405
2C60	1	6	0.82	1.16	0.72	1.364	1.569	1.777	0.5091	0.5065	0.4377
2C60	1	7	0.87	1.15	0.73	1.368	1.576	1.785	0.5195	0.5039	0.4413
2C60	1	8	0.91	1.15	0.75	1.371	1.583	1.793	0.5215	0.5034	0.4423
2C60	1	9	0.93	1.14	0.76	1.373	1.587	1.798	0.5178	0.5021	0.4416
2C60	1	10	0.96	1.14	0.77	1.376	1.592	1.804	0.5173	0.5027	0.4396
2C60	1	11	0.99	1.14	0.79	1.379	1.598	1.812	0.5256	0.5029	0.4432

A.5 LITHIUM CHEMISTRY INFORMATION

The *LIT data block is used to input lithium concentration as a function of time into PFCC. Figure A4 contains the lithium chemistry data used as PFCC input for the Farley-1 analysis. Figure A5 contains the lithium data for Farley-2.

A.6 AXIAL POWER DISTRIBUTIONS

The *AXI data block is used to input the normalized axial peaking factors for power and fast neutron flux. The *POW data block input is used to specify which profile should be used as a function of time. The same axial profile shapes for power peaking factors and fast neutron flux were used for the Farley analysis.

There does appear to be some problems with the axial power distributions. One cycle Farley-1 rods in assemblies 2E11, 2E30, 2E45, 2E50, and 2E57 have a large power depression in span 6 for the first 5000 hours of operation during Cycle 13. Two cycle Farley-1 rods in Assemblies 2D02, 2D07, 2D29, 2D41, and 2D50 have a large power depression in span 6 for the first 4000 hours of operation during cycle 12. This reduced power will cause PFCC to underpredict the oxide thickness for these rods.

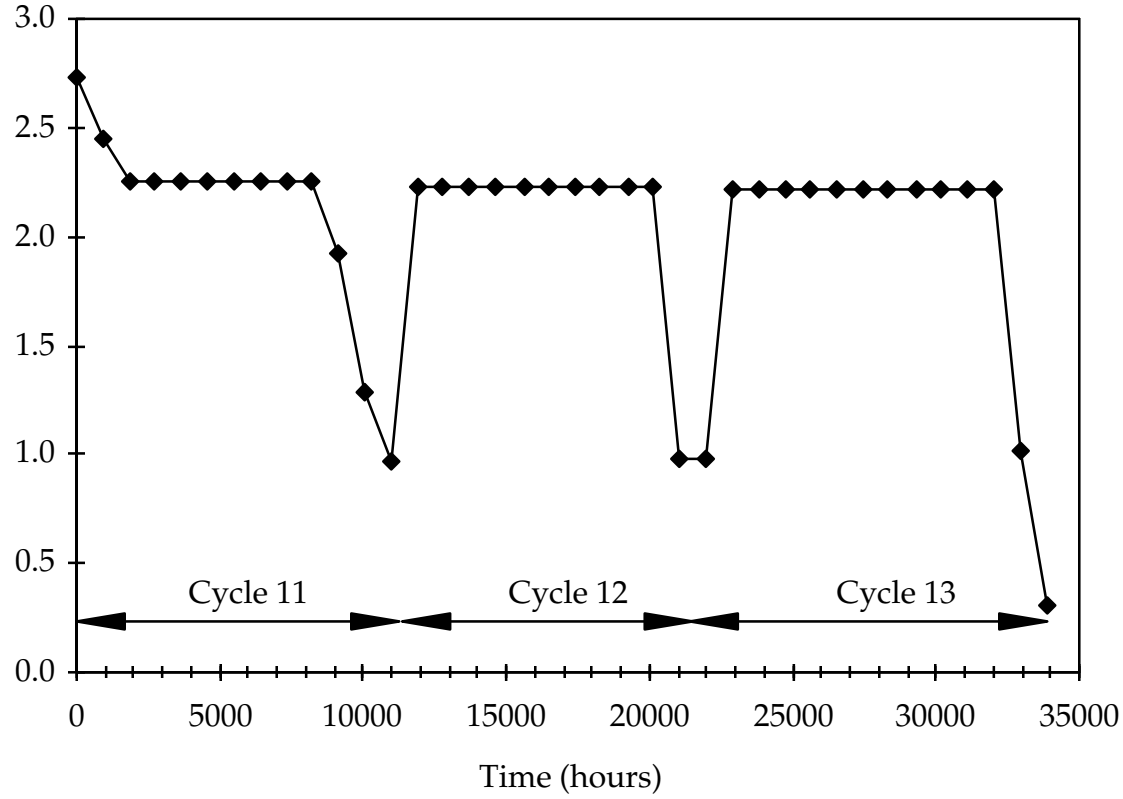

Figure A4 Farley-1 Input Lithium Concentration

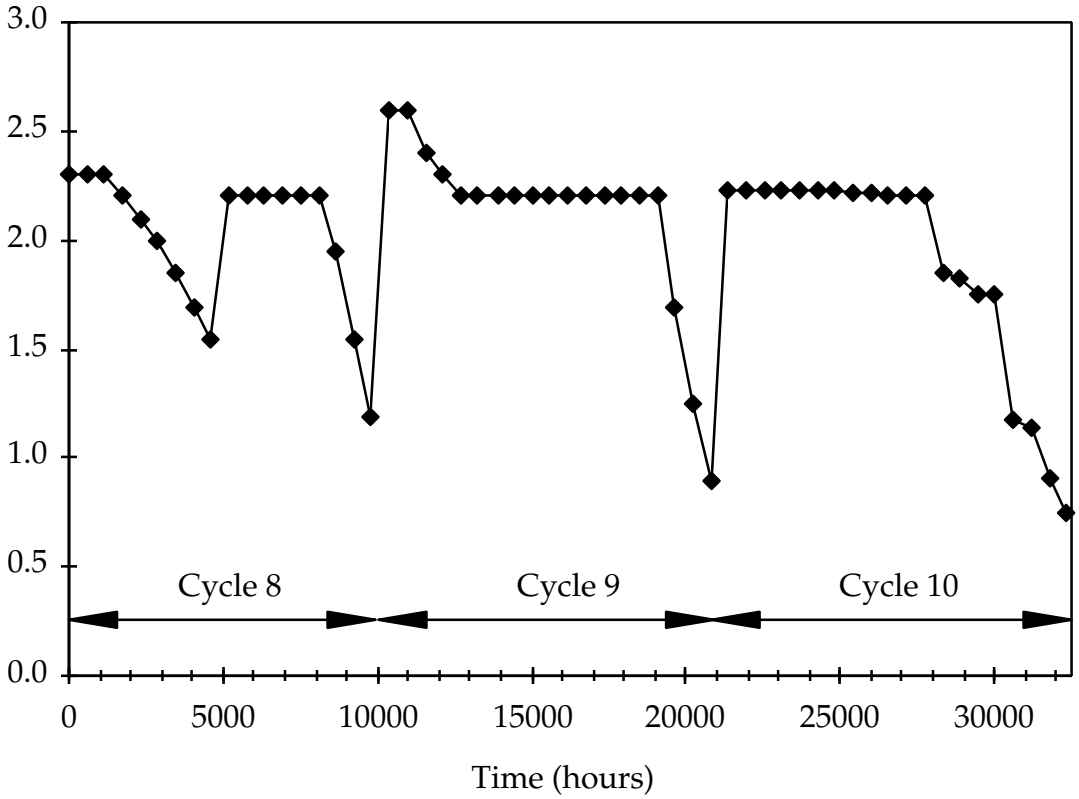

Figure A5 Farley-2 Input Lithium Concentration

Appendix B

PFCC PREDICTED OXIDE THICKNESSES

The largest oxide growth was observed in span 6 for the Farley rods. This span was subdivided in spans 6A and 6B for the rods that contained intermediate flow mixers. Tables B1 through B8 compile the results of the PFCC Farley analysis. In these tables, a "Y" in the "Calculated?" column indicates a PFCC analysis was performed on that specific rod. A "N" indicates that a PFCC calculation was not performed on that rod and the predicted values are taken from a rod that had similar characteristics. "Yb" indicates that a PFCC analysis was performed on the specific rod and that there was some nucleate boiling along the rod for a finite period of time.

A comparison of the PFCC oxide predictions with measurements is presented in Tables B1 through B8.

Table B1 Farley-2 EOC10 1-cycle rod results

Assembly	Face	Rod	Location	Calculated?	Oxide Thickness at Span 6 [µm]				Measured - Predicted [µm]	
					Measured		Predicted			
					6A	6B	6A	6B	6A	6B
2M15	1	6	E8	N	14.2	15.73	11.92	12.03	2.28	3.7
2M15	1	7	E8	N	17.9	14.28	11.92	12.03	5.98	2.25
2M15	1	8	E8	N	14.55	15.98	11.92	12.03	2.63	3.95
2M15	1	9	E8	Yb	16.26	15.9	11.92	12.03	4.34	3.87
2M15	1	10	E8	N	14.85	15.25	11.92	12.03	2.93	3.22
2M15	1	11	E8	Yb	16.57	15.12	11.89	12	4.68	3.12
2M09	4	7	L8	Yb	17.11	17.9	11.68	11.83	5.43	6.07
2M09	4	8	L8	N	16.29	17.47	11.68	11.83	4.61	5.64
2M09	4	9	L8	N	17.29	19.95	11.68	11.83	5.61	8.12
2M13	1	6	H5	Yb	15.22	18.08	11.66	11.81	3.56	6.27
2M13	1	7	H5	N	17.62	17.86	11.66	11.81	5.96	6.05
2M13	1	8	H5	N	16.54	19.33	11.66	11.81	4.88	7.52
2M13	1	9	H5	N	19.53	16.95	11.66	11.81	7.87	5.14
2M24	1	6	M7	Yb	16.46	17.54	11.72	11.88	4.74	5.66
2M24	1	7	M7	N	19.11	18.89	11.72	11.88	7.39	7.01
2M24	1	8	M7	N	14.61	18.54	11.72	11.88	2.89	6.66
2M24	1	9	M7	Y	21.73	21.13	11.37	11.54	10.36	9.59
2M29	3	6	D9	Yb	17.61	19.23	11.72	11.88	5.89	7.35

Table B1 Farley-2 EOC10 1-cycle rod results (continued)

Assembly	Face	Rod	Location	Calculated?	Oxide Thickness at Span 6 [µm]				Measured - Predicted [µm]	
					Measured		Predicted			
					6A	6B	6A	6B	6A	6B
2M29	3	7	D9	N	17.65	17.72	11.72	11.88	5.93	5.84
2M29	3	8	D9	N	14.58	17.68	11.72	11.88	2.86	5.8
2M29	3	9	D9	N	19.91	19.93	11.72	11.88	8.19	8.05
2M19	4	5	G12?	Y	18.06	37.21	10.8	10.93	7.26	26.28
2M19	4	6	G12	N	16.63	15	10.8	10.93	5.83	4.07
2M19	4	7	G12	N	18.1	22.18	10.8	10.93	7.3	11.25
2M19	4	8	G12	N	14.24	30.04	10.8	10.93	3.44	19.11
2M19	4	9	G12	Y	14.61	25.76	11.35	11.52	3.26	14.24
2M19	4	10	G12	N	16.93	36.79	11.35	11.52	5.58	25.27
2M46	3	6	E13/y	N	18.86	26.07	12	11.95	6.86	14.12
2M46	3	7	E13/y	Yb	20.7	22.19	12	11.95	8.7	10.24
2M46	3	8	E13/y	N	16.22	20.09	11.34	11.54	4.88	8.55
2M46	3	9	E13/y	Yb	20.8	21.73	11.34	11.54	9.46	10.19
2M49	1	6	N11/y	N	19.4	20.32	11.08	11.28	8.32	9.04
2M49	1	7	N11/y	Y	18.74	21.52	11.08	11.28	7.66	10.24
2M49	1	8	N11/y	N	18.65	19.39	11.66	11.78	6.99	7.61
2M49	1	9	N11/y	Yb	18.32	23.14	11.66	11.78	6.66	11.36
2M56	1	6	L3/y	Yb	25	29.99	12.08	11.98	12.92	18.01
2M56	1	7	L3/y	N	15.39	25.59	12.08	11.98	3.31	13.61
2M56	1	8	L3/y	Y	12.83	26.13	11.25	11.46	1.58	14.67
2M56	1	9	L3/y	N	15	19.62	11.25	11.46	3.75	8.16
2M56	1	10	L3/y	N	16.11	23.45	11.25	11.46	4.86	11.99
2M56	1	11	L3/y	Y	17.69	17.22	10.22	10.41	7.47	6.81
2M55	1	6	L13/	Y	17.63	19.6	10.08	10.72	7.55	8.88
2M55	1	7	L13/y	N	19.5	23.33	10.08	10.72	9.42	12.61
2M55	1	8	L13/y	N	17.18	19.99	11.17	11.37	6.01	8.62
2M55	1	9	L13/y	Y	16.6	22.17	11.17	11.37	5.43	10.8
2M54	2	6	P8/y	Y	17.15	17.21	8.74	8.98	8.41	8.23
2M54	2	7	P8/y	N	18.34	21.18	8.74	8.98	9.6	12.2
2M54	2	8	P8/y	N	19.27	20.55	9.54	9.78	9.73	10.77
2M54	2	9	P8/y	Y	17.37	18.86	9.54	9.78	7.83	9.08
2M54	3	6	P8/n	N	16.43	16.25	6.31	6.5	10.12	9.75
2M54	3	7	P8/n	N	13.76	14.57	6.31	6.5	7.45	8.07
2M54	3	8	P8/n	Y	15.75	15.69	6.31	6.5	9.44	9.19
2M54	3	9	P8/n	N	13.74	16.59	6.31	6.5	7.43	10.09
2M55	3	13	L13/n	Y	9.25	12.13	3.21	3.33	6.04	8.8
2M55	3	14	L13/n	N	8.8	12.52	3.21	3.33	5.59	9.19
2M55	3	15	L13/n	N	9.82	10.76	2.09	2.28	7.73	8.48

Table B1 Farley-2 EOC10 1-cycle rod results (continued)

Assembly	Face	Rod	Location	Calculated?	Oxide Thickness at Span 6 [µm]				Measured - Predicted [µm]	
					Measured		Predicted			
					6A	6B	6A	6B	6A	6B
2M55	3	16	L13/n	Y	9.12	8.89	2.09	2.28	7.03	6.61
2M46	1	2	E13/n	Y	10.82	8.57	2.11	2.31	8.71	6.26
2M46	1	3	E13/n	N	10.07	10.26	2.11	2.31	7.96	7.95
2M46	1	4	E13/n	Y	9.76	11.58	2.93	3.1	6.83	8.48
2M46	1	5	E13/n	N	10.15	11.26	2.93	3.1	7.22	8.16
2M49	3	13	N11/n	Y	12.55	11.57	3.11	3.29	9.44	8.28
2M49	3	14	N11/n	N	10.34	12.33	3.11	3.29	7.23	9.04
2M49	3	15	N11/n	Y	10.52	11.95	2.38	2.56	8.14	9.39
2M49	3	16	N11/n	N	10.13	12.13	2.38	2.56	7.75	9.57

Table B2 Farley-2 EOC10 2-cycle rod results

Assembly	Face	Rod	Location	Calculated?	Oxide Thickness at Span 6 [µm]				Measured - Predicted [µm]	
					Measured		Predicted			
					6A	6B	6A	6B	6A	6B
2L55	2	6	D5/n	Yb	45.51	55.77	38.03	38.62	7.48	17.15
2L55	2	7	D5/n	N	30.27	34.66	38.03	38.62	-7.76	-3.96
2L55	2	8	D5/n	N	29.16	27.71	38.03	38.62	-8.87	-10.91
2L55	2	9	D5/n	N	39.5	43.85	38.03	38.62	1.47	5.23
2L26	2	6	H11	N	34.78	41.24	38.8	39.32	-4.02	1.92
2L26	2	7	H11	Yb	31.97	46.61	38.8	39.32	-6.83	7.29
2L26	2	10	H11	N	37	39.87	38.8	39.32	-1.8	0.55
2L26	2	11	H11	N	33.49	39.76	38.8	39.32	-5.31	0.44
2L26	2	12	H11	N	36.63	42.09	38.8	39.32	-2.17	2.77
2L26	2	13	H11	N	32.42	38.85	38.8	39.32	-6.38	-0.47
2L54	1	6	M5/n	N	51.96	61.59	36.88	37.72	15.08	23.87
2L54	1	7	M5/n	N	40.62	44.7	36.88	37.72	3.74	6.98
2L54	1	8	M5/n	N	32.54	40.77	36.88	37.72	-4.34	3.05
2L54	1	9	M5/n	Yb	43.67	52.2	36.88	37.72	6.79	14.48
2L51	2	7	L4/n	N	28	35	37.68	38.47	-9.68	-3.47
2L51	2	8	L4/n	Yb	42	42	37.68	38.47	4.32	3.53
2L51	2	9	L4/n	N	41	44	37.68	38.47	3.32	5.53
2L51	2	10	L4/n	N	62	70	37.04	37.89	24.96	32.11
2L51	2	11	L4/n	N	38	49	37.04	37.89	0.96	11.11
2L51	2	12	L4/n	Yb	42	42	37.04	37.89	4.96	4.11
2L56	1	6	M11/n	Yb	27.06	32.49	36.8	37.64	-9.74	-5.15
2L56	1	7	M11/n	N	56.49	65.22	36.8	37.64	19.69	27.58
2L56	1	8	M11/n	N	40.04	44.74	36.8	37.64	3.24	7.1

Table B2 Farley-2 EOC10 2-cycle rod results (continued)

Assembly	Face	Rod	Location	Calculated?	Oxide Thickness at Span 6 [µm]				Measured - Predicted [µm]	
					Measured		Predicted			
					6A	6B	6A	6B	6A	6B
2L56	1	9	M11/n	N	33.91	34.93	36.8	37.64	-2.89	-2.71
2L28	4	7	D7	N	37	50	38.85	41.37	-1.85	8.63
2L28	4	8	D7	N	36	34	38.85	41.37	-2.85	-7.37
2L28	4	9	D7	N	35	45	38.85	41.37	-3.85	3.63
2L28	4	10	D7	Y	36	37	38.85	41.37	-2.85	-4.37
2L28	4	11	D7	N	34	50	38.85	41.37	-4.85	8.63
2L28	4	12	D7	N	35	45	38.85	41.37	-3.85	3.63
2L48	4	6	H14/n	Y	35.16	39.02	36.13	39.04	-0.97	-0.02
2L48	4	7	H14/n	N	47.11	47.69	36.13	39.04	10.98	8.65
2L48	4	8	H14/n	N	38.6	43.56	36.13	39.04	2.47	4.52
2L48	4	9	H14/n	N	34.52	37.7	36.13	39.04	-1.61	-1.34
2L40	3	6	B8/n	N	35.51	37.04	36.02	39.17	-0.51	-2.13
2L40	3	7	B8/n	N	38.13	42.46	36.02	39.17	2.11	3.29
2L40	3	8	B8/n	Y	48.75	49.8	36.02	39.17	12.73	10.63
2L40	3	9	B8/n	N	55.89	54	36.02	39.17	19.87	14.83
2L43	1	6	P8/n	Y	35.98	40.3	35.4	38.53	0.58	1.77
2L43	1	7	P8/n	N	32.58	37.97	35.4	38.53	-2.82	-0.56
2L43	1	8	P8/n	N	38.66	47.66	35.4	38.53	3.26	9.13
2L43	1	9	P8/n	N	33.49	38.07	35.4	38.53	-1.91	-0.46
2L08	4	6	L13/y	N	40.97	42.87	35.63	37.9	5.34	4.97
2L08	4	7	L13/y	N	47.22	60.03	35.63	37.9	11.59	22.13
2L08	4	8	L13/y	Y	36.86	42.94	35.63	37.9	1.23	5.04
2L08	4	9	L13/y	N	34.88	35.44	35.63	37.9	-0.75	-2.46
2L02	1	4	L3/y	Y	47	73	37.06	38.91	9.94	34.09
2L02	1	5	L3/y	N	43	53	37.06	38.91	5.94	14.09
2L02	1	6	L3/y	N	51	65	35.23	37.77	15.77	27.23
2L02	1	7	L3/y	Y	33	40	35.23	37.77	-2.23	2.23
2L02	1	8	L3/y	N	39	41	32.47	35.66	6.53	5.34
2L02	1	9	L3/y	Y	41	53	32.47	35.66	8.53	17.34
2L37	1	6	H2/y	Y	37.36	53	36.37	39.51	0.99	13.49
2L37	1	7	H2/y	N	45.44	40.91	36.37	39.51	9.07	1.4
2L37	1	8	H2/y	N	33.59	38.83	36.37	39.51	-2.78	-0.68
2L37	1	9	H2/y	N	39.32	39.94	36.37	39.51	2.95	0.43
2L07	4	6	N11/y	Y	35.81	43.28	36.28	38.38	-0.47	4.9
2L07	4	7	N11/y	N	42.56	44.8	36.28	38.38	6.28	6.42
2L07	4	8	N11/y	N	36.75	46.75	36.28	38.38	0.47	8.37
2L07	4	9	N11/y	N	36.08	37.47	36.28	38.38	-0.2	-0.91
2L50	2	6	D11/n	Y	39.59	45.15	29.29	31.59	10.3	13.56

Table B2 Farley-2 EOC10 2-cycle rod results (continued)

Assembly	Face	Rod	Location	Calculated?	Oxide Thickness at Span 6 [µm]				Measured - Predicted [µm]	
					Measured		Predicted			
					6A	6B	6A	6B	6A	6B
2L50	2	7	D11/n	N	29.43	36.1	29.29	31.59	0.14	4.51
2L50	2	8	D11/n	N	32.65	37.9	29.29	31.59	3.36	6.31
2L50	2	9	D11/n	N	30.12	37.65	29.29	31.59	0.83	6.06
2L53	1	6	E4/n	Y	43.11	57.26	29.28	31.59	13.83	25.67
2L53	1	7	E4/n	N	32.63	32.17	29.28	31.59	3.35	0.58
2L53	1	8	E4/n	N	29.7	32.15	29.28	31.59	0.42	0.56
2L53	1	9	E4/n	N	28.79	31.05	29.28	31.59	-0.49	-0.54
2L57	3	6	L12/n	Y	29.82	32.65	29.23	31.53	0.59	1.12
2L57	3	7	L12/n	N	23.46	27.08	29.23	31.53	-5.77	-4.45
2L57	3	8	L12/n	N	28.65	32.54	29.23	31.53	-0.58	1.01
2L57	3	9	L12/n	N	27.52	28.73	29.23	31.53	-1.71	-2.8
2L03	4	6	E13/y	N	34.93	36.38	33.16	36	1.77	0.38
2L03	4	7	E13/y	N	34.49	38.32	33.16	36	1.33	2.32
2L03	4	8	E13/y	Y	35.57	39.35	33.16	36	2.41	3.35
2L03	4	9	E13/y	N	37.12	42.5	33.16	36	3.96	6.5
2L05	2	6	N5/y	Y	31.56	35.14	27	30.26	4.56	4.88
2L05	2	7	N5/y	N	26.5	29.15	27	30.26	-0.5	-1.11
2L05	2	8	N5/y	N	32.64	37.09	27	30.26	5.64	6.83
2L05	2	9	N5/y	N	29.25	36.35	27	30.26	2.25	6.09
2L04	3	6	E3/y	Y	33.07	32.63	26.88	30.16	6.19	2.47
2L04	3	7	E3/y	N	27.82	31.63	26.88	30.16	0.94	1.47
2L04	3	8	E3/y	N	34.72	33.76	26.88	30.16	7.84	3.6
2L04	3	9	E3/y	N	30.16	37.86	26.88	30.16	3.28	7.7
2L01	4	6	C11/y	Y	38.22	40.32	26.88	30.16	11.34	10.16
2L01	4	7	C11/y	N	37.01	44.85	26.88	30.16	10.13	14.69
2L01	4	8	C11/y	N	34.35	36	26.88	30.16	7.47	5.84
2L01	4	9	C11/y	N	31.84	38.55	26.88	30.16	4.96	8.39
2L33	2	6	P7/y	N	24.46	28.09	25.71	29.15	-1.25	-1.06
2L33	2	7	P7/y	Y	25.49	26.96	25.71	29.15	-0.22	-2.19
2L33	2	8	P7/y	N	29.03	28.64	25.71	29.15	3.32	-0.51
2L33	2	9	P7/y	N	25.49	31.93	25.71	29.15	-0.22	2.78
2L34	1	6	J14/y	Y	30.37	30.54	24.3	27.51	6.07	3.03
2L34	1	7	J14/y	N	27.85	31.7	24.3	27.51	3.55	4.19
2L34	1	8	J14/y	N	30.19	31.57	24.3	27.51	5.89	4.06
2L34	1	9	J14/y	N	29.01	32.61	24.3	27.51	4.71	5.1
2L36	4	6	B9/y	Y	33.42	33.34	24.3	27.51	9.12	5.83
2L36	4	7	B9/y	N	30.17	32.82	24.3	27.51	5.87	5.31
2L36	4	8	B9/y	N	36.68	38.33	24.3	27.51	12.38	10.82

Table B2 Farley-2 EOC10 2-cycle rod results (continued)

Assembly	Face	Rod	Location	Calculated?	Oxide Thickness at Span 6 [µm]				Measured - Predicted [µm]	
					Measured		Predicted			
					6A	6B	6A	6B	6A	6B
2L36	4	9	B9/y	N	37.9	37.39	24.3	27.51	13.6	9.88
2L39	3	6	G2/y	Y	39.81	39.4	24.41	27.63	15.4	11.77
2L39	3	7	G2/y	N	29.26	35.75	24.41	27.63	4.85	8.12
2L39	3	8	G2/y	N	37.06	37.48	24.41	27.63	12.65	9.85
2L39	3	9	G2/y	N	40.75	42.92	24.41	27.63	16.34	15.29
2L44	2	7	K13/n	Y	26.23	43.54	18.08	19.15	8.15	24.39
2L44	2	8	K13/n	N	28.44	48.27	18.08	19.15	10.36	29.12
2L44	2	9	K13/n	N	29.14	30.54	18.54	19.74	10.6	10.8
2L44	2	10	K13/n	Y	25.98	34.78	18.54	19.74	7.44	15.04
2L44	2	11	K13/n	N	23.19	32.39	19.19	20.53	4	11.86
2L44	2	12	K13/n	Y	31.29	34.25	19.19	20.53	12.1	13.72
2L31	3	6	N6/n	Y	22.84	25.89	17.86	18.8	4.98	7.09
2L31	3	7	N6/n	N	23.48	25.67	17.86	18.8	5.62	6.87
2L31	3	8	N6/n	N	24.56	28.46	17.86	18.8	6.7	9.66
2L31	3	9	N6/n	N	26.49	25.29	17.86	18.8	8.63	6.49
2L46	4	6	F3/n	Y	25.35	26.34	17.65	18.58	7.7	7.76
2L46	4	7	F3/n	N	21.33	27.46	17.65	18.58	3.68	8.88
2L46	4	8	F3/n	N	25.21	27.46	17.65	18.58	7.56	8.88
2L46	4	9	F3/n	N	21.32	26.17	17.65	18.58	3.67	7.59
2L49	1	6	C6/n	Y	26.63	29.38	19.03	20.36	7.6	9.02
2L49	1	7	C6/n	N	28.33	32.04	19.03	20.36	9.3	11.68
2L49	1	8	C6/n	N	26.71	31.68	19.03	20.36	7.68	11.32
2L49	1	9	C6/n	N	24.63	27.43	19.03	20.36	5.6	7.07
2L30	1	6	C10/n	Y	22.48	25.69	17.86	18.8	4.62	6.89
2L30	1	7	C10/n	N	25.94	26.64	17.86	18.8	8.08	7.84
2L30	1	8	C10/n	N	24.36	27.98	17.86	18.8	6.5	9.18
2L30	1	9	C10/n	N	28.72	27.56	17.86	18.8	10.86	8.76
2L30	3	6	C10/n	Yb	18.59	23.81	14.52	13.19	4.07	10.62
2L30	3	7	C10/n	N	23.3	23.55	14.52	13.19	8.78	10.36
2L30	3	8	C10/n	N	24.34	26	14.52	13.19	9.82	12.81
2L30	3	9	C10/n	N	25.07	27.59	14.52	13.19	10.55	14.4
2L33	3	2	P7/n	N	12.73	14.04	5.41	5.66	7.32	8.38
2L33	3	3	P7/n	Y	12.35	12.83	5.41	5.66	6.94	7.17
2L33	3	4	P7/n	N	13.07	13.42	5.41	5.66	7.66	7.76
2L33	3	5	P7/n	N	13.56	13.92	5.41	5.66	8.15	8.26

Table B3 Farley-2 EOC10 3-cycle rod results

Assembly	Face	Rod	Location	Calculated?	Oxide Thickness at Span 6 [µm]		Measured - Predicted [µm]
					Measured	Predicted	
Y08	3	7	L8	Y	77.77	64.97	12.8
Y08	3	8	L8	Y	62.69	63.95	-1.26
Y08	3	9	L8	Y	56.73	65.38	-8.65
Y08	3	10	L8	Y	61.61	63.95	-2.34
Y08	3	11	L8	Y	61.63	65.15	-3.52
Y08	3	12	L8	Y	52.29	64.57	-12.28
Y04	4	6	L13/n	Y	85	70.84	14.16
Y04	4	7	L13/n	Y	91	69.81	21.19
Y04	4	8	L13/n	Y	81	69.09	11.91
Y04	4	9	L13/n	Y	87	68.35	18.65
Y04	4	10	L13/n	Y	90	62.04	27.96
Y04	4	11	L13/n	Y	99	66.15	32.85
Y13	2	7	G6	Y	39.97	46.01	-6.04
Y13	2	8	G6	Y	34.66	46.39	-11.73
Y13	2	9	G6	Y	29.54	46.73	-17.19
Y13	2	10	G6	Y	37.88	46.62	-8.74
Y13	2	11	G6	Y	30.45	46.59	-16.14
Y13	2	12	G6	Y	44.4	46.33	-1.93
Y21	4	6	J10	Y	39.03	45.82	-6.79
Y21	4	7	J10	Y	35.88	46.06	-10.18
Y21	4	8	J10	Y	37.18	46.53	-9.35
Y21	4	9	J10	Y	37.55	46.66	-9.11
Y34	1	6	E13/n	Y	32.72	34.58	-1.86
Y34	1	7	E13/n	Y	35.03	34.85	0.18
Y34	1	8	E13/n	Y	33.6	35.35	-1.75
Y34	1	9	E13/n	Y	32.82	35.37	-2.55

Table B4 Farley-2 EOC9 1-cycle rod results

Assembly	Rod	Calculated?	Oxide Thickness at Span 6 [µm]				Measured - Predicted [µm]	
			Measured		Predicted			
			6A	6B	6A	6B	6A	6B
2L51	F17	Y	17.79	14.96	11.67	11.83	6.12	3.13
2L51	G17	Y	12.75	13.81	11.62	11.79	1.13	2.02
2L51	H17	Y	18.11	14.71	11.54	11.7	6.57	3.01
2L51	I17	Y	15.66	14.8	11.43	11.59	4.23	3.21
2L51	J17	Y	12.57	13.2	11.45	11.6	1.12	1.6
2L51	K17	Y	10.52	10.88	11.42	11.57	-0.9	-0.69
2L26	E17	Y	7.81	9.63	11.62	11.97	-3.81	-2.34
2L26	F17	Y	9.17	10.84	11.72	12.08	-2.55	-1.24
2L26	G17	Y	9.14	11.56	11.72	12.08	-2.58	-0.52
2L26	H17	Y	10.41	11.93	11.7	12.5	-1.29	-0.57
2L26	K17	Y	8.39	10.72	11.72	12.08	-3.33	-1.36
2L26	L17	Y	9.76	10.84	11.74	12.1	-1.98	-1.26
2L02	A09	Y	12.76	15.84	9.71	9.9	3.05	5.94

Table B4 Farley-2 EOC9 1-cycle rod results (continued)

Assembly	Rod	Calculated?	Oxide Thickness at Span 6 [µm]				Measured - Predicted [µm]	
			Measured		Predicted			
			6A	6B	6A	6B	6A	6B
2L02	A10	Y	14.71	11.19	9.96	10.15	4.75	1.04
2L02	A11	Y	9.86	11.81	10.33	10.52	-0.47	1.29
2L02	A12	Y	12.3	12.14	10.67	10.86	1.63	1.28
2L02	A13	Y	13.33	18.54	10.86	11.06	2.47	7.48
2L02	A14	Y	15.63	19.2	10.88	11.08	4.75	8.12
2L33	A08	Y	10.88	11.82	9.39	9.55	1.49	2.27
2L33	A09	Y	10.98	12.04	9.46	9.61	1.52	2.43
2L33	A10	Y	9.81	10.39	9.65	9.79	0.16	0.6
2L33	A11	Y	7.83	9.12	9.8	9.95	-1.97	-0.83
2L33	A12	Y	8.12	10.54	9.93	10.08	-1.81	0.46
2L33	A13	Y	9.27	9.19	9.95	10.1	-0.68	-0.91

Table B5 Farley-2 EOC9 2-cycle rod results

Assembly	Rod	Calculated?	Oxide Thickness at Span 6 [µm]		Measured - Predicted [µm]
			Measured	Predicted	
Y04	F01	Y	28.18	34.87	-6.69
Y04	G01	Y	33.96	34.48	-0.52
Y04	H01	Y	32.93	33.93	-1
Y04	I01	Y	34.48	33.22	1.26
Y04	J01	Y	34.91	32.51	2.4
Y04	K01	Y	34.06	31.66	2.4
Y09	H01	Y	24.11	35.84	-11.73
Y09	I01	Y	29.43	35.88	-6.45
Y09	Q11	Y	26.8	32.22	-5.42
Y09	Q12	Y	26.96	35.25	-8.29
Y09	Q13	Y	23.27	34.3	-11.03
Y09	Q14	Y	22.27	30.95	-8.68
Y10	Q06	Y	27.57	35.76	-8.19
Y10	Q07	Y	28.83	35.72	-6.89
Y10	Q08	Y	29.55	35.76	-6.21
Y10	Q09	Y	26.32	35.87	-9.55
Y10	Q10	Y	31.17	35.93	-4.76
Y10	Q11	Y	32.78	35.71	-2.93

Table B6 Farley-1 EOC13 1-cycle rod results

Assembly	Face	Rod	Location	Calculated?	Oxide Thickness at Span 6 [µm]				Measured - Predicted [µm]	
					Measured		Predicted			
					6A	6B	6A	6B	6A	6B
2E30	4	6	H13/n	N	14.5	14.5	12.87	12.86	1.63	1.64
2E30	4	7	H13/n	N	20.5	16.5	12.87	12.86	7.63	3.64
2E30	4	8	H13/n	Y	15.5	17.5	12.87	12.86	2.63	4.64
2E30	4	9	H13/n	N	21.5	16.5	12.87	12.86	8.63	3.64
2E30	4	10	H13/n	N	14.5	17.5	12.87	12.86	1.63	4.64
2E30	4	11	H13/n	N	23.5	16.5	12.87	12.86	10.63	3.64
2E57	3	7	E4/n	N	13.5	18.5	12.27	12.28	1.23	6.22
2E57	3	8	E4/n	N	20.5	15.5	12.27	12.28	8.23	3.22
2E57	3	9	E4/n	Y	15.5	17.5	12.27	12.28	3.23	5.22
2E57	3	10	E4/n	N	19.5	17.5	13.27	13.25	6.23	4.25
2E57	3	11	E4/n	N	12.5	17.5	13.27	13.25	-0.77	4.25
2E57	3	12	E4/n	Y	13.5	18.5	13.27	13.25	0.23	5.25
2E45	2	4	F3	N	13.5	20.5	12.54	12.54	0.96	7.96
2E45	2	5	F3	N	19.5	14.5	12.54	12.54	6.96	1.96
2E45	2	6	F3	Y	15.5	21.5	12.54	12.54	2.96	8.96
2E45	2	7	F3	N	21.5	18.5	12.54	12.54	8.96	5.96
2E45	2	8	F3	N	16.5	21.5	12	11.98	4.5	9.52
2E45	2	9	F3	Y	18.5	16.5	12	11.98	6.5	4.52
2E11	3	6	B8/y	N	28.5	28.5	13.66	13.68	14.84	14.82
2E11	3	7	B8/y	N	26.5	31.5	13.66	13.68	12.84	17.82
2E11	3	8	B8/y	N	28.5	29.5	13.66	13.68	14.84	15.82
2E11	3	9	B8/y	Y	21.5	29.5	13.66	13.68	7.84	15.82
2E11	3	10	B8/y	N	30.5	31.5	13.66	13.68	16.84	17.82
2E11	3	11	B8/y	N	25.5	27.5	13.66	13.68	11.84	13.82
2E50	3	4	D12/y	N	20.5	15.5	11.47	11.49	9.03	4.01
2E50	3	5	D12/y	N	14.5	19.5	11.47	11.49	3.03	8.01
2E50	3	6	D12/y	N	18.5	17.5	11.47	11.49	7.03	6.01
2E50	3	7	D12/y	Y	12.5	14.5	11.47	11.49	1.03	3.01
2E50	3	8	D12/y	N	13.5	14.5	11.47	11.49	2.03	3.01
2E50	3	9	D12/y	N	15.5	15.5	11.47	11.49	4.03	4.01

Table B7 Farley-1 EOC13 2-cycle rod results

Assembly	Face	Rod	Location	Calculated?	Oxide Thickness at Span 6 [µm]				Measured - Predicted [µm]	
					Measured		Predicted			
					6A	6B	6A	6B	6A	6B
2D07	3	6	F9/y	N	43.5	36.5	44.34	45.23	-0.84	-8.73
2D07	3	7	F9/y	N	31.5	38.5	44.34	45.23	-12.84	-6.73
2D07	3	8	F9/y	Y	42.5	42.5	44.34	45.23	-1.84	-2.73
2D07	3	9	F9/y	Y	29.5	37.5	44.12	45.11	-14.62	-7.61
2D07	3	10	F9/y	N	33.5	40.5	44.34	45.23	-10.84	-4.73
2D07	3	11	F9/y	N	32.5	34.5	44.34	45.23	-11.84	-10.73
2D50	3	6	F12/y	N	38.5	41.5	39.8	41.58	-1.3	-0.08
2D50	3	7	F12/y	Y	35.5	45.5	39.8	41.58	-4.3	3.92
2D50	3	8	F12/y	Y	42.5	47.5	39.94	41.73	2.56	5.77
2D50	3	9	F12/y	N	35.5	48.5	39.94	41.73	-4.44	6.77
2D50	3	10	F12/y	N	45.5	47.5	39.94	41.73	5.56	5.77
2D50	3	11	F12/y	N	34.5	41.5	39.94	41.73	-5.44	-0.23
2D02	2	5	F7/y	N	40.5	41.5	34.88	37.41	5.62	4.09
2D02	2	6	F7/y	N	52.5	42.5	34.88	37.41	17.62	5.09
2D02	2	7	F7/y	N	44.5	54.5	34.88	37.41	9.62	17.09
2D02	2	8	F7/y	Y	47.5	39.5	36.23	38.78	11.27	0.72
2D02	2	9	F7/y	N	38.5	38.5	36.23	38.78	2.27	-0.28
2D02	2	10	F7/y	Y	37.5	37.5	34.88	37.41	2.62	0.09
2D29	4	5	M8/y	N	60.5	61.5	37.1	38.81	23.4	22.69
2D29	4	6	M8/y	Y	47.5	46.5	37.1	38.81	10.4	7.69
2D29	4	7	M8/y	N	40.5	57.5	37.1	38.81	3.4	18.69
2D29	4	8	M8/y	N	47.5	54.5	34.6	36.16	12.9	18.34
2D29	4	9	M8/y	Y	48.5	58.5	34.6	36.16	13.9	22.34
2D29	4	10	M8/y	N	52.5	60.5	37.1	38.81	15.4	21.69
2D41	4	6	H5/n	N	27.5	25.5	32.09	34.02	-4.59	-8.52
2D41	4	7	H5/n	N	21.5	28.5	32.09	34.02	-10.59	-5.52
2D41	4	8	H5/n	N	29.5	31.5	32.09	34.02	-2.59	-2.52
2D41	4	9	H5/n	Y	30.5	35.5	30.37	32.31	0.13	3.19
2D41	4	10	H5/n	N	32.5	39.5	32.09	34.02	0.41	5.48
2D41	4	11	H5/n	Y	28.5	29.5	32.09	34.02	-3.59	-4.52

Table B8 Farley-1 EOC13 3-cycle rod results

Assembly	Face	Rod	Location	Calculated?	Oxide Thickness at Span 6 [µm]		Measured - Predicted [µm]
					Measured	Predicted	
2C12	3	9	E11/y	Y	88.5	77.12	11.38
2C12	3	10	E11/y	Y	83.5	77.19	6.31
2C12	3	11	E11/y	Y	64.5	77.01	-12.51
2C12	3	12	E11/y	Y	86.5	75.99	10.51
2C12	3	13	E11/y	Y	69.5	76.36	-6.86
2C12	3	14	E11/y	Y	80.5	74.73	5.77
2C60	1	6	L13/y	Y	18.5	42.16	-23.66
2C60	1	7	L13/y	Y	26.5	43.46	-16.96
2C60	1	8	L13/y	Y	26.5	45.68	-19.18
2C60	1	9	L13/y	Y	34.5	46.54	-12.04
2C60	1	10	L13/y	Y	35.5	48.27	-12.77
2C60	1	11	L13/y	Y	45.5	50.15	-4.65

Appendix C

AVERAGE SHIFT AND STANDARD DEVIATION CALCULATIONS

The average measured minus predicted oxide thickness value was calculated as:

$$\text{Average} = \bar{x} = \sum_{i=n}^{N} \frac{M_i - P_i}{N} \qquad \text{Eq. (C-1)}$$

where:

M_i = measured oxide thickness for sample i,

P_i = predicted oxide thickness for sample i, and

N = number of samples in our analysis.

The standard deviation, σ, on the measured minus predicted oxide thickness average is calculated as:

$$\sigma = \sqrt{\frac{\sum_{i=1}^{N}\left[\left(M_i - P_i\right) - \bar{x}\right]^2}{N-1}} \qquad \text{Eq. (C-2)}$$

Two dashed lies are shown in Figure 32 and 34, one representing the best linear fit of the data and the other representing the best linear fit plus one standard deviation. The standard deviation on the linear fit, σ_{fit}, is calculated as:

$$\sigma_{fit} = \sqrt{\frac{\sum_{i=1}^{N}\left[\left(M_{fit,i} - M_i\right) - \bar{x}_{fit}\right]^2}{N-1}} \qquad \text{Eq. (C-3)}$$

where:

$M_{fit,i}$ = fitted measured oxide value from curve fit $M_{fit,i} = mP_i + b$ for sample i,

$\bar{x}_{fit}$ = average value of $M_{fit,i} - M_i$, which is equal to 0.0,

m = curve fit coefficient, and

b = curve fit constant.

WARNING: This Document contains information classified under U.S. Export Control regulations as restricted from export outside the United States. You are under an obligation to ensure that you have a legal right to obtain access to this information and to ensure that you obtain an export license prior to any re-export of this information. Special restrictions apply to access by anyone that is not a United States citizen or a Permanent United States resident. For further information regarding your obligations, please see the information contained below in the section titled "Export Control Restrictions."

Export Control Restrictions

Access to and use of EPRI Intellectual Property is granted with the specific understanding and requirement that responsibility for ensuring full compliance with all applicable U.S. and foreign export laws and regulations is being undertaken by you and your company. This includes an obligation to ensure that any individual receiving access hereunder who is not a U.S. citizen or permanent U.S. resident is permitted access under applicable U.S. and foreign export laws and regulations. In the event you are uncertain whether you or your company may lawfully obtain access to this EPRI Intellectual Property, you acknowledge that it is your obligation to consult with your company's legal counsel to determine whether this access is lawful. Although EPRI may make available on a case by case basis an informal assessment of the applicable U.S. export classification for specific EPRI Intellectual Property, you and your company acknowledge that this assessment is solely for informational purposes and not for reliance purposes. You and your company acknowledge that it is still the obligation of you and your company to make your own assessment of the applicable U.S. export classification and ensure compliance accordingly. You and your company understand and acknowledge your obligations to make a prompt report to EPRI and the appropriate authorities regarding any access to or use of EPRI Intellectual Property hereunder that may be in violation of applicable U.S. or foreign export laws or regulations.

About EPRI

EPRI creates science and technology solutions for the global energy and energy services industry. U.S. electric utilities established the Electric Power Research Institute in 1973 as a nonprofit research consortium for the benefit of utility members, their customers, and society. Now known simply as EPRI, the company provides a wide range of innovative products and services to more than 1000 energy-related organizations in 40 countries. EPRI's multidisciplinary team of scientists and engineers draws on a worldwide network of technical and business expertise to help solve today's toughest energy and environmental problems.

EPRI. Electrify the World

Program:

Nuclear Power

TR-106358-V2

EPRI • 3412 Hillview Avenue, Palo Alto, California 94304 • PO Box 10412, Palo Alto, California 94303 • USA
800.313.3774 • 650.855.2121 • askepri@epri.com • www.epri.com